

**Shape Control and Residual Stresses Management in Carbon Fiber Reinforced
Thermoplastic Structures Manufactured Using Automated Fiber Placement**

Clara Scattolin

A Thesis in
The Department of
Mechanical, Industrial, and Aerospace Engineering

Presented in Partial Fulfillment of the
Requirements for the Degree of Master of Applied Science
at Concordia University
Montreal, Quebec, Canada

January 2024

© Clara Scattolin, 2023

CONCORDIA UNIVERSITY
School of Graduate Studies

This is to certify that the thesis

Prepared by: Clara Scattolin

Entitled: Shape Control and Residual Stresses Management in Carbon Fiber Reinforced Thermoplastic Structures Manufactured Using Automated Fiber Placement

and submitted in partial fulfillment of the requirements for the degree of

Master of Applied Science (Mechanical Engineering)

complies with the regulations of the University and meets the accepted standards with respect to originality and quality.

Signed by the final Examining Committee:

Dr. Farjad Shadmehri Chair

Dr. Khaled E. Galal Examiner

Dr. Farjad Shadmehri Examiner

Dr. Suong Van Hoa Supervisor

Approved by

Dr. Sivakumar Narayanswamy
MASc. Mechanical and Industrial Program Director

January 2024

Dr. Mourad Debbabi, Dean
Gina Cody School of Engineering and Computer Science

ABSTRACT

Shape Control and Residual Stresses Management in Carbon Fiber Reinforced Thermoplastic Structures Manufactured Using Automated Fiber Placement

Clara Scattolin

Thermoplastics are particularly well suited to the aerospace industry because of their superior mechanical properties and shelf-life when compared to thermosets. When manufacturing thermoplastic composite parts using automated fiber placement (AFP) technology, the high processing temperature and non-uniform cooling causes residual process stresses to arise. Constituent level or ply level stresses are residual stresses that come from interactions inherent to the composite system. They would be present in this carbon fiber reinforced polyether ether ketone (PEEK) material system regardless of the manufacturing method. Residual process stresses are laminate level stresses that arise from an external process, like AFP manufacturing.

AFP manufactured parts can include flat panels with free edges and fully constrained geometries like rings and cylinders. They express their residual stresses somewhat differently: flat panels will warp visibly as they cool, while the stresses present in rings will only be visible once they have been slit along their length. They will visibly spring in or out.

The goal of this thesis was to see if it was possible to use annealing to relieve the residual process stresses from thermoplastic composite structures manufactured using AFP without compromising laminate properties. These properties included crystallinity, void content, and fiber volume fraction. It would seem that the residual stresses in unidirectional panels with free edges can be mostly relieved with annealing. A 3-hour hold at 200°C brought them to within 2mm of flat. However, the radii and spring-in or spring-out behavior of hoop-wound and asymmetric rings remained unaffected.

Copyright 2023, School of Graduate Studies, Concordia University – December 2023

Acknowledgements

Thank you to my supervisor Dr Suong V. Hoa for proposing this project idea to me and seeing it through.

Thank you to Dr Daniel Rosca for his insight into thermoplastic composite behavior and for his invaluable help manufacturing my samples.

Thank you to my officemates on the 13th floor for their help in the lab and serving as a sounding board for my ideas.

And finally, thank you to me parents for putting up with me postponing adulthood for 2 more years.

Table of Contents

List of figures.....	viii
List of tables.....	xi
Chapter 1: Introduction.....	1
1.1 Composite materials.....	1
1.2 Automated fiber placement.....	1
1.2.1 Description.....	1
1.2.2 Applications.....	3
1.3 Thermoplastic composites.....	3
1.4 Levels of residual stresses.....	4
1.4.1 Micromechanical.....	4
1.4.2 Macro-mechanical.....	5
1.4.3 Global.....	6
1.5 Residual process induced stresses.....	7
1.6 Measuring residual stresses.....	7
1.7 Impact of residual process stresses.....	8
1.8 Research goal.....	9
1.8.1 Research objectives.....	10
Chapter 2: Literature review.....	12
2.1 Stress from strain calculations for flat and cylindrical laminates.....	12
2.2 Modeling residual stresses.....	13
2.3 Annealing experiments.....	15
2.3.1 Material and ultimate properties.....	16
2.3.2 Laminate properties.....	16
2.3.3 Thermal properties.....	17
2.3.4 Process residual strains.....	18
2.4 Possible impact of research.....	19
Chapter 3: Design of heat treatment cycle using flat panels.....	21
3.1 Selecting annealing cycle parameters.....	21
3.2 Flatness condition.....	24
3.3 Surface characterization.....	25
3.3.1 Stability test.....	26
3.3.2 MATLAB's curve fitting toolbox.....	28
3.3.3 Function validation.....	28

3.3.4	Curvature equations	30
3.4	Final cycle parameters.....	32
3.5	Results and discussion.....	32
Chapter 4:	Annealing of thermoplastic composite rings.....	36
4.1	Goal	36
4.2	Design of sample layup sequences.....	37
4.3	Sample manufacturing.....	40
4.3.1	Processing conditions.....	40
4.3.2	Material specifications	41
4.4	Ring annealing.....	42
4.5	Sample dimensioning and cutting	42
4.6	Experimental procedure	43
4.6.1	Strain gages	43
4.6.2	Strain gage installation.....	45
4.6.3	Data collection system	48
4.6.4	Radius	48
4.7	Data collection for sample characterization	49
4.7.1	Micrograph analysis.....	49
4.7.2	Crystallinity.....	54
Chapter 5:	Ring annealing results	56
5.1	Sample characterization	56
5.1.1	Fiber volume fraction.....	56
5.1.2	Void content.....	60
5.1.3	DSC crystallinity results	62
5.2	Strain measurements	66
5.2.1	Unidirectional samples.....	66
5.2.2	Asymmetric samples	68
Chapter 6:	Stress from strain calculations	72
6.1	Classical laminate theory (CLT)	72
6.2	Stress-strain relations for thin cylindrical shells	73
6.2.1	Compliance matrix transformation	74
6.2.2	Stress equilibrium in cylindrical coordinates.....	76
6.3	Approach for hoop-wound samples	78
6.3.1	Sample calculations	78

6.3.2	Result	79
6.4	Approach for asymmetric samples	82
6.4.1	Sample calculations	82
6.4.2	Results.....	83
Chapter 7:	Discussion	87
7.1	Sample characterization	87
7.2	Hoop-wound samples	89
7.3	Asymmetric samples	91
Chapter 8:	Conclusion.....	93
8.1	Contributions.....	94
8.2	Future work	94
Chapter 9:	Manufacturing recommendations.....	95
References	96

List of figures

Figure 1: Schematic of AFP machine head [10].....	2
Figure 2: Examples of an AFP with a horizontal gantry (left) and robotic arm (right) [10]	2
Figure 3: Residual stresses on the fiber and matrix of a composite. Note the tensile ($\blacktriangleleft\blacktriangleright$) stresses on the matrix and compressive ($\blacktriangleright\blacktriangleleft$) stresses on the fiber [19]	4
Figure 4: Sketch of lamina deformation as it cools. Blue outline represents the ply when warm, while yellow represents the ply once cold	5
Figure 5: Overview of macro-mechanical stresses. Image on the top right shows how the plies would contract if left unconstrained, while the bottom right image shows the net result when constrained [24].....	6
Figure 6: An example of global stresses of a sample that was rapidly cooled [19].....	6
Figure 7: An example of how global process induced stresses arise during the AFP process. Note that in all cases the fiber direction is perpendicular to the page. Each ply contracts as it cools, contracting the fibers beneath it [25].....	7
Figure 8: Speckle pattern used for DIC strain measurements [33].....	8
Figure 9: Supposedly flat panel manufactured using AFP	9
Figure 10: Unidirectional ring manufactured using AFP	9
Figure 11: Section of leading edge of aircraft nacelle manufactured using AFP	10
Figure 12: Transformation from cartesian coordinates (left) to cylindrical coordinates (right) presented by Siegl and Ehrlich [38].....	12
Figure 13: Force balance using winding tension from Cirino and Pipes [40]	14
Figure 14: Experimental jig for measuring residual strains in split ring experiment by Schlottermuller et al. [27]	18
Figure 15: Curvature measurement fixture from Unger and Hansen [49].....	19
Figure 16: Definition of flatness tolerance by ISO (left) and flatness callout for technical drawings (right) [79]	24
Figure 17: Laser measuring system experimental set-up (left) and coordinate system (right).....	26
Figure 18: Set up for sensitivity test	27
Figure 19: Adjusted height of surface for sensitivity experiment.....	28
Figure 20: Top view of sample from trial 3 before annealing, 4 layers unidirectional	29
Figure 21: Side view of sample from trial 3 before annealing, 4 layers unidirectional.....	29
Figure 22: MATLAB fit function for sample from trial 3 before annealing, axes are in mm	29
Figure 23: Vacuum bag assembly for heat blanket experiment.....	32
Figure 24: Side view of sample from trial 3 after annealing, 4 layers unidirectional.....	34
Figure 25: Alternative manufacturing method for tight curves	36
Figure 26: Coordinate system used for bimetallic strip approximation.....	38
Figure 27: Expected spring in and spring out behavior	39
Figure 28: AFP manufacturing of experimental samples	40
Figure 29: Manufactured samples cooling on mandrel after deposition.....	41
Figure 30: Readout of manufacturing parameters	41
Figure 31: $[90]_8$, $[90_4, 45_4]_T$ and $[45_4, 90_4]_T$ samples in convection oven for annealing	43
Figure 32: 2-part cutting jig oblique view, the grip (right) and cutting guide (left)	43

Figure 33: Linear strain gage installed on outer surface (left) and inner surface (right) of annealed unidirectional hoop-wound sample.....	45
Figure 34: Rectangular rosettes installed on outer surface (left) and inner surface (right) of not annealed $[90_4, 45_4]_T$ sample	45
Figure 35: Strain gage installation material including waterproof coating, M-Bond 200 adhesive and catalyst, 99% isopropyl alcohol, PCT installation tape and glass sheet.....	46
Figure 36: Rectangular rosette being lifted from glass sheet at a 45° angle	46
Figure 37: Strain gage alignment on different layups, diagram not to scale [101], [102]	47
Figure 38: Alignment of rectangular rosette on a 90° outer plie (left) and rectangular rosette pulled back to allow the glue application (right)	47
Figure 39: System 8000-8-SM for data collection.....	48
Figure 40: Inner and outer radius measured using the arc measurement tool[107].....	49
Figure 41: Mold and sample holder (left), polished puck (right)	50
Figure 42: PRESI - MECATECH 234 polishing machine	50
Figure 43: Image of thermoplastic tape (20X magnification) transformed using adapted procedure.....	52
Figure 44: Number of fibers and their respective surface area being calculated in ImageJ for thermoplastic tape at 20X magnification	52
Figure 45: Threshold necessary for void analysis.....	53
Figure 46: Annealed $[45_4, 90_4]_T$ sample cropped to retain a representative portion of the 45° layers at 20X magnification	54
Figure 47: Annealed $[45_4, 90_4]_T$ sample with the threshold adjusted to select only for the voids 20X magnification	54
Figure 48: Annealed $[45_4, 90_4]_T$ sample with voids counted using 'Analyze Particles' function 20X magnification	54
Figure 49: Micrograph for in-situ hoop-wound sample at 10 times magnification.....	57
Figure 50: Binary image to isolate the fibers for in-situ hoop-wound sample (original image Figure 49) at 10 times magnification	57
Figure 51: Micrograph for an annealed $[90_4, 45_4]_T$ sample at 10 times magnification	58
Figure 52: Binary image to isolate the fibers for an annealed $[45_4, 90_4]_T$ sample (original image Figure 51) at 10 times magnification	59
Figure 53: Compilation of tape micrographs with resin rich areas (20X magnification).....	59
Figure 54: Cropped micrograph for annealed $[45_4, 90_4]_T$ sample.....	61
Figure 55: Binary transformation of annealed $[45_4, 90_4]_T$ sample to select the voids in the laminate.....	61
Figure 56: Cropped micrograph for in-situ $[90_4, 45_4]_T$ sample.....	62
Figure 57: Binary transformation of annealed $[90_4, 45_4]_T$ sample to select the voids in the laminate.....	62
Figure 58: DSC results for a sample of carbon fiber reinforced thermoplastic tape	64
Figure 59: DSC results for a sample for annealed $[90]_8$ sample	64
Figure 60: DSC results for a sample for not annealed $[90_4, 45_4]_T$ sample.....	65
Figure 61: DSC results for a sample for annealed $[45_4, 90_4]_T$ sample	65
Figure 62: In-situ hoop-wound sample exhibiting spring in behavior.....	66

Figure 63: Strain as a function of time (10 datapoints per second) for annealed hoop-wound sample 2, cut 2	67
Figure 64: In-situ consolidated $[90_4, 45_4]_T$ sample with one cut experiencing spring out behavior	68
Figure 65: In-situ consolidated $[45_4, 90_4]_T$ sample with one cut experiencing spring in behavior	69
Figure 66: Strain as a function of time (10 datapoints per second) during cutting procedure for in-situ $[90_4, 45_4]_T$ sample.....	69
Figure 67: Coordinate system for CLT	72
Figure 68: Cylindrical coordinates, showing the circumferential and radial directions	73
Figure 69: Circumferential strain distribution for the in-situ and annealed hoop-wound samples calculated in cylindrical coordinates.....	80
Figure 70: Circumferential stress distribution for the in-situ and annealed hoop-wound samples calculated in cylindrical coordinates.....	81
Figure 71: Radial stress distribution for the in-situ and annealed hoop-wound samples calculated in cylindrical coordinates.....	81
Figure 72: Circumferential strain distribution for in-situ and annealed $[90_4, 45_4]_T$ samples.....	83
Figure 73: Circumferential strain distribution for in-situ and annealed $[45_4, 90_4]_T$ samples ..	84
Figure 74: Circumferential strain distribution when radial stress at the inner surface is set to zero	90

List of tables

Table 1: Experiments consulted when designing annealing cycle.....	22
Table 2: Annealing processing parameters for flat samples	23
Table 3: Straightness and flatness recommended tolerances in mm [80].....	25
Table 4: Standard deviation data with adjusted z	27
Table 5: Adjusted R ² for different degrees of x and y. This fit contains 41 points.....	30
Table 6: RMSE for different degrees of x and y. This fit contains 41 points.....	30
Table 7: Gaussian curvature before and after heat treatment	32
Table 8: Mean curvature before and after heat treatment	33
Table 9: Maximum variation in the z direction after heat treatment and the mean radius of curvature before and after heat treatment	34
Table 10: Sample specifications	37
Table 11: Average ply properties for the arrangement shown in Figure 26	38
Table 12: Curvature and deflection results for the arrangement shown in Figure 26.....	39
Table 13: Thermal properties of APC-2 PEEK matrix according to manufacturer [77].....	41
Table 14: APC-2/AS4 tape properties from manufacturer at 24°C [77], [95]	42
Table 15: Final annealing cycle parameters for thermoplastic composite rings.....	42
Table 16: Manufacturer data for strain gages	44
Table 17: Breakdown of tools used for strain gage application.....	46
Table 18:Polishing procedure	51
Table 19: Testing procedure for DSC.....	55
Table 20: Fiber volume fraction for carbon fiber reinforced tape, in-situ consolidated samples and annealed samples.....	56
Table 21: Void content for carbon fiber reinforced tape, in-situ consolidated samples and annealed samples	60
Table 22: Crystallinity for tape, un-annealed samples and annealed samples.....	63
Table 23: Measured Residual strain for in-situ and annealed hoop-wound samples.....	66
Table 24: Outer radii of in-situ and annealed samples before and after cutting.....	68
Table 25: Measured Residual strain for in-situ and annealed $[90_4, 45_4]_T$ samples	70
Table 26: Measured Residual strain for in-situ and annealed $[45_4, 90_4]_T$ samples	70
Table 27: Outer radii of $[90_4, 45_4]_T$ in-situ and annealed samples before and after cutting	71
Table 28: Outer radii of $[45_4, 90_4]_T$ in-situ and annealed samples before and after cutting	71
Table 29: Mechanical properties used to calculate residual stresses	72
Table 30: Circumferential and radial stresses for the outer and inner surfaces of the hoop-wound samples calculated using stress from strain calculations from Chapter 6.....	79
Table 31: Strain distribution for annealed $[45_4, 90_4]_T$ sample 1	82
Table 32: [ABD] matrix for $[45_4, 90_4]_T$ laminates	82
Table 33: Midplane strain and curvature used to calculate the force and moment resultants for the $[90_4, 45_4]_T$ samples.....	85
Table 34: Midplane strain and curvature used to calculate the force and moment resultants for the $[45_4, 90_4]_T$ samples	86

Chapter 1: Introduction

1.1 Composite materials

Composite materials are an active area of research with a variety of specialized applications. Composite materials are advanced materials composed of at least two distinct constituent phases. The constituent phases are mixed, but remain chemically distinct from one another [1]. These phases are generally referred to as the reinforcement and the matrix phase. The reinforcement phase is the stiffer and stronger phase which provides the strength to the material. The matrix phase holds the fibers together and transfers the load from one fiber to the next [1], [2].

Matrix materials are generally classified into 3 categories: metal, polymer and ceramic matrices [1]. The reinforcement is generally categorized into particulate or fiber reinforcements, depending on their shape [3]. In this case, fiber reinforced polymer matrix composites are what are being studied. These composites are actively being researched and have varied applications, including the aerospace and sports industries [4]. Fiber reinforced polymer matrix composites can be manufactured using several different methods, including labour intensive techniques like hand layup and fully automated methods like filament winding, automated fiber placement, pultrusion and liquid composite molding [5], [6]. The choice of technique depends on the materials used and the geometry of the finished part.

In the scope of this project, polyether ether ketone (PEEK), will be used as the matrix material and carbon fibers for the reinforcement. Automated fiber placement will be the manufacturing method of interest.

1.2 Automated fiber placement

1.2.1 Description

Automated fiber placement (AFP) is a relatively new and fully automatable manufacturing process for thermoset and thermoplastic composite materials with applications in the aerospace industry [5], [7]. AFP was developed in the 1970s as an improvement to the filament winding process. Filament winding is a process limited to cylindrical geometries, whereas AFP offers greater flexibility in the types of parts it can manufacture [8].

AFP technology is subject of current research because of its high degree of automation and flexibility makes it an interesting candidate for numerous industrial applications [4], [7], [8]. Most notably, it could serve to replace hand layup [9], which is standard in much of the aerospace industry [5].

AFP machines consist of 3 main components: the head, the robotic arm, and the substrate or tooling [10]. A breakdown of these components can be seen in Figure 1. The AFP head is responsible for heating the incoming tape and applying enough pressure to it such that it bonds to the previous layer. The heat can be applied by using a laser, gas torch, infrared or heat lamp [9], [11]. Once the end of the layer is reached, the head can cut the tape to then begin the next layer [10]. The head can be installed on a gantry or robotic arm. Robotic arms allow for more versatility in part geometry and tooling, while a gantry system allows for the manufacturing of larger components [10]. Examples of these 2 different kinds of AFP can be seen in Figure 2. The tool or mandrel on which the composite tape is applied can vary depending on the desired part

geometry. Cylindrical or elliptical mandrels can be used to create tubular geometries [11]. In these instances, the mandrel rotates as the head moves along the length of the part. Flat or curved tools can also be used to create flat or curved composite sheets [11]. In these cases, the tool is fixed and the head is responsible for all the necessary movement [10].

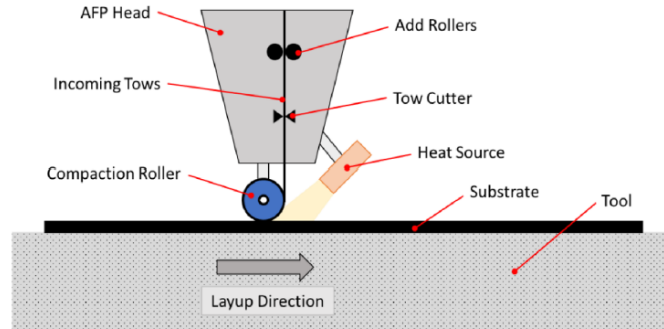


Figure 1: Schematic of AFP machine head [10]

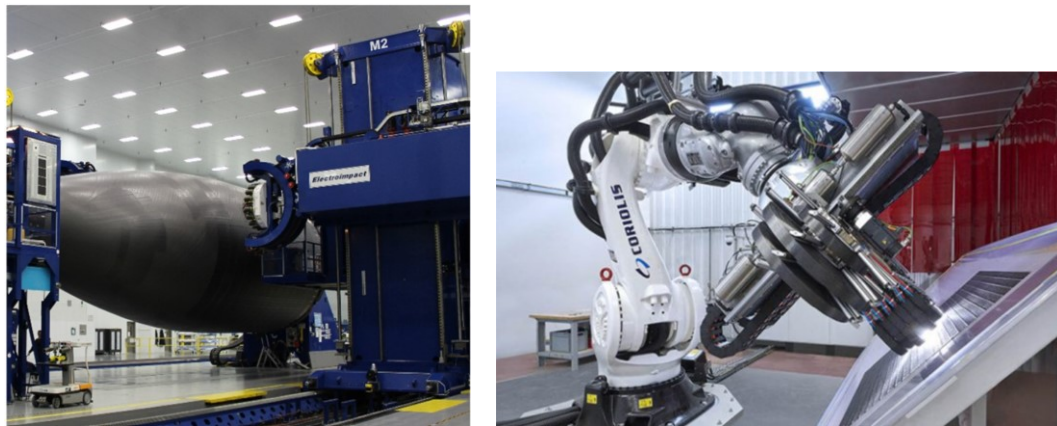


Figure 2: Examples of an AFP with a horizontal gantry (left) and robotic arm (right) [10]

The high degree of automation afforded by the AFP process has several advantages, including reducing the cost of labour, increasing the repeatability of the process, and reducing waste [4], [8]. Using long continuous tapes means that cylinders or pressure vessels can be wound continuously, without joints or seams [12]. It is also possible to achieve parts with high volume fractions [12]. Competing manufacturing processes include hand layup, which is a much slower process that requires highly trained staff [7]. This human element can also introduce variation in the resulting parts and reduces the possible output quality [10].

The AFP process has disadvantages relating to the mandrel, cost, and automation. Mandrels can be expensive to manufacture and difficult to extract once manufacturing is complete. Even if an AFP process can save on labour, the initial investment can be quite costly [12]. Automation comes with one major disadvantage: every manufacturing parameter needs to be carefully adjusted to ensure the quality of the composite. Feed rate, processing temperature and application force are factors known to significantly impact the quality of the final part [4]. If improperly managed, these parameters can cause voids to form in the composite and delamination failure to occur [4].

Another important disadvantage of AFP is that the nonuniform heating and cooling of the part causes residual stresses to develop [13]. The part is built up in an additive manner, with each new layer bonded to the previous one using heat and pressure. As the machine head travels along the part's surface, it heats the material in a very localized manner. As the head moves away, the part begins to cool. Given that the part is not at a uniform temperature, the cooling rate varies. This thermal gradient causes the residual stresses to develop. These residual thermal stresses are not apparent in cylinders due to the constraints of their geometry. However, if a ring is split open along its length, the shape will tend to spring inwards or spring open depending on the internal stresses present [13]. This deformation is visible on other shapes with free edges, like flat sheets.

1.2.2 Applications

Given that a variety of geometries can be achieved on the different possible tools, this process has several applications. AFP technology can be used to make a variety of aircraft components [4], [7], [8]. Cylindrical parts like the skin of aircraft can be made using AFP [8]. More complex geometries like airfoil shapes of flight control surfaces (ailerons and spoilers) can also be manufactured using AFP [8]. Other specialty applications include parts for high-end vehicles [4], wind turbine blades [7] and sports equipment [4].

1.3 Thermoplastic composites

Thermoplastics are a subset of plastics with interesting mechanical and thermal properties that are well suited to the AFP process. AFP machines can be used with several different types of materials, including thermoset and thermoplastic prepreg tapes [5], [7]. The winding process and machinery is the same for both types of tape, but the processing temperatures will vary.

Thermoset prepreg tapes are commonly used because of their low viscosity and low processing temperature [10]. For thermoset tapes, the layup can be done at between 60-70°C [14]. The low processing temperature allows for more variety in the materials that can be used to design the compaction rollers [14], while the low viscosity of uncured thermosets allows for better fiber wetting. These factors greatly simplify the manufacturing process and lead to good quality parts. However, after the fiber winding process, thermoset composites have the disadvantage of needing to be cured in an autoclave to allow for the cross-links which fully solidifies the plastic to form. The application of heat and pressure in an autoclave is an expensive and time consuming process [5], [9]. Thermosets also have a relatively short shelf life and need to be kept frozen until manufacturing to avoid premature curing [10].

Once cured, the thermoset composites are strong but quite brittle [15]. They also tend to have low void content, which is desirable [14]. Once they reach the end of their life, thermoset plastics cannot be recycled. The application of heat after curing causes the plastic to degrade instead of melting due to the formation of the crosslinks during the curing process [5].

Thermoplastic tapes are gaining in popularity due to their mechanical properties [16] and infinite shelf life [17], despite their manufacturing challenges which include high processing temperatures and high viscosity [5], [14]. Thermoplastics have a higher impact resistance than thermosets, which are known to be quite brittle [15]. They also have superior strength to weight ratios and fracture toughness [17].

Thermoplastics have an infinite shelf life [17], and do not require refrigeration when stored. Unlike thermosets, thermoplastic composites structures may not need post-processing, which reduces manufacturing time and costs. After the deposition process is complete and the

parts are cooled, they are ready for use. The trade-off is that thermoplastics require higher manufacturing temperatures [10]. They need to be processed at the melt temperature of the thermoplastic, which can be around 400°C [14]. These higher manufacturing temperatures are more difficult to achieve and can lead to a development of internal stresses within the part. Thermoplastics can also be reheated to their melting temperature and cooled without negative consequences. This procedure simplifies the assembly and repair processes for thermoplastic composites [15]. Assembly can be done by simply reheating the part and “welding” components together [17], [18].

Overall, thermoplastic composites offer several advantages when compared to traditional thermosets. Thermoplastics have superior mechanical properties [15], [17] and autoclave treatment may not be necessary, simplifying manufacturing and reducing production costs. The major downside of producing thermoplastic composites is the high processing temperature. These large thermal gradients can cause residual stresses within samples, warping them. Preventing and eliminating these residual stresses is an area of active research. A categorization of the residual stresses present in samples and how they arise is detailed in the next section.

1.4 Levels of residual stresses

Residual stresses develop in thermoplastic composites due to a variety of factors, including interactions within the material and from outside sources. Residual stresses in composite materials can occur at 3 different scales: the micromechanical level, the macro-mechanical level and the global level [19]. These stresses describe constituent level, laminae level, and laminate level stresses respectively. Constituent and ply level stresses are intrinsic to composite materials and due to interactions within the material itself. They would arise regardless of the manufacturing technique chosen. Stresses at the laminate level are generally caused by external factors and are a combination of manufacturing induced stresses and environmental stresses.

1.4.1 Micromechanical

The properties of a composite’s constituent phases and how these phases interact are what govern the residual stresses at a micromechanical level [19]. For this experiment, continuous carbon fibers constitute the embedded phase, and PEEK constitutes the matrix phase. PEEK is a semi-crystalline thermoplastic; its coefficient of thermal expansion is a positive value [20]. This means that the thermoplastic expands as its heated and shrinks as it cools from its melting temperature.

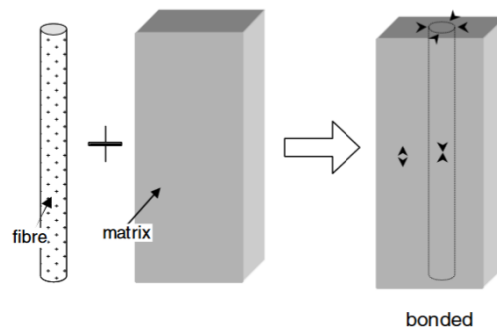


Figure 3: Residual stresses on the fiber and matrix of a composite. Note the tensile ($\leftarrow \rightarrow$) stresses on the matrix and compressive ($\rightarrow \leftarrow$) stresses on the fiber [19]

However, carbon fibers exhibit the opposite behavior. The coefficient of thermal expansion along the fibers is negative [19]. This means that as the carbon fibers cool down from the processing temperature, they tend to lengthen [19]. The mismatch between the fiber's tendency to lengthen and the thermoplastic's tendency to contract as they cool creates a tensile stress in the matrix and a compressive force on the fiber which promotes fiber buckling [19]. These stresses are illustrated in Figure 3. This kind of stress arises from a mismatch in the behaviors of the fibers and the matrix. It will always be present, regardless of the manufacturing method and layup.

1.4.2 Macro-mechanical

Macro-mechanical stresses occur as 2 laminae interact with each other [19] or as the laminae interacts with a mold or tool [21]. They arise due to the orthotropic nature of composite layers. The load bearing and thermal expansion properties of individual plies are dependant on the orientation of the material. More specifically, these orthotropic materials have 3 perpendicular axes of symmetry [22], [23].

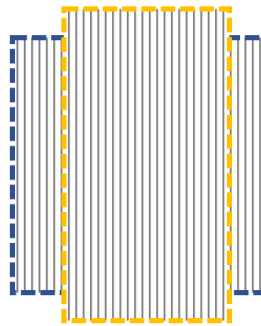


Figure 4: Sketch of lamina deformation as it cools. Blue outline represents the ply when warm, while yellow represents the ply once cold

The strength of a lamina in its fiber direction and transverse direction differs because fibers can only support loads in their longitudinal direction. If the composite is stressed in the transverse direction, the matrix, which is the much weaker phase, supports the load [2].

When cooled from its stress-free temperature, a composite lamina will lengthen in its longitudinal direction and shrink in its transverse direction. The lengthening arises from the fibers tendency to lengthen as they cool, while the shrinkage is due to the matrix's tendency to contract as it cools [19]. A sketch of this behavior can be seen in Figure 4. The blue and yellow outlines represent single lamina before and after cooling respectively. The proportions are exaggerated for illustrative purpose.

If two consecutive plies are placed at different orientations, stresses will develop between them due to these direction specific thermal properties. Take, for example, two perpendicular layers. When cooled from their stress-free temperatures, both layers will want to shrink in their transverse directions [19]. However, this movement will be constrained by the nearby perpendicular layer since it tends to expand in that direction. This mismatch will cause bending moments in the laminate [19] and residual stresses to arise. An example of this can be seen in Figure 5. The shrinkage of the 90° plies in the middle of the laminate are constrained by the 0° plies on the outer and inner surfaces. This causes residual tensile in the core of the sample and compressive stresses in the outer layers [24]. These stresses would arise regardless of the

manufacturing technique selected; they are not specific to the AFP process. They are specific to the layup sequence.

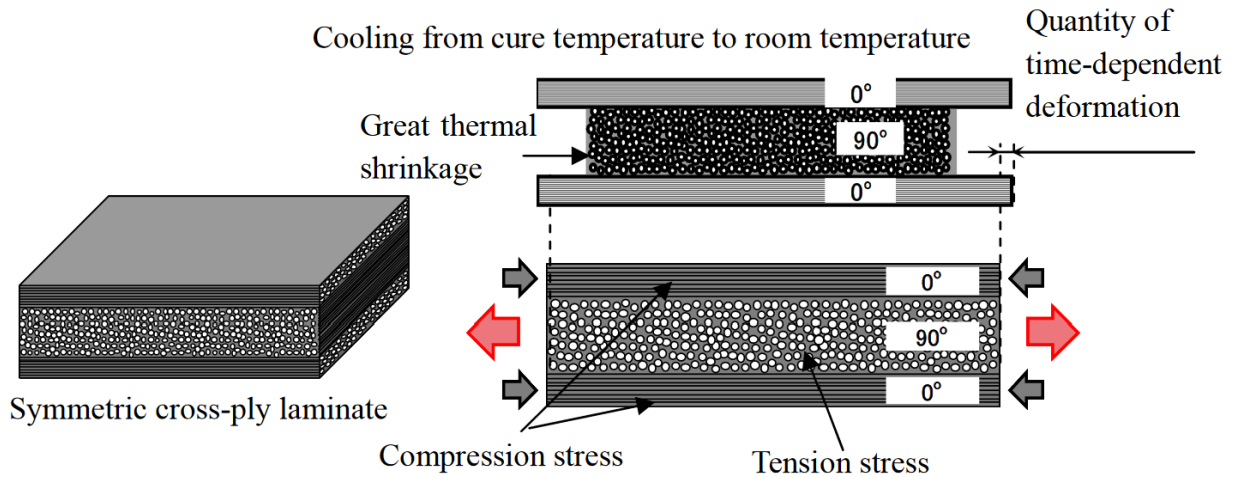


Figure 5: Overview of macro-mechanical stresses. Image on the top right shows how the plies would contract if left unconstrained, while the bottom right image shows the net result when constrained [24]

1.4.3 Global

Global laminate stresses describe external hygrothermal conditions that create a gradient in the internal stresses of a composite [19]. For example, infiltration of moisture into a composite is a slow process. When a composite is subjected to a humid environment, the outer layers will saturate much faster than the core and it could take on the order of magnitude of weeks for thin laminate to saturate fully [23]. This uneven saturation causes a stress gradient within the laminate.

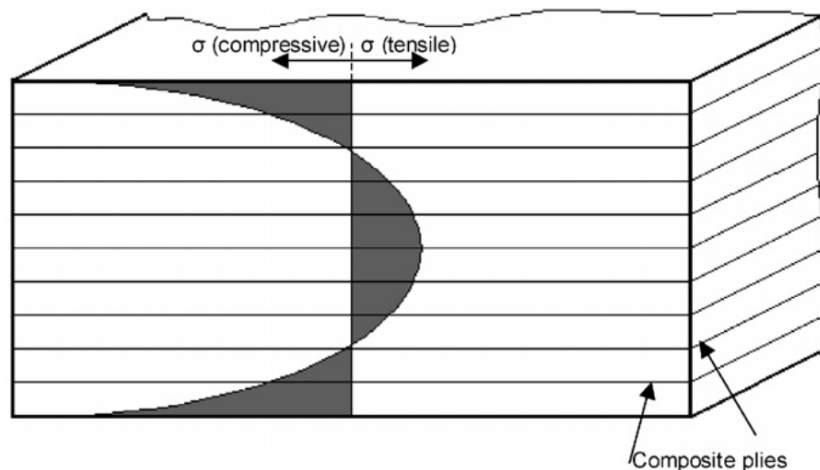


Figure 6: An example of global stresses of a sample that was rapidly cooled [19]

Uneven heating or cooling of a laminate can create a similar non-uniform stress distribution in a much shorter time. If a thick laminate is heated to a uniform temperature and then cooled, the surfaces of the laminate will cool rapidly [19] due to the convection and radiation away from the surface. The plies near the midplane will take longer to cool since

conduction through the laminate is necessary to cool them. Since the outer surfaces of the laminate are solidified and rigid, the shrinkage or expansion of the plies near the midplane cannot occur. This constraint generates tensile stresses near the center of the laminate [19]. This residual stress profile can be seen in Figure 6. Global stresses are caused by an external factor, like uneven cooling, rapid cooling, or humidity,

1.5 Residual process induced stresses

The uneven heating and cooling during the AFP manufacturing process can cause residual stresses to form. They are often referred to as ‘residual process stresses’ or ‘residual manufacturing stresses’ and they act at the laminate (global) level. An example of this can be seen in Figure 7. In this instance, all the layers are oriented so that the fiber direction is perpendicular to the page. This means that as a layer is deposited on the tool, ply would contract as it cools [25]. When another layer is added, the layer contracts, compressing the layers below it. This causes a stress gradient of compressive stresses throughout the composite part. When demoulded, the part would tend to curve inwards [25].

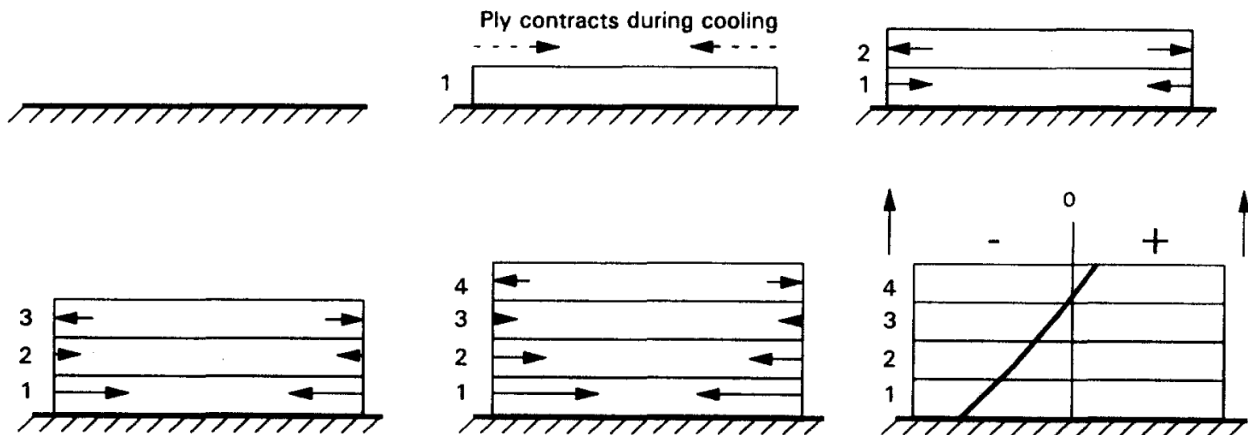


Figure 7: An example of how global process induced stresses arise during the AFP process. Note that in all cases the fiber direction is perpendicular to the page. Each ply contracts as it cools, contracting the fibers beneath it [25]

These process-induced stresses are somewhat unique to AFP manufacturing due to its layer-by-layer tape deposition. The movement of the robotic head causes rapid heating and uneven cooling, also creating residual process stresses. When using an alternate technique like hand-layup or compression moulding, the plies would have been laid down and then consolidated. An individual ply would not have a chance to cool before the next was laid down. Instead, they would have been consolidated at a uniform temperature which limits warping. These residual process stresses due to the AFP manufacturing process will be the focus of this experiment.

1.6 Measuring residual stresses

Residual stresses in carbon fiber reinforced composites can be measured in a variety of ways, including some destructive techniques like hole drilling, layer removal, slitting, and non-destructive techniques like X-ray diffraction, Bragg grating sensors, and digital image correlation (DIC). The choice of technology is usually dictated by the sample geometry, as well as the maturity and availability of the technology.

Residual stresses are often measured using destructive techniques like hole drilling or layer removal [26]. When hole drilling is used, strain gauges arranged like a rosette are placed on the surface of the composite. A hole is drilled through the middle of the strain gage arrangement and the value read by the strain gauges is the residual stresses relaxing [26]. When layer removal is performed, composite plies are machined away, and the resulting curvature is measured. The curvature in the sample after the layer removal process represents the residual stresses present at that depth [26]. When considering rings and other cylindrical geometries, samples can be sawed along their length. The displacement in or out of the rings can be measured using strain gages [13], [27]. While these techniques can reliably measure the residual strains, the samples are lost in the process.

Non-destructive techniques like X-ray diffraction, Bragg grating sensors, and digital image correlation (DIC) can also be used to measure residual strains. X-ray diffraction characterizes strain in the crystalline structure of the material [28]. The major downside of X-ray diffraction is that it can only characterize surface strains [28] and is expensive to perform [29]. Another non-destructive technique is imbedding fiber Bragg grating (FBG) sensors into composite samples. FBG sensors which are made from optical fibers and can provide strain readings by measuring the shift in the wavelength of the light reflected through the fiber [30], [31]. These sensors can be used to detect manufacturing defects [30], measure residual manufacturing strains, and allow for structural health monitoring [32]. The difficulty is that they must be embedded into the samples during manufacturing, and that the wavelength readings can be impacted by the temperature of the samples [32]. Digital image correlation (DIC) is a non-contact method of measuring the strain of large samples using a camera. Samples are painted with a speckle pattern and imaging software tracks the position of the dots to create a map of the strain field [33]. This technique is usually used for mapping the strain during destructive testing, but future applications could include the use for residual strain monitoring during sample manufacturing [33]. An example of a sample marked for DIC analysis can be seen in Figure 8.

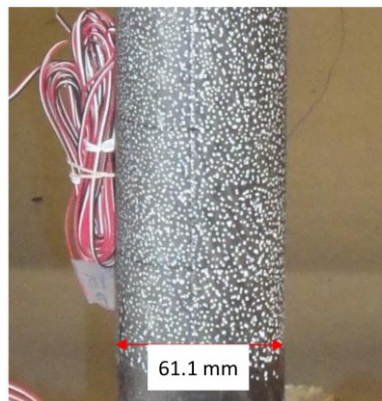


Figure 8: Speckle pattern used for DIC strain measurements [33]

1.7 Impact of residual process stresses

Residual process stresses are not usually desirable because they can cause visible distortions [34] and they can negatively impact a sample's mechanical properties [19]. The deformation can be significant, meaning that the part may no longer fit into the intended assembly. Compromising the sample's properties could lead to premature failure [19]. These are both serious problems, limiting the usefulness of AFP manufactured thermoplastic composites.

1.8 Research goal



Figure 9: Supposedly flat panel manufactured using AFP

Thermoplastics are attractive materials for the aerospace industry because of their mechanical properties, infinite shelf life, and recyclability. AFP manufacturing is also well suited to the needs of the aerospace industry because of the high degree of automation and the variety of part geometries that can be achieved. However, when these technologies are combined, the layer-by-layer deposition of the thermoplastic tape by the AFP head causes residual process stresses to arise. These stresses can impact the mechanical properties and final geometry of the part, often rendering them useless. Two different geometries will be studied here: flat panels and thin rings. These geometries were chosen because they represent unconstrained samples with free edges and fully constrained samples without any free edges respectively. An example of a supposedly flat unidirectional panel manufactured using AFP can be seen in Figure 9. Despite being manufactured on a flat mandrel, the corners of the sample lifted significantly as it cooled.

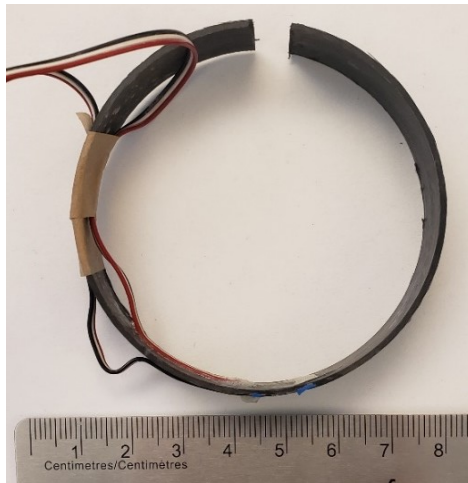


Figure 10: Unidirectional ring manufactured using AFP

Residual stresses can also arise in self constrained geometries, although they are not immediately apparent. The ring or cylinder would slide off the mandrel and appear perfectly round, providing no outward indication to the manufacturer it was subject to any residual stresses. However, when cut along its length, the part would spring open or spring closed, depending on the residual stress profile. Figure 10 shows a unidirectional hoop-wound ring that sprung inwards when a half-inch section was removed. Cylindrical geometries are of particular interest in the aerospace industry since they can be used for the fuselage of an aircraft [10]. Layup [10] and processing parameters [35] can tailor a macro-mechanical stress profile within the cylinder to counteract the cabin pressure [27]. However, the unpredictable nature of residual

process stresses could interfere with the desired stress profile. As such, they need to be eliminated even if they are not visible.

Another common issue when manufacturing curved panels or angled laminates using AFP is that they warp during manufacturing and spring open when demolded [36]. An example of such a part can be seen in Figure 11. This part is the leading edge of an aircraft nacelle. Traditionally, a custom metal mandrel would be manufactured, and tape deposited onto the mandrel from edge to edge until the desired thickness was achieved. However, the thermoplastic composites deform as the tape is being deposited and cools, making this kind of shape very difficult to achieve.

As an alternative, it would be possible to constrain the part during manufacturing by using an elliptical mandrel. The tape would be wound around the mandrel, creating a shape without free edges. This additional constrain would prevent any deformation during manufacturing. The sample could then be annealed to relieve the residual process stresses. Finally, the desired portion of the structure could be cut away, leaving behind the structure in Figure 11. It is generally understood that AFP manufactured cylinders also spring inwards or outwards when cut along their lengths. The goal of this research to see if this springing behavior can be mitigated with annealing to make this a viable manufacturing alternative.

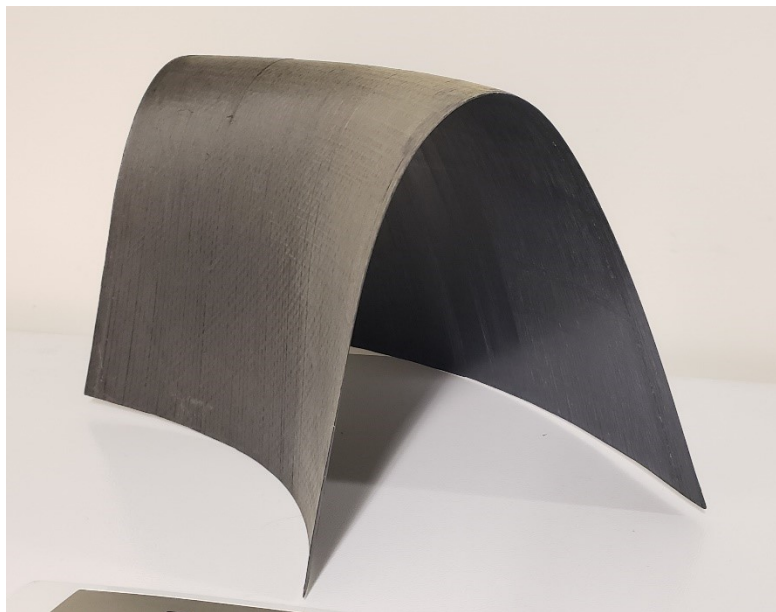


Figure 11: Section of leading edge of aircraft nacelle manufactured using AFP

1.8.1 Research objectives

The goal of this research is to eliminate the residual process stresses and reduce unwanted deflection present in AFP manufactured thermoplastic parts using annealing. Two different part geometries will be tackled in this study: flat panels (with free edges) and thin rings (fully constrained geometry). Panels that had been manufactured as flat but warped during manufacturing were used to develop and perfect a heat treatment process because the residual process stresses are easily visible and relatively easy to measure and quantify. Once the annealing procedure was finalized, it was then applied to the rings to see if the spring-in and spring-out behavior could be mitigated. Finally, key laminate properties like fiber volume

fraction, void content, and crystallinity were characterized to ensure that the heat treatment did not have adversely affect them. If successful, this could potentially allow for more widespread use of thermoplastics in the aerospace industry.

Chapter 2: Literature review

Current work relating to residual stresses in thermoplastic composites tends to focus on one of two aspects: either modeling the residual stresses to predict the final stress state or experimentally quantifying the residual process stresses. While predicting [29], [34], [35], [37], [37], [38], [39], [40], [41], [42], [43], [44], [45], [46], [47] and experimentally quantifying [13], [27], [48], [49], [50], [51], [52], [53], [54], [55], [56], [57], [58], [59], [60], [61], [62], [63] the residual stresses is important, few research groups are focused on eliminating the deformation caused by the residual stresses.

The next sections contain an overview of the current research regarding residual stresses in AFP manufactured parts. First is an overview of stress from strain calculations for different sample geometries. Next is residual stress models, including numerical and then finite element models. It concludes with an overview of annealing experiments where researchers attempt to quantify the impact of the heat treatment on residual stresses and other laminate properties. While there is significant research on modeling of residual stresses and on annealing of thermoplastics, very little of the work is focused on controlling the residual stresses of thermoplastics using post-processing.

2.1 Stress from strain calculations for flat and cylindrical laminates

Classical laminate theory (CLT) presented by Hyer [22] is a traditional method of calculating lamina properties, as well as calculating the stresses from strains in flat laminates. The stress and strain calculations are limited to flat geometries [22]. However, it is possible to extend the properties of laminae to different part geometries by means of certain matrix transformations. For example, Siegl and Ehrlich [38] present a solution for transforming compliance matrices from the x-y-z cartesian coordinates to a cylindrical coordinate system in r- θ -z. This transformation can be seen in Figure 12. They consider the composite layers to be orthotropic [38]. This allows for the transformation of the traditional properties provided by manufacturers to be converted from rectangular to cylindrical coordinates.

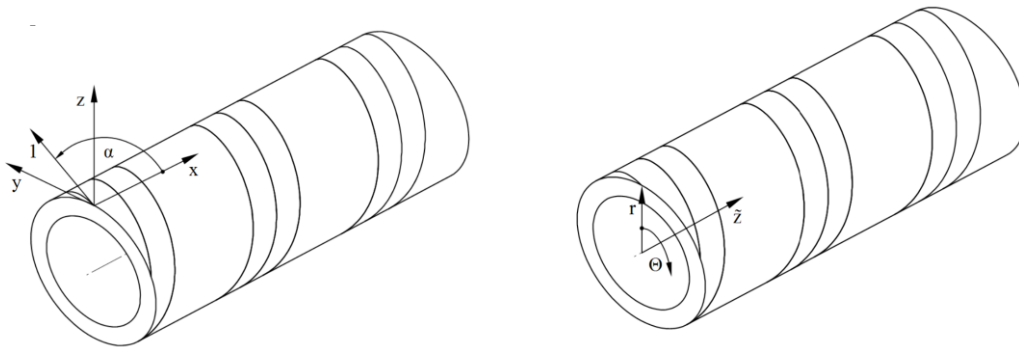


Figure 12: Transformation from cartesian coordinates (left) to cylindrical coordinates (right) presented by Siegl and Ehrlich [38]

With the compliance matrix transformed into cylindrical coordinates, it is now possible to calculate the radial, circumferential, and axial stresses from their respective strains. For cylindrical geometries, it is common to assume either plane stress [37], [40], [41], [42], [64], plane strain [43], [44], [64], or internal loading [45] conditions. When dealing with thin rings, plain stress boundary conditions are the most appropriate [37], [40], [41], [42], [64]. Cohen and Hyer [64] modeled both plain stress and plain strain conditions using the compatibility equations.

They compare the values of hoop, axial, and radial stresses of both assumptions to determine the ratio of radius to thickness of the samples best suited to this system of equations. The general approach is to approximate each composite layer as a thin shell with the upper and lower surfaces bound by the next layer [37], [40], [41], [42], [43], [44], [45], [64], [64]. The equilibrium conditions in cylindrical coordinates produce an ordinary differential equation (ODE) with a known solution [37], [39], [40], [41], [42].

When simplifying the loading conditions of a part, assuming that the structure is in pure bending can provide an alternate closed form solution to calculate the stress in cylinders [65]. Timoshenko and Goodier present an elastic solution that uses the gap in a cut ring to calculate the moment present by assuming that the ring is subject to pure bending [65]. However, it considers isotropic materials and needs to be adapted for use with composite materials.

2.2 Modeling residual stresses

AFP manufacturing is a complex multi-step process involving tape heating, tape compaction, cooling, and the thermal dependence of mechanical properties. At each step of the manufacturing process, the manufacturing parameters must be closely controlled. The temperature and time dependant properties of manufacturing are complex to model. Models for residual stresses vary significantly in complexity, part geometry, and boundary conditions. Some research groups are trying to predict residual process stresses in flat panels [29], [35], [66], cylinders [42], [43], [44], and rings [37], [40]. Other research groups are attempting to predict more niche properties, like sample bending [67], part distortion [34], [46], and laminate properties [47].

Given the impact residual stresses can have the mechanical properties of parts, predicting the residual stresses that will arise during production can be crucial to evaluating the quality of the finished part [29]. Several research groups are studying these implications on flat geometries. Chinesta et al. [29] proposes a parametric model to predict the residual stresses created during the AFP manufacturing process. Their model involves 3 distinct components: a thermal model, a mechanical model and the residual stresses. This work is still preliminary and has yet to be validated against experiments or other models [29]. Sonmez et al. [35] used stress-strain relations and temperature dependant viscoelastic behavior to predict residual stresses for rigid flat cross-ply or unidirectional composite samples. They compared the results from their model against the results from a press molding experiment. The model reliably predicted the experimental results [35]. Chapman et al. [66] designed a model to calculate the residual stresses in thermoplastic composites. Their thermal model considered the impact of temperature, crystallinity and viscosity as a function of time. The mechanical properties are calculated from the composite's constituent phases and are impacted by the sample's thermal history. Finally, the thermal and mechanical models are combined to calculate the residual stresses in the layup. This model was validated experimentally on carbon fiber reinforced PEEK samples. Layer removal was used to experimentally determine the residual stresses. They validated their model against a unidirectional ply that was 40 layers thick. Stresses in the transverse direction were reliably predicted, however, they had difficulty measuring the longitudinal stresses [66].

Given the applications for cylindrical geometries in pressure vessels and aircraft structure, process residual stresses in cylinders are also commonly modeled. Chouchaoui and Ochoa [44] developed a series of equations to relating the applied loads the deformation experienced by a composite tube. These equations were developed from partial differential equations describing

the displacement in radial coordinates and elastic constants to relate stress and strain. They used several different loading conditions including tensile, bending, torsion loads as well as internal and external pressure. They also assumed no slippage. These results were validated against an experiment published by another research group where they measured failure from internal pressure. Experimental results closely matched their prediction [44]. Tzeng [42] proposes a solutions for solving all the layers within the cylinder simultaneously by assuming that the radial stresses are constant at the interfaces for a cylinder subject to compressive loads. The numerical predictions were compared to a split ring experiment and the results matched quite closely [42]. Sayman [27] presents a numerical solution for axially symmetric composite cylinders under plane-strain condition. The model develops a system of ordinary differential equations using the stress-strain properties of the composite. Solutions for the system of equations are computed for 2 different sets of boundary conditions: an open and closed cylinder. This solution was validated against a model in ANSYS [27].

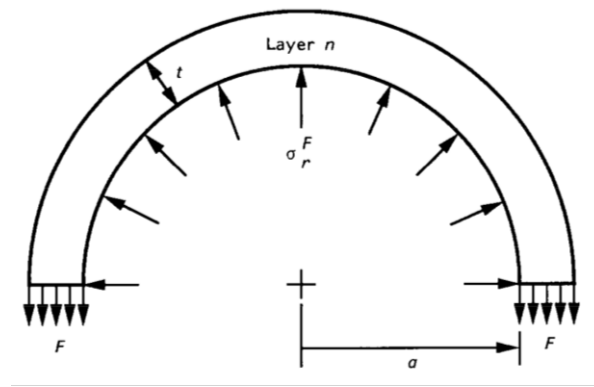


Figure 13: Force balance using winding tension from Cirino and Pipes [40]

Models for thin rings are similar to those of cylinders. The main difference is the assumptions made in the axial direction of the sample. Cirino and Pipes [40] are another research group who use the theory of elasticity and plane stress assumptions to build their model. Their equations consider only hoop-wound rings. What is interesting about their model is that they use the winding tension during manufacturing to calculate the radial stress and model the residual stress profiles in samples [40]. This boundary condition can be seen in Figure 13. Dedieu et al. [37] developed a parametric solution for determining the residual stresses in AFP manufactured rings. They had good agreement between their model and experiment results when overestimating the effective thickness of the plies. Their model built up the composite one layer at a time in 3 distinct steps. First, the substrate is heated, then the compressive force from the winding is applied, then finally the ring is cooled [37]. In a related paper, Dedieu et al. [39] developed a thermoelastic model to predict global residual stresses. They validated their model against a finite element Eulerian-Lagrangian model [39].

Using the sum of moments and the total stored strain energy, Srinath and Acharya [67] developed an equation to predict the bending stress in the ring in a solid ring. This model lined up closely with their experimental results, however, it is not specific to composite materials. This solution was considered as a possible alternative closed form solution that could be adapted using average laminate properties.

Large temperature gradients are known to cause visible distortion in AFP manufactured parts [46]. Several researchers are working to model these deformations in order to be able to predict their presence. Tafreshi et al. [34] modeled and experimentally measures the temperature gradient in carbon fiber reinforced PEEK samples. They used a heat transfer model which includes convection and conduction as modes of heat transfer. The aim of this experiment was to explain why large distortions occur in AFP manufactured samples. Their conclusion was that measured temperature gradient was significant contributed to the distortion. They validated their data with an experiment on an AFP machine, using carbon fiber reinforced PEEK prepreg tapes. The model showed the correct trends and maximal values, but failed to predict the correct rate of change for the temperature. Further research could link these temperature readings to residual stress measurements [34]. Fricke et al [46] designed a finite element model to predict the warping of flat laminates manufactured using AFP. This model included the heat transfer of the laser, as well as temperature dependant mechanical properties and crystallinity. In their experiment, they varied the temperature of the mandrel, they compared a heated mandrel to a room temperature mandrel. The FEA was able to more closely predict the results for panel deviations for the heated mandrel. This is likely due to the increased cooling rate of samples manufactured on the room temperature mandrel [46].

Laminate properties are another factor to consider when designing parts to be manufactured by AFP. Khan et al. [47] modeled how processing parameters like polymer viscosity, tape void content, roller set up and pressure, lay-up speed, temperature and laminate thickness impacted the degree of bonding and void content in carbon fiber reinforced composites. Their model consisted of thermal, consolidation, degradation, and degree of intimate contact sub-models. Their results could be used to optimize the properties of a manufactured part. The set of parameters would be dependant on the geometry of the final part. They validated their model against carbon fiber reinforced samples made using tape layup. Their predictions were within 20% their experimental values [47].

2.3 Annealing experiments

The work of the previous researchers was focused on predicting a sample's final stress state. The focus of the work presented in this next section is the modification of a sample's properties by means of annealing. This work is largely accomplished experimentally. Annealing is the process of heating and slow cooling a sample with the goal of relieving residual process stresses, recrystallizing the matrix, and otherwise modifying the sample's material properties [68]. This procedure is done regularly on metals and standards govern the annealing procedure for engineering metals like steel [69], aluminum [70], copper [71] and refractory alloys [72]. These standards suggest annealing times and temperatures for different alloy compositions [69], [70], [71], [72].

This process is not yet standardized for thermoplastic composites. The annealing schedule would depend on the thermoplastic in question, as well as the desired outcome. Several research groups are studying annealing and the possible impact on diverse properties like: tensile and ultimate strength [58], [61], fracture toughness [53], [73], shear properties [50], [51], [54], [56], [58], [59], flexural properties [48], [57], interlaminar shear [54], [56], [59], thermal properties [52], dielectric properties [60], crystallization [53], [56], [57], [58], [59], [60], [61], [74], and coefficient of thermal expansion [55]. There is significantly less work on residual stresses [13], [27], [41], [74], curvature [49], [63], and residual strains [74]. Even though many of the

experiments included are considering properties other than residual process stresses, they were retained because they still contained valuable data regarding the annealing temperature and hold time. The following paragraphs summarize the annealing experiments that were consulted when building the annealing schedule for this experiment. They are addressed thematically, grouping experiments studying similar properties.

2.3.1 Material and ultimate properties

The materials mechanical properties and properties at failure can be impacted by annealing [50], [51], [53], [58], [61]. The annealing temperature, hold time, and consolidation pressure all play an important role.

Annealing and cooling rates could possibly impact the tensile and ultimate properties of a material [61]. Cantwell, Davies, and Kausch [61] were looking to see how the cooling rate impacts mechanical properties like tensile strength, ultimate stress, and creep resistance. They considered 2 different stacking sequences of carbon fiber reinforced PEEK composite: $[90]_8$ and $[\pm 45]_{2s}$. In both cases, the samples with the slower cooling rate had a higher crystallinity. The crystallinity was measured using a DSC. For the $[90]_8$ laminate, they found that there was no relationship and failure stress, nor was there a relationship between cooling rate and creep response. For the $[\pm 45]_{2s}$ laminate, they found there to be no link between the cooling rate and failure stress. However, fast cooled sample had larger strain at failure and deformation in creep loading than slow cooled sample [61].

Fracture toughness is a failure property of the composite that is described by the energy released during failure [73]. Manson and Seferis [53] examined how autoclave processing parameters impacted carbon fiber reinforced PEEK composites. They investigated processing temperature, pressure and hold time. They performed DSC, micrograph, double edge notched test for fracture toughness. Samples heated to 382°C and above experienced the best consolidation and highest degree of crystallinity. Consolidation pressure also had a large impact on consolidation, while hold time did not. Processing above 350°C showed major improvements on fracture toughness, while neither of the other parameters had a consequential impact [53].

Interfacial shear strength describes the strength of the bond between the fiber and the matrix [50], [51], [58]. These interactions and stresses are present on a micromechanical scale. Wang et al. [50] measured the impact of annealing temperature on interfacial shear strength using the fiber pull-out test [50]. They noted that there was full or partial removal of residual stresses when annealed and slow cooled [50]. Gao and Kim [58] were also studying how the cooling rate impacts the crystallinity and as a consequence, the tensile properties and interfacial shear strength of their carbon fiber composite and neat PEEK samples [58]. They discovered that, as the cooling rate in °C/min increased, the percent crystallinity and interfacial shear strength of the samples decreased since the polymers did not have sufficient time to rearrange themselves into a crystalline structure [58]. Greisel et al. [51] also studied the impact of annealing on the results of a single-fiber push-out test. Annealing lead to an increase in interfacial fracture toughness and ductile failure mode. Unannealed sample exhibited a brittle failure mode [51].

2.3.2 Laminate properties

Flexural properties of samples can be measured using a 3-point bending test [48], [57]. Risteska et al. [57] used three-point bending test according to ASTM D-790 to determine the

flexural mechanical properties of the samples and concluded that the annealed samples had a flexural strength of 30% less than the autoclaved reference sample. They also used a DSC to determine the degree of crystallinity and microscopy to determine void content. They concluded that increasing annealing temperature did contribute to an increase in crystallinity in the samples and that the void content would need further investigation [57]. Xin, Shepherd, and Dearn [48], performed tests on carbon fiber reinforced PEEK samples to see how annealing, sterilisation and thermal ageing impacted the results of static and dynamic three-point bend tests [48]. The annealed samples showed higher yield strengths [48].

Interlaminar shear strength (ILSS) describes the bond between layers in the composite structure [56] [54] [59]. Mondo and Parfrey [54] compared the interlaminar shear strength of autoclaved, annealed, and in situ consolidated polyphenylene sulfide (PPS) composite samples. They also varied the manufacturing process parameters. In-situ samples had interlaminar shear strengths of between 80-85% those of the autoclave samples. Annealed samples had interlaminar shear strengths of about 90% those of the autoclave samples, which was a slight improvement over the in-situ samples [54]. Hoang et al. [56] compared in situ, annealing, vacuum bag and hot press manufacturing techniques to determine their respective impacts on the composites void content, crystallinity and interlaminar shear strength. They measured the degree of crystallinity using DSC, the void content by matrix digestion and the interlaminar shear using a short beam shear test. All three forms of post treatment showed large increase in crystallinity when compared to the in-situ sample. Annealing did not significantly improve void content nor interlaminar shear strength, while hot press and vacuum bag did. Hot press showed the best improvement [56]. El Kadi and Denault [59] wanted to determine the impact of manufacturing parameters (including cooling rate) on short beam shear test, 3-point flexural fatigue test of carbon fiber reinforced PEEK samples made using compression moulding. As expected, slower cooling rates created samples with higher crystallinity. Rapidly cooled then annealed sample allowed for intermediate amount of crystal growth. Increasing the cooling rate caused a decrease in short beam shear strength. Annealing to 150°C was not enough to increase the short beam shear strength, but annealing at 230°C increased it slightly. Fatigue tests to preliminary to draw definitive conclusions [59].

2.3.3 Thermal properties

Annealing is also known to impact thermal properties like the glass transition temperature [52], dielectric properties [60] and the coefficient of thermal expansion [55]. Cebe [52] was studying how annealing low molecular weight PEEK and commercially available PEEK impacts how they melt. Differential scanning calorimetry was used to collect data. Annealed samples exhibited higher glass transition temperature and density [52]. Giants [60] was working to determine how annealing, and as a consequence, crystallinity, impacted the dielectric properties of neat PEEK. Annealing above the glass transition temperature, but below the melting temperature, contributed to a large increase in crystallinity [60]. The conductivity of the samples decreased as the crystallinity increased [60]. Lebrun and Denault [55] studied how annealing different matrix and fiber combinations impacts the coefficient of thermal expansion and residual stresses of the samples. For the carbon fiber reinforced PEEK sample, no thermal expansion was observed when the sample was heated beyond 180°C. The sample only experiences thermal contraction. This means that they were successful in making a sample with reproduceable expansion behavior [55].

2.3.4 Process residual strains

All of the experiments listed previously involve designing an annealing cycle to modify laminate or material properties. None dealt with residual strains of any kind. This section contains experiments focused on reducing the residual process strains and deformation from samples. There are few experiments broaching this topic when compared to the previous sections.

Residual stresses and strains can also be impacted by the thermal history of manufactured parts. Unger and Hansen [74] were studying the internal strains in unidirectional samples made from carbon fiber reinforced PEEK. They measured the strain of the samples using embedded strain gauges as they recrystallized. Samples were first quenched then annealed at temperatures between 170°C and 300°C. A cooling and heating rate of 2°C/min was used. The expansion of the samples due to their coefficients of thermal expansion was reversed as the samples cooled, while the strains due to crystallization remained. As the anneal temperature increased, the residual strains due to recrystallization grew [74]. This is a combination of micromechanical (due to crystallization) and process induced strains. Schlottermuller et al. [13], [27] performed a parametric study to determine the impact of mandrel heating, annealing, tape material, presence of a liner, winding angle, tape force, and number of layers on the residual stresses of AFP wound tubes. They studied carbon fiber reinforced PEEK and PP rings. Residual strains were measured using strain gages when the rings were slit open [27]. This experimental setup can be seen in Figure 14. Annealing was found to have some impact on overall residual stresses, while wind angle was found to have the biggest impact [13], [27]. Researchers did not differentiate between process and macro-mechanical strains in this case.

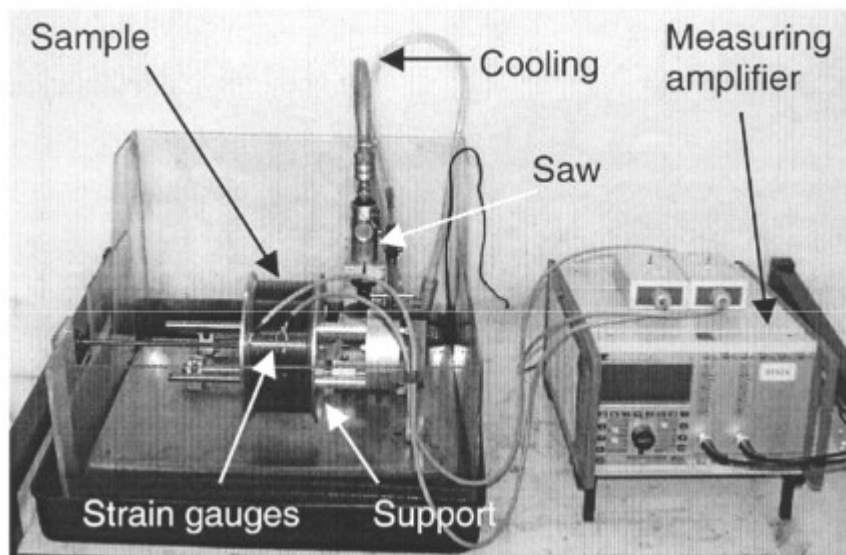


Figure 14: Experimental jig for measuring residual strains in split ring experiment by Schlottermuller et al. [27]

Residual stresses profiles in thick laminate are impacted by the sample cooling rates during annealing. With high cooling rates, the surfaces cool at a faster rate than the core of the samples, causing residual tensile stresses within samples [62]. This is a classic example of residual process strains. Tsukada et al. [62] used fiber Bragg grating sensors and three-point bending tests to compare the residual stress profiles of thick samples for 3 different cooling rates. It was not possible to undo the skin-core using annealing [62].

The overall geometry of a part can be altered by annealing. Researchers Unger and Hansen [49] were looking at reducing the curvature in flat samples manufactured by compression molding. This experiment resembles the one presented here the closest, but uses a different manner of manufacturing and sample geometry. Unger and Hansen [49] performed an experiment aimed at determining how the annealing cooling rate affects curvature. This is an investigation of residual process stresses. They were studying stiffened antisymmetric [0/90] laminates made from carbon fiber reinforced PEEK. The stiffening forced curvature along a single axis of the samples, simplifying the measurements. A sketch of the stiffened panels and the jig for measuring curvature can be seen in Figure 15. During annealing, samples were placed in an oven until temperature equilibrium was reached, then they were clamped for a designated dwell time. They tried temperatures between 25-200°C and dwell times between 1-146 minutes. They found that the cooling rate had the largest impact on the parts curvature. As the cooling rate decreased, so did the curvature. The most stress relaxation was found at around the glass transition temperature (T_g), increasing the temperature above T_g did not appreciably increase the stress relaxation in the part. They managed to achieve a maximum of 18.2% reduction in curvature at 125°C and when clamped for 146 minutes [49]. Valvez et al. [63] were looking at how annealing temperature and time impact radius of curvature, volume variation, hardness, bending stress and bending modulus of PETG when reinforced with carbon and aramid fibers. The sample radii calculated using measurements taken on a profile projector. They studied temperatures between 90-130°C and times between 30-480minutes. Changes in the radius of curvature were only noted at 130°C and 240min and 480min for the carbon fiber sample [63]. The data collection of this sample was clever, but unfortunately the annealing parameters were for PETG and not PEEK.

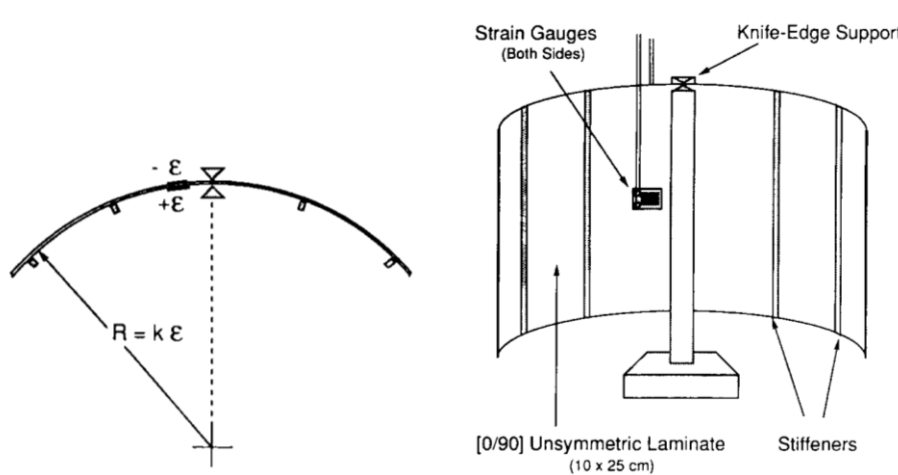


Figure 15: Curvature measurement fixture from Unger and Hansen [49]

2.4 Possible impact of research

Of all the annealing experiments included in this overview, Unger and Hansen [49], Valvez et al. [63], and Schlottermuller et al. [13], [27] were the only research groups dealing specifically with shape control or residual stress reduction by annealing of thin composite plates or cylinders. However, none of these experiments achieved what is being done here. Unger and Hansen had limited success with stiffened samples [49], Valvez et al. worked with flat PETG composite samples [63]. Neither of these experiments treated cylindrical geometries [49], [63]. Schlottermuller et al. did treat cylindrical geometries, but was weighing the benefits of annealing

with other processing parameters rather than isolating its impact [13], [27]. The most important takeaway from these experiments was their data collection methods. Radius could be measured optically [63], while the strains could reliably be measured using strain gages [13], [27], [49].

The experimental work from sections 2.3.1 to 2.3.3 was focused on quantifying changes in other laminate properties like bending or shear strength, which are not the goal here. However, the experiments treating PEEK were retained because they contained a starting point for designing an annealing cycle. All of the previously mentioned numerical and FEA models predict and quantify the residual stresses, but do little to reduce them. Attempting to reduce the residual stresses is where this work distinguishes itself.

Some cylindrical parts like pressure vessels and aircraft are designed specially to exhibit a particular pattern of residual stresses which can help to counter the load specific to that application. For example, to counteract the internal pressure that pressure vessels are subject to, a compressive residual stress profile can be designed [27]. Aircraft fuselages are another highly engineered cylindrical form that can be made using AFP [4], [8]. Composites have become increasingly attractive for this application because their lightweight nature can help improve the fuel efficiency of airplanes [4]. For aircraft parts made from traditional engineering materials like aluminum, the residual stress profile can be tailored using heat treatments, machining, rolling and surface treatments [75], [76]. If manufactured using composites, the residual stress profile could potentially be managed using the manufacturing processing parameters [35] and the sample layup [10]. For applications like these, it is important to be able to distinguish between the unintended residual process stresses caused by the large temperature gradients inherent to the AFP manufacturing procedure, and the desired residual stress profile. If this work is successful, then the process stress would be eliminated, leaving behind only the tailored process-independent stress profiles.

Chapter 3: Design of heat treatment cycle using flat panels

The experiments presented here were carried out in multiple stages. First, the annealing cycle was designed to remove the process dependent residual stresses. At this stage, panels that had been manufactured on a flat mandrel and warped were used. Annealing parameters were taken from experiments presented in the literature review. Once an adequate procedure could be designed for flat samples, the annealing procedure was extended to thin rings. Finally, the void content, fiber volume fraction, and crystallinity of the laminates was measured to assess the impact of annealing on these quantities. All the samples manufactured here were carbon fiber reinforced polyether ether ketone (PEEK).

The first step of this study was to develop an annealing cycle with an appropriate temperature and duration to relieve the residual process stresses in AFP manufactured parts. The goal was a cycle that could be completed within one workday. Trials were first conducted on warped unidirectional laminates. These laminates were selected because the micromechanical and macro-mechanical stresses should be relatively small when compared to the process induced stresses. These process induced stresses, brought on by the uneven heating and cooling of the AFP process, are what cause the visible warping on what should be flat panels.

3.1 Selecting annealing cycle parameters

Annealing experiments from other research groups were used as a starting point. The goal at this stage was to get an idea of what annealing temperatures and times worked best for other researchers. This experiment is focused on residual stresses. However, the scope of the research was opened to experiment concerning mechanical properties, part geometry and thermal properties because few experiments were solely focused on residual stresses. A summary of all the experiments consulted can be seen in Table 1. Composites reinforced with carbon fiber (CF), glass fibers (GF) were included. PEEK matrix composites were prioritized in the search, but some other thermoplastics like polyphenylene sulfide (PPS), polyether ketone ketone (PEKK), and polypropylene (PP) were also included.

However, the annealing cycles parameters chosen by each research group varied significantly in their hold times and temperatures. The glass transition temperature of PEEK is 143°C [77] and it has a range of processing temperatures from 385 °C to 400°C [77]. The annealing temperature was expected to be somewhere between the glass transition and processing temperatures. Given that the goal was to develop an out-of-autoclave procedure, temperatures below 250°C would be preferable since they could be achieved in an oven. Anything above would require autoclave processing. Heat blankets were considered in addition to an oven because of their versatility and the possibility for doing repairs [78].

Many researchers had annealing temperatures in the 100-200 °C range which was encouraging [49], [49], [50], [57], [59], [74]. Several had most success in temperatures near the glass transition of their respective thermoplastic and saw little improvement in increasing their processing temperature much above that value [48], [49], [52], [53]. As a starting point, 200°C was selected to be the oven temperature. This temperature could be readily achieved in the Thermo Scientific programmable table-top oven available for the experiment. This temperature is also achievable with a heat blanket, which is an alternative out-of-autoclave option. A 360W heater from BriskHeat (SRL06241PADL) was used. It could achieve a maximum temperature of 400°F (204°C) and has an active area of 6” by 24”.

Table 1: Experiments consulted when designing annealing cycle

#	Testing procedure	Properties measured	Material	Annealing Temperature	Dwell Time and Heating/Cooling Rate
Mechanical tensile properties, shear properties and failure properties					
[48]	Static and dynamic three-point bending	Failures strength	CF PEEK	250°C	4h
[57]	Three-point bending	Flexural mechanical properties	CF PEEK, PPS	75°C 100°C 150°C	1h
[59]	Short beam shear test, 3-point flexural fatigue test	Failure strength and elastic modulus	CF PEEK	150°C 230°C	1h
[61]	Tensile test, scanning electron microscope	Tensile strength, ultimate stress, and creep resistance	CF PEEK	380°C	1°C/min 50°C/min
[50]	Fiber pull-out	Interfacial shear strength	CF PPS droplets	80°C, 100°C, 110°C, 120°C, 150°C, 230°C	12h 6-7h
[51]	Fiber push-out test	Interfacial fracture toughness	CF PPS	320°C, 135°C, 230°C	15 minutes 10°C/min
[53]	Microscopy, DSC, double edge notch	Laminate quality and fracture toughness	CF PEEK	350°C, 366°C, 382°C, 400°C	15, 30, 45 minutes
[56]	Matrix digestion, DSC, short beam shear	Void content, crystallinity and interlaminar shear strength.	CF PEKK	270°C	2h 40°C/min
[54]	Short beam shear	Interlaminar shear strength	CF PPS	204°C	2h
[58]	DSC, x-ray spectroscopy, tensile testing, fiber pull-out	Crystallinity, tensile properties and interfacial shear strength.	CF PEEK		1°C/min, 70°C/min, 160°C/min, 600°C/min, 1000°C/min, 15000°C/min

Strain and part geometry					
[49]	Strain gage	Curvature	CF PEEK	25°C, 100°C, 125°C, 150°C, 175°C, 200°C	1, 6, 16, 46, 146 minutes
[13] [27]	Strain gage	Residual stresses	CF PEEK, GF PP	90% of T _c (crystallization temperature)	20 minutes
[74]	Strain gage	Strain of crystallization	CF PEEK	170°C-300°C	2°C/min
Thermal and electrical properties					
[60]	DSC	Dielectric properties	PEEK	160°C, 210°C, 260°C, 310°C	1h 2h
[52]	DSC	Melt properties	PEEK	230°C, 206°C, 302°C	24h

Some groups held their annealing temperature for one hour or less [13], [27], [49], [53], [57], [59], [60]. Others held their annealing time for up to a day [52]. A hold time of 12 hours was chosen as a starting point because it lies in the middle of this wide range of times. After an initial test at with a 12-hour hold, the goal would be to reduce the annealing hold time such that the cycle could be completed in a single workday.

Cooling rate was considered to be more critical than the heating rate since cooling is when the thermoplastic would crystallize. Given that few experiments specified their cooling rates [51], [56], [58], [61], [74], the default slow cooling rate for the oven was selected. This value was around 2°C/min, but slowed as the samples approached room temperature. As for vacuum bag pressure, 15 torr was selected as the recommendation of Concordia Center for Composites (CONCOM) manufacturing staff. To determine if the initial annealing processing parameters of 12h at 200°C and 15 torr was sufficient, an initial trial was conducted. The processing parameters for each trial and the specification of each laminate can be seen in Table 2. For the layups, ‘Symm.’ refers to a symmetric laminate, while ‘Uni.’ refers to unidirectional panels. No additional weight or caul plate was placed on the samples during annealing.

Table 2: Annealing processing parameters for flat samples

	Layup	# of Layers	Sample Size (cm)	Heat Application	Anneal Temp.	Bag Pressure (torr)	Hold Time (h)	Heating Rate (°C/min)	Cooling Rate (°C/min)
1	Symm.*	15	23 × 24	Oven	200°C	15	12	7.6	0.5-2.25
2	Uni.	4	28 × 11	Oven	200°C	15	3	7.6	0.5-2.25
3	Uni.	4	28 × 11	Oven	200°C	15	3	7.6	0.5-2.25
4	Uni.	12	15.5 × 15.5	Oven	200°C	15	3	7.6	0.5-2.25
5	Uni.	12	26 × 15	Heat blanket	165°C	15	3	0.57	1.63

* [0₂/+45/90/-45/0/+45/90]_s

To determine how repeatable the process was and to isolate the impact of temperature, hold time, layup orientation, thickness, and method of heat application, 5 trials were performed. The first trial consisted of an unbalanced symmetric sample with a layup of [0₂/+45/90/-45/0/+45/90]_s. This sample was 15 layers thick and the 90° layer was the midplane of the layup.

This sample would isolate the impact of layup on annealing. This sample had a maximum deflection of 8.5mm in one corner. Trials 2 and 3 had identical annealing parameters on samples 4 layers thick. The goal here was to determine the repeatability of the annealing procedure. Thicker samples were used in trials 4 and 5. The impact of the sample thickness could be ascertained by comparing trials 4 and 5 to 2 and 3. Additionally, trials 4 and 5 were annealed using an oven and heat blanket respectively. Comparing these trials would show which heat application method was most suitable.

The movement of the AFP head as it deposits tape causes uneven thermal gradients in the manufactured parts. This difference in temperature means that some areas of the sample will cool faster than others. The constraint imposed by the already solidified thermoplastic on adjacent sections which are still cooling is what creates these residual process stresses. For samples that should be flat, removing this visible deformation is analogous to removing the residual stresses.

The preliminary experiments involved several steps. First, it is necessary to quantify flatness and what kind of variation is acceptable in the aerospace industry. The sample geometry must then be measured, and the data imported for analysis. It is also important to establish that the measurement method is repeatable. To be able to compare the samples to one another, the curvature of the samples before and after annealing must be calculated. From the curvature, the relative success of the annealing cycles can be ascertained.

3.2 Flatness condition

To establish whether a cycle was effective, it was important to discuss the meaning of flatness. Recommended flatness tolerances for thermoplastic composite materials are not well documented. The International Organization for Standardization (ISO) defines flatness as a geometric tolerance that is “limited by two parallel planes a distance t apart” [79]. An illustration of this definition can be seen in Figure 16. This means that all the points that make up that surface must fall within the range specified by the dimension ‘ t ’. This definition holds, regardless of the material. The range can vary depending on the part’s application.


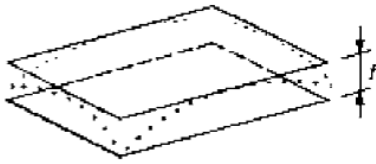

Symbol	Definition of the tolerance zone	Indication and explanation
	 <p>(a)</p>	 <p>(b)</p>

Figure 16: Definition of flatness tolerance by ISO (left) and flatness callout for technical drawings (right) [79]

The ISO standards do present a list of recommended flatness tolerances for machined metal parts in ISO 2768-2 [80]. A summary of those standards can be seen in Table 3. If these standards were going to be applied to this experiment, given that the samples are between 100 and 300mm, the widest tolerance acceptable according to this standard is up to 0.8mm [80]. This was determined to be an unrealistically small target for this experiment. As of now, ISO does not have suggested standards for any polymers [80].

Table 3: Straightness and flatness recommended tolerances in mm [80]

Accuracy grade	Straightness and flatness tolerances for ranges of nominal length					
	to 10	over 10 to 30	over 30 to 100	over 100 to 300	over 300 to 1000	over 1000 to 3000
H	0.02	0.05	0.1	0.2	0.3	0.4
K	0.05	0.1	0.2	0.4	0.6	0.8
L	0.1	0.2	0.4	0.8	1.2	1.6

ASTM International, another well known standards organization, does have some composite related standards, including: ASTM D3917-15a Standard Specification for Dimensional Tolerance of Thermosetting Glass-Reinforced Plastic Pultruded Shapes [81], and ASTM D5687/D5687M-20 Standard Guide for Preparation of Flat Composite Panels with Processing Guidelines for Specimen Preparation [82]. Unfortunately, neither of these standards specifies standards for thermoplastic flat plates [53], [54]. ASTM D3917-15a [81] includes dimensional and angular tolerances for thermoset shapes made using pultrusion, including flat sheets. For a sample 200mm (0.2m) long, a variation of 0.5mm would be permitted. This may be a reasonable value for thermoset plastics because of their superior dimensional stability [3], however, for thermoplastics, this may not be a reasonable target.

ASTM D5687/D5687M-20 [82] suggests a flatness of 0.05mm (0.002 inches) for molds used to manufacture composites [82]. The standard does not specify a tolerance for the completed composite parts [82]. The National Institute for Aviation Research has a similar set of recommendations: flatness tolerance of 0.002 inches for the mold and none for the completed composite part [83]. Other experiments measuring warpage in samples see deviations from 0.15-2mm with no standard to compare them to [18], [84]. Part of the difficulty in specifying tolerances for composite materials is that the tolerance must be a multiple of the ply thickness [85]. For this experiment, the 0.8mm tolerance from ISO 2768-2 and the 0.5mm tolerance from ASTM D5687/D5687M-20 will be used as a starting point despite being quite an ambitious target.

3.3 Surface characterization

The shape of the samples was characterized by determining the coordinates of points on the surface of the samples. These coordinates were determined using a laser measuring system. The laser measuring system (LMS) is a measuring tool that allows a user to collect 3D geometry data from a sample up to 20 cm long, 20 cm wide, and 40cm tall. The instrumentation setup can be seen in Figure 17. The system consists of a MAD12D platen from TSUN electronic and Keyence LK-G402 laser. Measurements are recorded using LK Navigator software. Samples are affixed to the platen using a threaded hole at its center. The laser is aligned with this origin. The platen allows users to move the sample in the x and y directions as indicated in Figure 17. The laser is used to measure the distance to the sample. In order to obtain the height of the sample rather than the distance between the sample and the receptor, the distance to the platen was measured and used to offset all the z values.

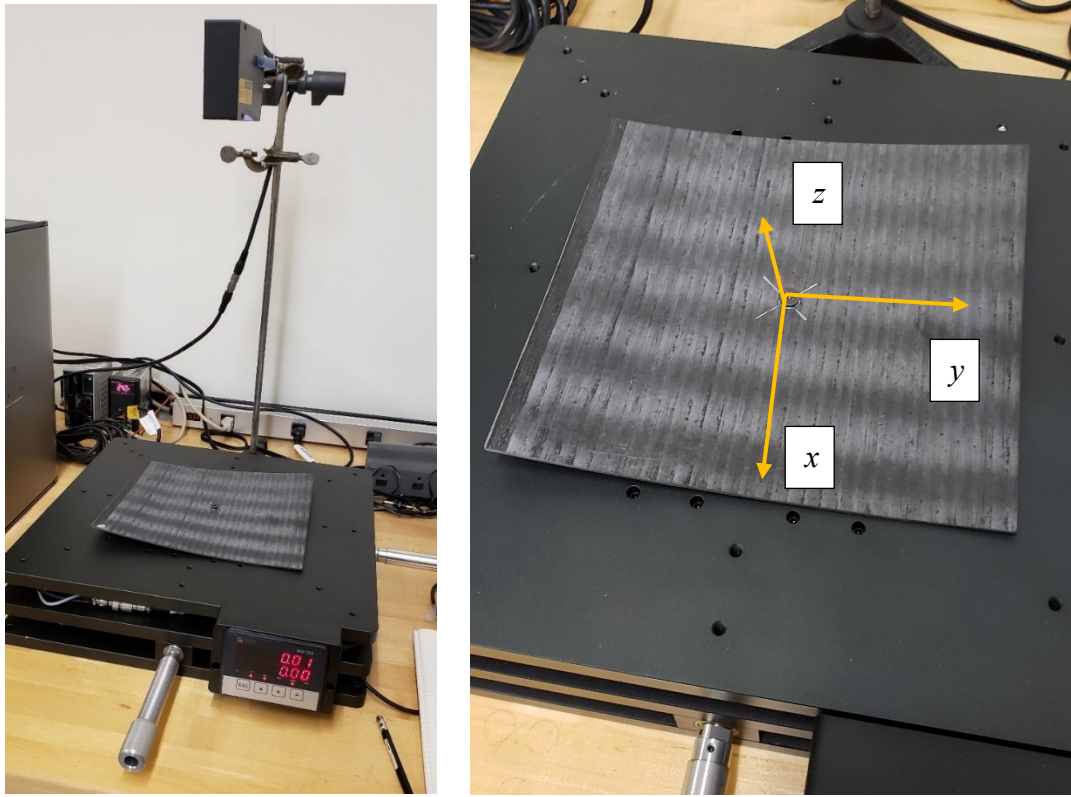


Figure 17: Laser measuring system experimental set-up (left) and coordinate system (right)

3.3.1 Stability test

Given the single fixture point in this system, there was concern about the repeatability of the measurements. Samples needed to be measured, annealed, and measured a second time. With each installation on the platen, there could be slight variations in how the part is rotated about the center hole. In order to address this concern, a sensitivity study was performed.

This sensitivity study involved measuring the z value of 7 points on the surface. The values $x = 0, \pm 20\text{mm}, \pm 40\text{mm}, \pm 60\text{mm}$ were measured along the line $y = 20\text{mm}$. These measurements were taken 6 times. Between each set of measurements, the sample was completely removed from the platen and then replaced on the platen to simulate measurements taken before and after annealing. The experimental set-up can be seen below in Figure 18. The sample variance and sample standard deviation were then calculated at each point to determine the spread in the data.

The sample variance is described by the sum below [86].

$$s^2 = \frac{\sum_{i=1}^n (z_i - \bar{z})^2}{n - 1} \quad (1)$$

The sample standard deviation is simply calculated by taking the root of the sample variance [86].

$$s = \sqrt{s^2} \quad (2)$$

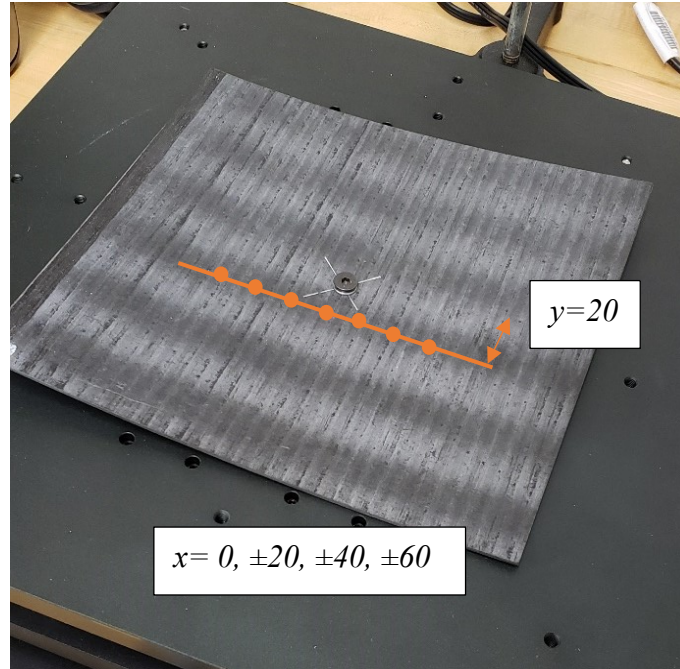


Figure 18: Set up for sensitivity test

The results for this validation test can be seen in Table 4. The z-values recoded in each trial are plotted in Figure 19. The average sample standard deviation for all of the measurements was of 0.036mm. Given that this standard deviation is within 2% of the smallest z measurement (1.79mm), the variation was deemed to be sufficiently small for the purposes of this experiment. This confirms that when carefully aligning the edge of the sample such that it is parallel to the edge of the platen with each installation, repeatable measurements before and after annealing can be gathered. It is indeed possible to consistently hit the same points along its surface. Thanks to this validation, the LMS was retained as a measurement method for this preliminary experiment.

This validation was simply performed on the measured z values to see if the offset between measurements was significant. Looking ahead, the curvature calculations presented in the next sections are partial derivatives. This means that the offset, which is already small, will vanish with the derivatives performed.

Table 4: Standard deviation data with adjusted z

x	y	adjusted z (mm)						AVG z	Standard Deviation
		Trial 1	Trial 2	Trial 3	Trial 4	Trial 5	Trial 6		Sample
-60	20	4.32	4.39	4.41	4.41	4.39	4.36	4.38	0.0316
-40	20	3.10	3.18	3.19	3.20	3.17	3.11	3.16	0.0389
-20	20	2.24	2.34	2.34	2.24	2.25	2.30	2.29	0.0439
0	20	1.82	1.84	1.85	1.89	1.85	1.88	1.86	0.0236
20	20	1.79	1.80	1.79	1.81	1.88	1.79	1.81	0.0321
40	20	2.14	2.20	2.15	2.18	2.27	2.24	2.20	0.0464
60	20	2.84	2.82	2.86	2.90	2.91	2.92	2.88	0.0373
								AVG	0.036

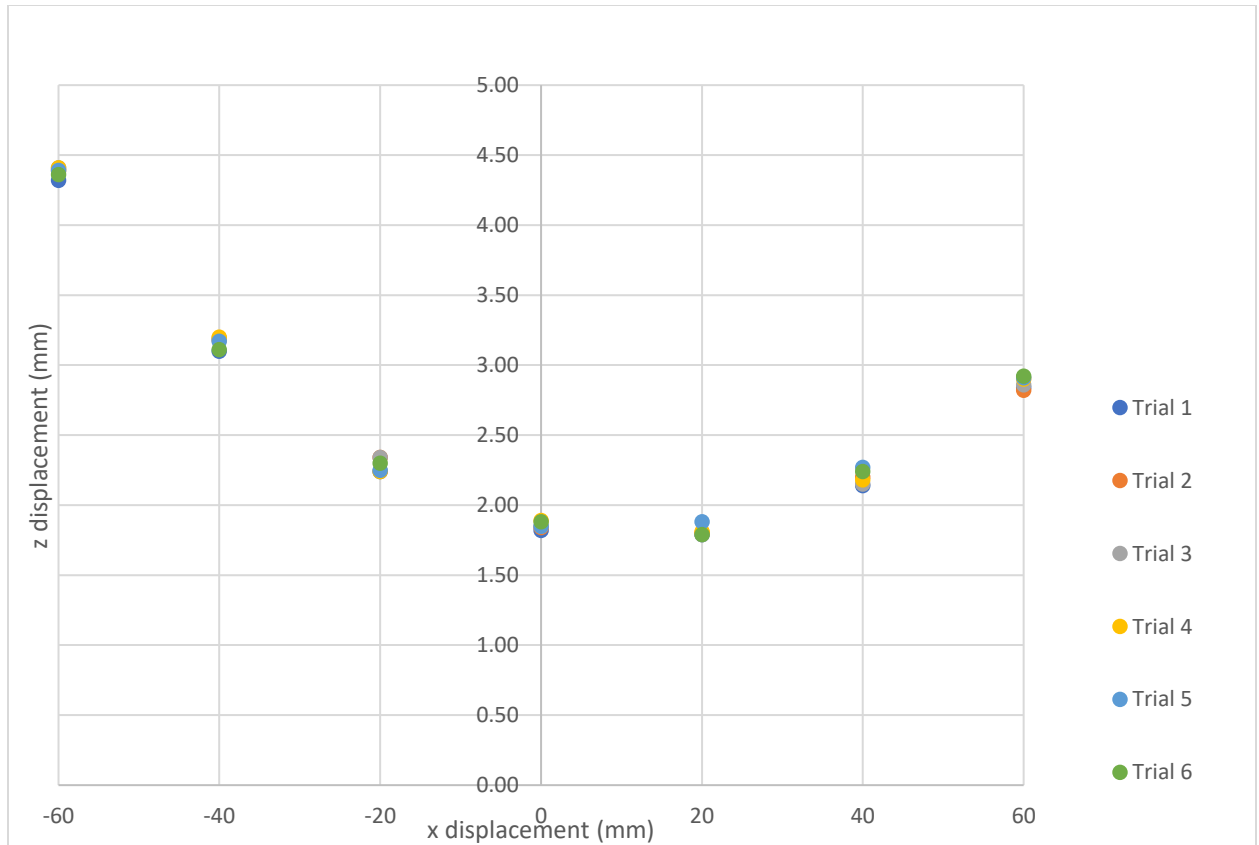


Figure 19: Adjusted height of surface for sensitivity experiment

3.3.2 MATLAB's curve fitting toolbox

MATLAB has a built-in app called 'Curve Fitting Toolbox.' This app uses the input data and calculates the coefficients for the fit function selected by the user. This app was used to find the model that best fits the measured geometry data and assess the goodness of fit of the considered equation because of its versatility and ease of use. The measures of goodness of fit that are calculated by the toolbox are outlined in the next section.

3.3.3 Function validation

Once all the 3-dimensional surface data was gathered using the LMS, it became necessary to select a mathematical function that most closely matched the curve of the surfaces. From these functions, the curvature will then be calculated. To begin, a visual inspection of the samples was performed. As a reference, the sample from trial 3 (4 layers thick and unidirectional) can be seen in Figure 20 and Figure 21. Note that these photos were taken before annealing. From these photos, it looks as though the sample has a significant curvature along its shorter length (perpendicular to the fiber direction), and a weaker curvature along its longer dimension (in the fiber direction). This would suggest that a polynomial of x and y to the second power would be necessary.



Figure 20: Top view of sample from trial 3 before annealing, 4 layers unidirectional



Figure 21: Side view of sample from trial 3 before annealing, 4 layers unidirectional

The equation for a second-degree polynomial in x and y was used to characterize the surface is of the form seen below where $c_1, c_2, c_3, c_4, c_5, c_6$ are constant. When the fit equation was calculated for the sample from trial 3, it gives the results seen in Figure 22.

$$z = c_1 + c_2x + c_3y + c_4x^2 + c_5xy + c_6y^2 \quad (3)$$

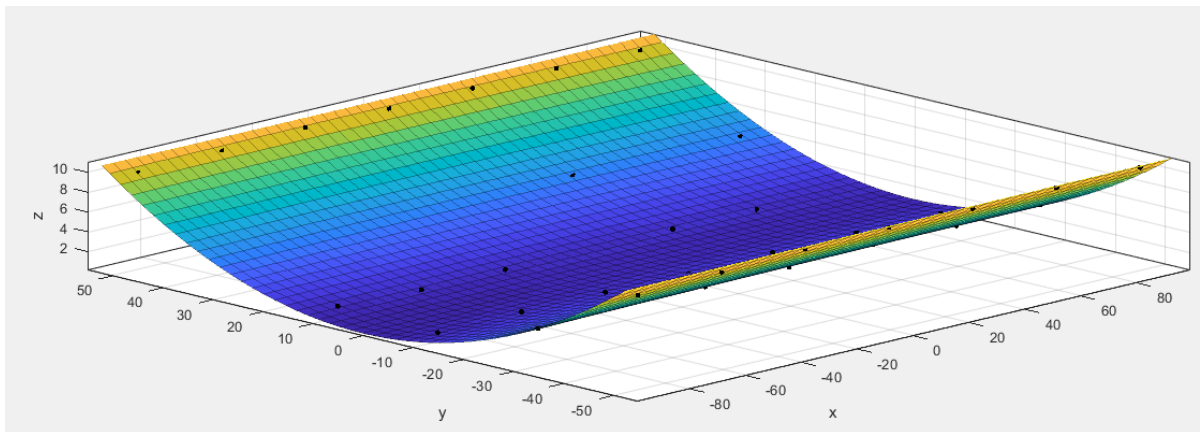


Figure 22: MATLAB fit function for sample from trial 3 before annealing, axes are in mm

As a validation, a test was conducted by increasing the degrees of both x and y from 1 to 5 to see how the number of terms impacted the goodness of fit. adjusted R-squared and root mean squared error (RMSE) were used as measures of goodness of fit. Ideally, these values should approach 1 and 0 respectively [87],[88].

There was no significant improvement in the RMSE seen in Table 6 nor the adjusted R^2 seen in Table 5 when the polynomials were increased past the second degree. The second-degree polynomial was necessary to achieve an adjusted R^2 value of 0.999. Higher order polynomials only served to improve the fourth decimal place. For the RMSE values, the second-degree polynomial was able to achieve 0.0457 which was deemed sufficiently small given the magnitude of the dimensions measured.

Table 5: Adjusted R^2 for different degrees of x and y. This fit contains 41 points

		x^n				
		1	2	3	4	5
y^n	1	0.0144	0.9625	0.9604	0.958	0.9552
	2	0.5314	0.9994	0.9995	0.9996	0.9995
	3	0.5041	0.9994	0.9995	0.9996	0.9995
	4	0.5787	0.9996	0.9996	0.9996	0.9995
	5	0.5795	0.9995	0.9996	0.9995	0.9995

Table 6: RMSE for different degrees of x and y. This fit contains 41 points

		x^n				
		1	2	3	4	5
y^n	1	1.9314	0.3767	0.3872	0.3989	0.412
	2	1.3317	0.0457	0.0427	0.0393	0.0414
	3	1.3699	0.0461	0.0433	0.0401	0.043
	4	1.4188	0.0439	0.0401	0.0408	0.0431
	5	1.4566	0.0442	0.0407	0.0426	0.00436

3.3.4 Curvature equations

The curvature can then be calculated from the fit function provided by the Curve Fitting Toolbox. The equation of the plane is first parametrized in terms of u, v .

$$\begin{aligned} z &= c_1 + c_2x + c_3y + c_4x^2 + c_5xy + c_6y^2 \\ r &= [u, v, c_1 + c_2u + c_3v + c_4u^2 + c_5uv + c_6v^2] \end{aligned} \quad (4)$$

The partial derivative with respect to u and with respect to v of this vector are respectively described below.

$$\begin{aligned} r_u &= [1, 0, c_2 + 2c_4u + c_5v] \\ r_v &= [0, 1, c_3 + c_5u + 2c_6v] \end{aligned} \quad (5)$$

These partial derivatives can be used to compute the unit normal vector at a point. Note that \times represents a cross-product [89].

$$\hat{n} = \frac{r_u \times r_v}{|r_u \times r_v|} \quad (6)$$

The partial derivatives can also be used to describe E, F, G from the first fundamental form of the surface [89], [90], [91]. Note that \cdot represents a dot product, and so E, F, G represent functions, and not vectors.

$$\begin{aligned} E &= r_u \cdot r_u \\ F &= r_u \cdot r_v \\ G &= r_v \cdot r_v \end{aligned} \quad (7)$$

The second partial derivatives of the vector r can be computed as follows.

$$\begin{aligned} r_{uu} &= [0, 0, 2c_4] \\ r_{vv} &= [0, 0, 2c_6] \\ r_{uv} &= r_{vu} = [0, 0, c_5] \end{aligned} \quad (8)$$

The second partial derivatives and the unit normal vector shown above can be used to calculate L, M, N from the second fundamental form of the surface [89], [91]. As previously stated, \cdot represents a dot product. As a consequence, L, M, N will represent functions rather than vectors.

$$\begin{aligned} L &= r_{uu} \cdot \hat{n} \\ M &= r_{uv} \cdot \hat{n} \\ N &= r_{vv} \cdot \hat{n} \end{aligned} \quad (9)$$

From the functions E, F, G and L, M, N it is possible to calculate the Gaussian and the mean curvature of the surface at any point. The equation for the Gaussian curvature, K , can be seen below [91]. The Gaussian curvature is the product of the 2 principal curvatures at that point on the surface [90], [91]. Given that the fit equation has a unit of mm , the Gaussian curvature has a unit of $\frac{1}{mm^2}$ which is an abstract unit and hard to visualize. The Gaussian curvature is mainly used to determine the direction of the curves and the resulting function shape [90].

$$K = \frac{LN - M^2}{EG - F^2} \quad (10)$$

The equation characterizing the mean curvature, H , can be seen below [91].

$$H = \frac{EN + GL - 2FM}{2(EG - F^2)} \quad (11)$$

The mean curvature is the average of the 2 principal curvatures at that point [90], [91] and in this case has a unit of $\frac{1}{mm}$. The reciprocal of the mean curvature is the radius of curvature, which is easier to visualize and can serve as a way to validate that the order of magnitude of the equations was correct.

3.4 Final cycle parameters

Once the stability of the measurement system was assessed and the equations finalized, the samples could be annealed. The samples in the first 4 experiments were all vacuum bagged with a breather and bagging film and placed in the HERATHERM tabletop oven from Thermo Scientific. Release film was not necessary since the samples were not going to achieve their melting temperatures. For the fifth sample, a layer of release film was placed between the sample and the heat blanket. This assembly and an external thermocouple were then vacuum bagged to a flat tool. This assembly was insulated from the work surface and ambient air with wood and several layers of thick breather. This assembly can be seen in Figure 23. Despite being set to its maximum temperature of 400°F (204°C), the sample reached a steady hold temperature of 165°C. This is likely due to the limits of the insulation and the heat transfer to the surroundings.

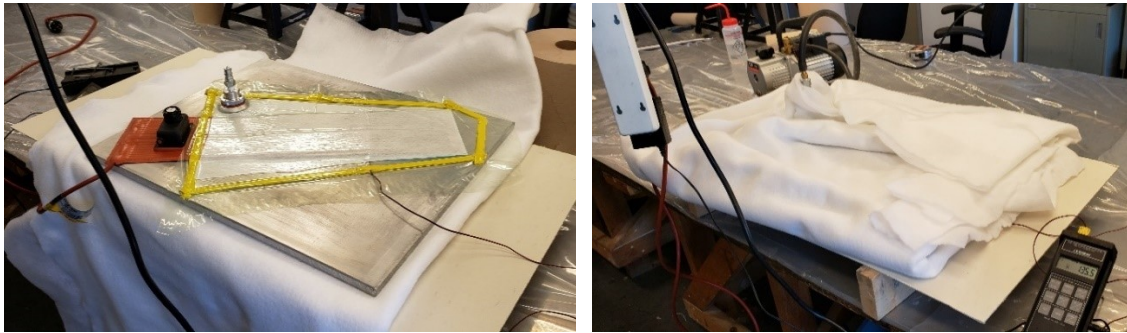


Figure 23: Vacuum bag assembly for heat blanket experiment

3.5 Results and discussion

Once the different heat treatment trials were complete, the impact of temperature, hold time, and method of heat application could be assessed for the flat samples. The number of datapoints in each fit equation is also noted. The Gaussian and mean curvatures were evaluated at 10mm intervals over the surface of the sample. The curvature values were then averaged to generate the data seen in the below tables. Due to its layup, the symmetric sample from experiments 1 had 2 stable mode shapes. These curvatures were characterized separately. Overall, the symmetric sample saw much less improvement than the unidirectional samples despite its longer hold time.

Table 7: Gaussian curvature before and after heat treatment

	Layup	# of layers	# of points in fit	Gaussian curvature (K)	
				Before H.T. (1/mm ²)	After H. T. (1/mm ²)
1, 1	Symmetric	15	48	5.434×10^{-8}	6.333×10^{-8}
1, 2		15	48	8.640×10^{-8}	6.679×10^{-8}
2	Unidirectional	4	42	9.395×10^{-8}	9.861×10^{-9}
3	Unidirectional	4	42	-1.399×10^{-7}	-9.318×10^{-9}
4	Unidirectional	12	42	5.049×10^{-7}	2.131×10^{-8}
5	Unidirectional	12	49	1.885×10^{-7}	2.358×10^{-8}

The Gaussian curvature for each sample can be seen in Table 7. Given that Gaussian curvature is the product of the principal curvatures of a point rather than the sum, it does not provide any direct insight into the sample's geometry. Instead, the Gaussian curvature provides insight into the shape and concavity of the surface. The negative Gaussian curvature values seen in trial 3 indicates that the sample is saddle shaped [90] and that the two principal curvatures are of opposite concavity. All of the other samples were elliptical paraboloids [90].

The results for the mean curvature can be seen in Table 8. The mean radius of curvature, which is the reciprocal of the mean curvature can be seen in Table 9. Samples look increasingly flat as the mean curvatures decreases and the mean radius of curvature increases. The unidirectional samples saw improvements of their mean curvatures of between 86% and 90%. This range is rather narrow and would indicate that the procedure is repeatable. Additionally, the 4-layer samples from experiments 2 and 3 saw a slightly larger reduction than the 12-layer samples from trials 4 and 5. The 4-layer samples had 89-90% improvements, compared to 86-87% for the 12-layer ones. Given the small sample size here and the accuracy of these measurements, this difference is not statically significant. The samples in experiments 2 to 5 all experienced a 3-hour hold, and these results would indicate that this hold time would be sufficient for the 8-layer rings that are going to be used in the next stage of the study.

Table 8: Mean curvature before and after heat treatment

	Layup	# of layers	# of points in fit	Mean curvature (H)		
				Before H.T. (1/mm)	After H. T. (1/mm)	% reduction
1, 1	Symmetric	15	48	6.781×10^{-4}	5.519×10^{-4}	19%
1, 2		15	48	5.216×10^{-4}	4.336×10^{-4}	17%
2	Unidirectional	4	42	3.180×10^{-3}	2.945×10^{-4}	90%
3	Unidirectional	4	42	2.955×10^{-3}	3.108×10^{-4}	89%
4	Unidirectional	12	42	1.100×10^{-3}	1.503×10^{-4}	86%
5	Unidirectional	12	49	1.321×10^{-3}	1.706×10^{-4}	87%

There was no significant difference between the two different heat application methods explored here. The sample in experiment 4 was heated in an oven and experienced an 86% improvement, while the sample from experiment 5 which was heated with a heat blanket experienced an 87% improvement. The heat blanket was only capable of achieving 165°C while the oven reached 200°C, which would support the data from other researchers that there was no significant benefit in exceeding the glass transition of the thermoplastic.

Table 9 shows the variation in z before and after heat treatment, as well as the mean radii of curvature for all the samples. By looking at the values for the mean radius of curvature of the unidirectional samples, the improvement becomes immediately clear. The unidirectional samples had starting radii of 34cm to 90cm, which are noticeably tight curves. After annealing, they had radii of between 321cm to 665cm, which are barely noticeable.

The maximum variation in z will be used to see if the heat treatments were sufficient to meet industry standards. According to ISO 2768-2, the maximum variation should be of 0.8mm [80], while ASTM D5687/D5687M-20 only allows 0.5mm [82]. None of the samples here were able to meet these standards. The smallest variation seen was of 0.850mm, which is still too large

for either standard. Given that the variations ranged from 0.85mm to 1.76mm, a tolerance of 2.00mm would probably be more realistic. A tolerance of 1.50mm could also be realistic, 3 of the 4 unidirectional samples were able to achieve this. This was somewhat expected, given that these standards were designed for machined parts [80] and thermoset polymers [82] respectively, both of which are more dimensionally stable materials.

Layup seemed to make the largest impact on the sample’s curvature reduction. Despite having a 12-hour hold, the symmetric sample saw the little improvement to its mean curvature. Mode 1 improved by 19%, while mode 2 improved by only 17%. It is important to note that this sample did exhibit less initial curvature than the unidirectional samples, which could in part explain the limited % percent reduction in curvature. However, when looking at the maximum deflection noted in Table 9, it is immediately clear that this sample still exhibits the largest deflection of all the samples. It remains further from ‘flat’ than the unidirectional samples. Unlike the unidirectional samples, this angle plies in the asymmetric layup may constrain the movement of the thermoplastic matrix, preventing it from relieving the stresses present.

Table 9: Maximum variation in the z direction after heat treatment and the mean radius of curvature before and after heat treatment

Trial	Layup	# of layers	# of points in fit	Max Δz		Mean radius of curvature (R)	
				Before H.T. (mm)	After H.T. (mm)	Before H.T. (cm)	After H.T. (cm)
1, 1	Symmetric	15	48	8.23	6.71	147.49	181.21
1, 2		15	48	6.05	5.13	191.71	230.62
2	Unidirectional	4	42	13.08	1.76	34.58	339.53
3	Unidirectional	4	42	9.90	1.21	36.01	321.80
4	Unidirectional	12	42	5.11	0.85	90.91	665.18
5	Unidirectional	12	49	11.80	1.48	75.87	586.22



Figure 24: Side view of sample from trial 3 after annealing, 4 layers unidirectional

The major downside of the annealing process is that it tends to leave behind a slight curvature along the fiber direction. Figure 24 shows the sample from trial 3 after the annealing has been performed. This is the same sample as was shown in Figure 20 and Figure 21. Note how after annealing, the sample has a slight curvature in the fiber direction, which wasn’t present originally. All the unidirectional exhibited a similar curvature after annealing. Further work would be required to determine the exact cause of this. However, it seems likely that the interaction between the part and the mandrel would be a major factor. These samples were all

vacuum bagged to flat aluminum tools during annealing. No caul plate was used. As the sample cooled, the side against the tool would cool more slowly than the side against the vacuum bag since the tool would act as a heatsink. This difference in cooling rate could have created a small gradient in the laminate level stresses, which could have caused this visible curvature.

Chapter 4: Annealing of thermoplastic composite rings

4.1 Goal

As previously outlined, the AFP manufacturing process is prone to creating residual process stresses in fabricated parts. The AFP head moves along the part's surface to heat the substrate and deposit more tape. This movement causes non-uniform cooling to occur and residual stresses to arise. In samples with free edges like flat or curved panels, these stresses are immediately apparent as deviations from the intended geometry. In the previous section, it was demonstrated that the residual stresses in unidirectional flat panels can be largely removed using annealing. The goal of this chapter is to see if this procedure can be extended to closed geometries without free edges, like thin rings. The residual stresses in rings are not immediately apparent: they still appear to be perfectly round. These residual stresses can be observed by slitting the ring and observing how it deforms. They may twist, spring inwards, or spring outwards.

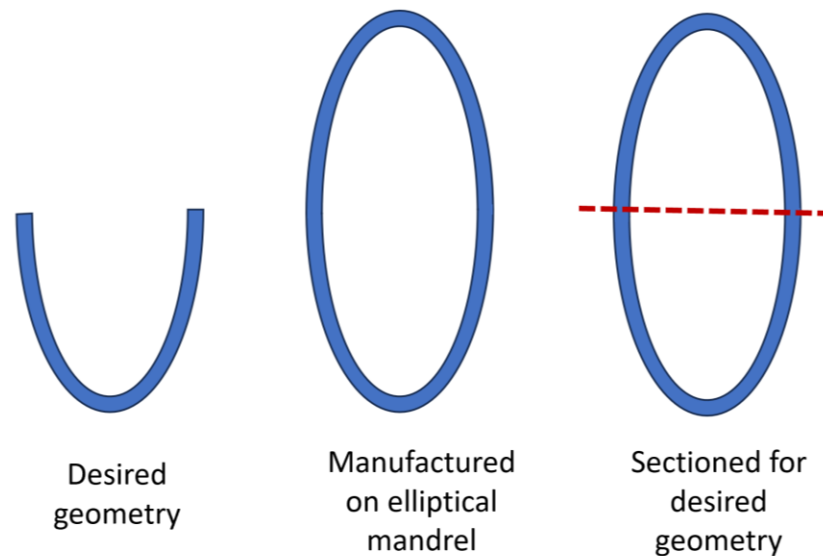


Figure 25: Alternative manufacturing method for tight curves

AFP manufacturing is known for being able to create parts with diverse geometries, but ‘U’ shaped parts can be difficult to achieve because of the springing open that occurs during manufacturing and demolding. Figure 25 presents an alternative method for manufacturing these difficult geometries. The parts could instead be manufactured continuously on closed mandrels, creating parts with no free edges. The deposited composite would then be annealed. The desired arc could then be sectioned away from the rest of the cylinder. The goal would be to produce these “U” shaped pieces without any visible distortion.

Now that the annealing cycle parameters were selected, there were still several steps remaining in this experiment. Three different layup sequences had to be selected for the experiment and processing conditions had to be selected for sample manufacturing. Once the design phase was complete, the tube could be annealed and sectioned into rings. In this final stage of these experiments, the samples needed to be characterized and the residual strains measured. Micrograph analysis and DSC were used to characterize the fiber volume fraction and

the crystallinity respectively. The strain in the samples was measured using strain gages and an external data acquisition system.

4.2 Design of sample layup sequences

The intention was to design 3 layups: a control, a sample that would spring inwards due to the macro-mechanical stresses and a sample that would spring outwards. Properties in the radial and hoop direction were of interest. Transverse properties (along the length of the tube) were not of particular interest for this experiment. The samples needed to be thin enough to be springy, but stiff enough such that the stiffness of the strain gages does not significantly impact the final results. The secondary goal was to have layups that are representative of layups used in the industry and straightforward to manufacture.

Table 10: Sample specifications

# Layers	Layup	Length of tube	Diameter	Intent
8	$[90]_8$	5"	2.5"	Control
8	$[90_4, 45_4]_T$	5"	2.5"	Spring outward
8	$[45_4, 90_4]_T$	5"	2.5"	Spring inward

The final sample layups can be seen in Table 10. Hoop-wound samples (90°) were chosen as the control samples. Hoop winding would make stiff unidirectional samples that would be simple to manufacture. Laying down the tape longitudinally along the mandrel (0°) was not selected because the strength properties of the sample would be largely governed by the tape overlap rather than the properties of the tape itself. 8 layers was selected as the thickness. These samples were manufactured on a 2.5" diameter steel mandrel.

It would be possible to achieve the goal of designing one layup that springs in and one that springs out by inducing two equal and opposite bending moments within the laminates. The bending moment would force a curve in the samples, causing one of the rings to spring inward while the other sprung outwards. It is well understood that a bending moment is generated when two materials with different coefficients of thermal expansion are bonded to one another [92]. While the system of equations by Timoshenko [92] is commonly used when considering metals with different coefficients of thermal expansion [92], this same principle can be applied to composite laminates [24], [93], [94]. Instead of using 2 different metals, 2 laminae of different orientations are considered. The difference in the coefficient of thermal expansion in each direction, combined with the difference in angle between the 2 laminae can create the same effect as the sample cools down from the processing temperature [24], [93], [94].

Asymmetric layups consisting of four 45° plies and four 90° plies was selected. These 2 layup sequences can be shortened to $[90_4, 45_4]_T$ and $[45_4, 90_4]_T$. Note that the plies are listed in the order they are laid down, with the first plies being against the mandrel. Transverse plies (0°) were also not used in these asymmetric layups for the reasons stated previously.

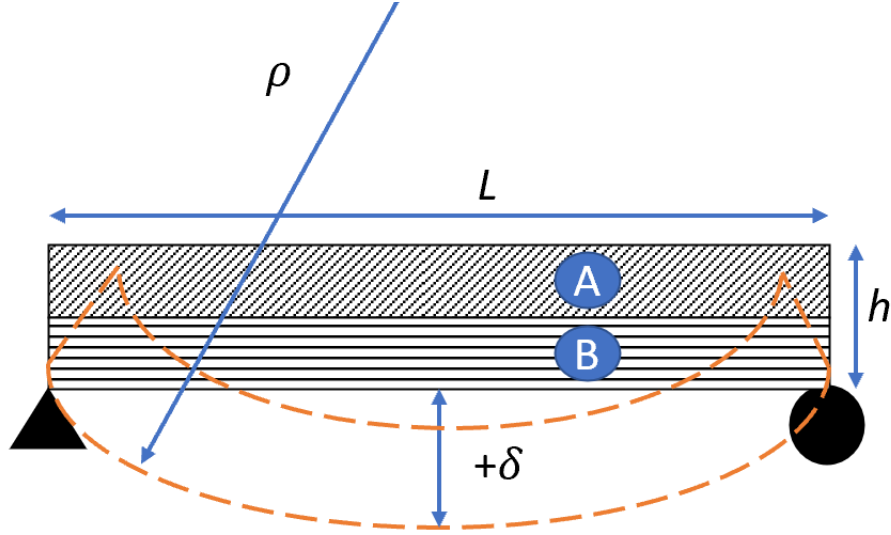


Figure 26: Coordinate system used for bimetallic strip approximation

To attempt to predict which of the asymmetric layups will spring in and which would spring out, a simple approximation was done using Timoshenko's bimetallic strip analysis [92]. While these equations are built for flat geometries, they were simply used to indicate in which direction the sample would curve: towards the 45° plies or the 90° plies. The direction and not the magnitude of the deflection is what was important at this stage. The geometry used in this approximation can be seen in Figure 26. In the following equations, the subscript 'A' refers to the top 4 layers (45°), while the subscript 'B' refers to the bottom 4 layers (90°). The off axis-properties of these plies were used. This would help to isolate how these layers would interact, highlighting the macro-mechanical stresses. The properties of laminate 'A' were taken to be the off-axis properties in the x direction at 45°. The properties of laminate 'B' were taken to be the properties of carbon fiber in the fiber direction. The average longitudinal properties and their respective sources for the strip arrangement seen in Figure 26 can be seen in Table 11.

Table 11: Average ply properties for the arrangement shown in Figure 26

	Ply Orientation	Off-Axis Properties	
A	45°	$E_A = 12.57 \text{ GPa}$	[77], [95]
		$\alpha_A = 1.19 \times 10^{-5} \text{ 1/C}$	[96]
B	90°	$E_B = 138 \text{ GPa}$	[77], [95]
		$\alpha_B = -0.2 \times 10^{-6} \text{ 1/C}$	[96]

Assuming that the two layers seen in Figure 26 were the same thickness and have a combined thickness of h , the curvature of a sample for any given temperature range ΔT can be calculated from the samples' young modulus (E_A, E_B) and their coefficients of thermal expansion (α_A, α_B) [92]. The temperature range used here was $\Delta T = 20 - 200^\circ\text{C}$, to simulate the sample cooling from an annealing temperature of 200°C to a room temperature of 20°C .

$$n = \frac{E_A}{E_B} \quad (12)$$

$$\frac{1}{\rho} = \frac{24(\alpha_B - \alpha_A)\Delta T}{h\left(14 + n + \frac{1}{n}\right)} \quad (13)$$

The radius of curvature (ρ) and the length of the sample (L) can be used to calculate the deflection (δ) of the sample [92]. The sign of the deflection (δ) will indicate whether the laminate would curve towards the 45° plies or the 90° plies. As an approximation, the length of the samples was taken to be the circumference of the hoops. Note that this behavior isn't visible in the fully constrained ring, it can only be observed in a slit ring. At this stage, approximating the slit ring as a flat strip is enough to get an indication of in which direction the deformation will take place.

$$\delta = \frac{L^2}{8\rho} \quad (14)$$

Table 12: Curvature and deflection results for the arrangement shown in Figure 26

Curvature	1.63 1/m
Radius of curvature	0.614 m
Deflection	0.00810 m

The results for the curvature, radius of curvature, and deflection for the arrangement shown in Figure 26 can be seen in Table 12. Notice that the deflection is positive, predicting that the ply would curve into a ‘smile’ shape, putting the 45° ply in compression and the 90° ply in tension. The opposite would be true if the laminate was constructed in the opposite direction.

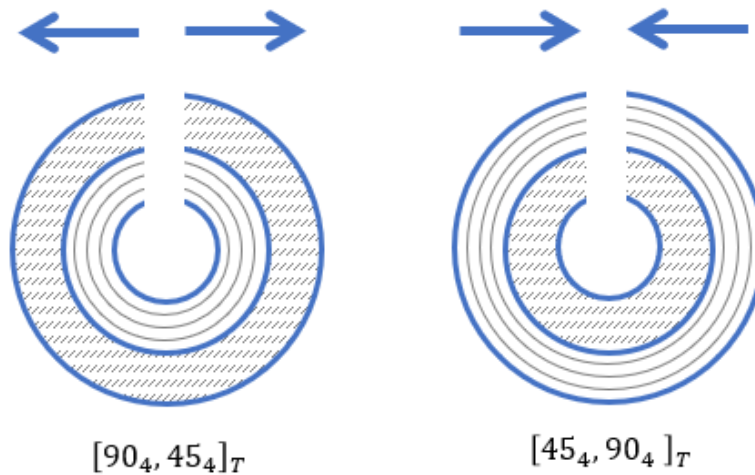


Figure 27: Expected spring in and spring out behavior

Using this approximation, it is possible to predict the spring in and spring out behavior of those laminates. Given that the $[90_4, 45_4]_T$ laminate has the 45° plies as the outer layers, spring out behavior would put the 45° ply in compression and the 90° ply in tension. The opposite

residual stress profile would develop in the $[45_4, 90_4]_T$ layup, in which would cause the ring to open. This is illustrated graphically in Figure 27. These predictions will later be validated experimentally. It will also be possible to determine whether annealing would relieve or accentuate this behavior.

4.3 Sample manufacturing

The samples were manufactured on a 6-axis automated fiber placement system made by Automated Dynamics which can be seen in Figure 28. The robotic arm is the model ZX130L, made by Kawasaki [97]. This AFP uses a hot gas torch to heat the incoming tape during manufacturing. This AFP has 2 interchangeable heads, one designed for thermoplastic manufacturing, and another for thermoset manufacturing. The entire AFP assembly used to manufacture the samples for this experiment can be seen in the image below.

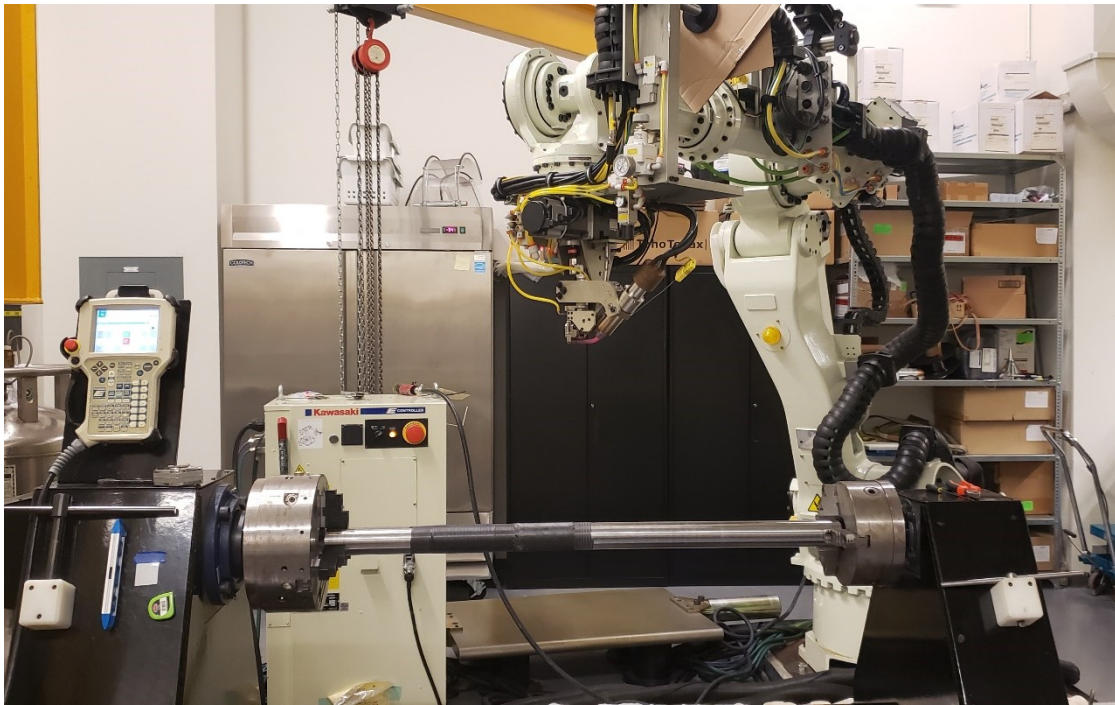


Figure 28: AFP manufacturing of experimental samples

4.3.1 Processing conditions

The three different layup sequences manufactured for this experiment can be seen in Table 10. To speed up manufacturing, reduce waste, and ensure dimensional accuracy, the samples were all manufactured as one continuous tube. Excess length was added between each section to allow for cutting. A 2.5” diameter mandrel was used. To help with the adhesion, an initial hoop-wound layer was placed on the mandrel. On that section, both the $[90]_8$ and $[90_4, 45_4]_T$ layups were built. The hoop-wound or $[90]_8$ sample were laid down at 88° to allow for the head of the AFP to translate during deposition. Five (5) inches away from the edge of the hoop-wound section, a small band of hoop-wound tape was laid down. Using this additional band and the original hoop-wound layer as anchors, the $[45_4, 90_4]_T$ sample was built. Without these anchors, the 45° bands would have nothing to adhere to. Each 45° layer was comprised of 19 bands. The parts after manufacturing can be seen in Figure 29. Five inches of length was manufactured for each sample.

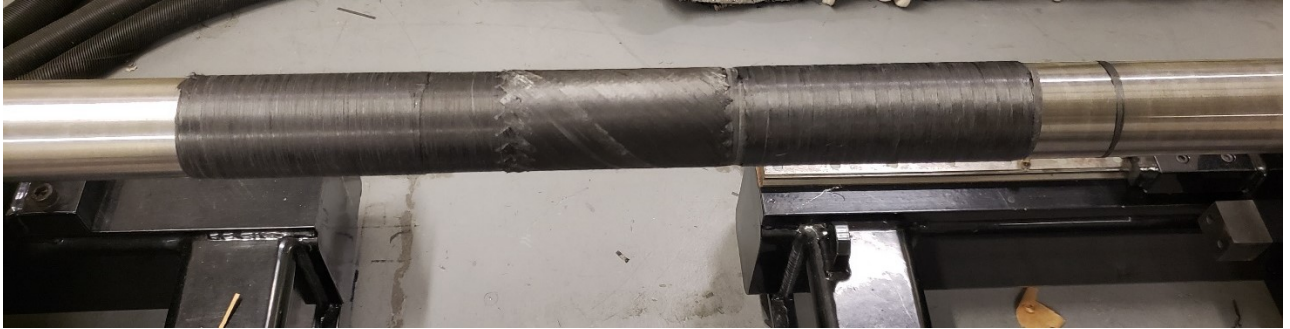


Figure 29: Manufactured samples cooling on mandrel after deposition

During the layup, the gas flow through the torch was 60 standard liters per minute, and the temperature of the torch was at 875°C. The roller had a diameter of 0.5” and applied a compaction force of 60lb. The layup speed was of 2.5”/s. All of these process parameters were used at the recommendation of the operator. An overview of the process parameters can be seen in Figure 30.

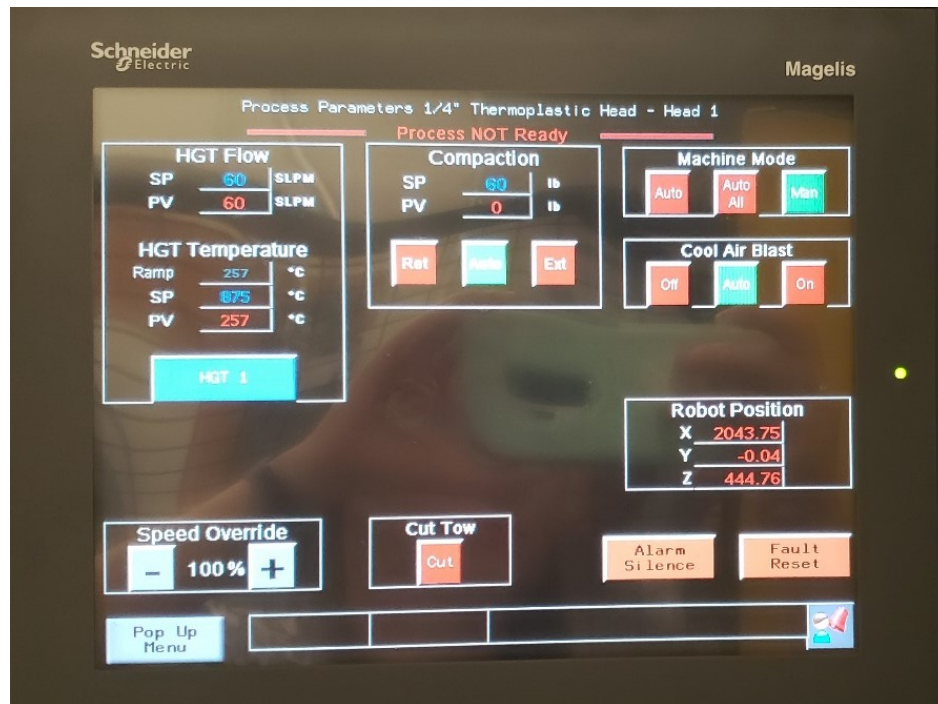


Figure 30: Readout of manufacturing parameters

4.3.2 Material specifications

All of the samples were made using carbon fiber (AS4) reinforced PEEK (APC-2) pre-impregnated tape manufactured by Solvay [95], [77]. The thermal properties provided by the supplier [77] for the APC-2 PEEK thermoplastic matrix can be seen in Table 13. The mechanical properties of the APC-2/AS4 prepreg tape according to the supplies can be seen in Table 14.

Table 13: Thermal properties of APC-2 PEEK matrix according to manufacturer [77]

Glass transition temperature	143°C
Processing temperature	385-400°C

Table 14: APC-2/AS4 tape properties from manufacturer at 24°C [77], [95]

Wt% of resin	34%
0° Young's modulus	138 GPa
0° Poisson's ratio	0.30
90° Young's modulus	10.3 GPa
Shear modulus	5.7 GPa

4.4 Ring annealing

The previous experimentation on flat samples was used to finalize the annealing cycles for the thermoplastic rings. A summary of these parameters can be seen in Table 15. The oven was selected as the heat application method instead of the heat blanket because the oven offered superior temperature control and consistency. It did not require additional insulation like the heat blanket did. Additionally, the heat blanket could not have uniform contact with the rings due to their geometry.

Table 15: Final annealing cycle parameters for thermoplastic composite rings

Method of heat application	Oven
Annealing temperature	200°C
Vacuum bag pressure	None
Hold time	3h
Heating rate	7.6°C/min
Cooling rate	0.5-2.25°C/min

The annealing temperature of 200°C and hold time of 3h were sufficient for the unidirectional samples and so they were retained. Although the temperature could have been reduced to a value closer to the glass transition temperature of PEEK, 200°C was retained as a safe bet. Unlike the flat samples, rings are a self-constrained geometry with no free edges. For this reason, vacuum bagging was deemed unnecessary. Finally, the default rapid heating and slow cooling at approximately 2°C/min was retained.

4.5 Sample dimensioning and cutting

The tube seen previously in the manufacturing section (Figure 29) shows all 3 layups wound consecutively. To begin, this tube was sectioned twice to isolate the three layups from one another. Each layup was approximately 5" long at this stage. Note that all of the cutting mentioned in this section was done on a tile cutting saw with a diamond saw blade. Then, each tube was cut into 2 equal halves of 2.5". One of the halves was put aside to be the unannealed in-situ consolidated sample. The other half was annealed in a convection oven using the annealing cycle outlined in Table 15. Samples in the convection oven can be seen in Figure 31.

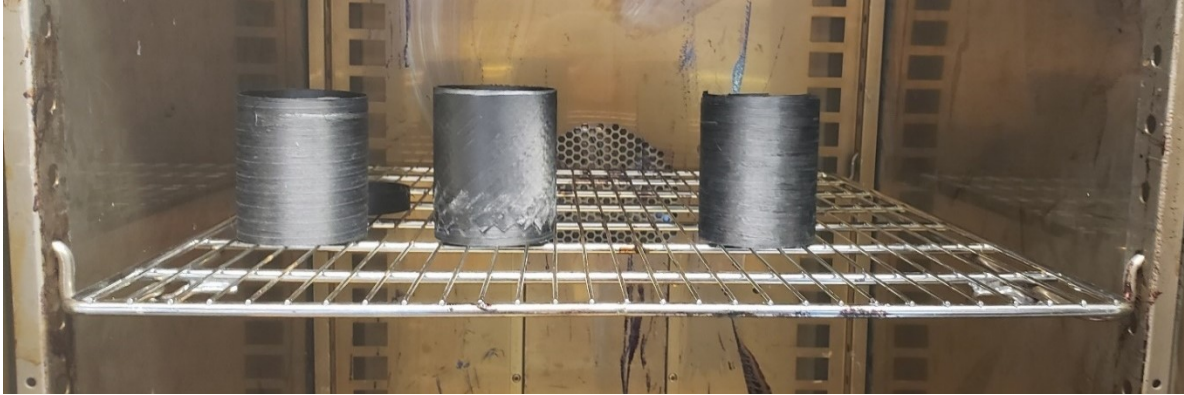


Figure 31: $[90]_8$, $[90_4, 45_4]_T$ and $[45_4, 90_4]_T$ samples in convection oven for annealing

The three different layups ($[90]_8$, $[90_4, 45_4]_T$, $[45_4, 90_4]_T$) and the two different heat treatments (annealed and in-situ consolidation) create 6 unique sample combinations. Each of those 6 samples was then cut into 3 rings that are 0.25” wide. The rough edges of the tube were cut off and discarded. This made for a total of 18 composite rings.

To ensure that the samples were safely cut to an even thickness, a 2-part cutting jig was 3D printed. The jig can be seen in Figure 32. The piece on the right was a grip. The tube to be cut was held in the grip with the small set screw. It simply made the tube longer and therefore easier and safer to hold during the cutting process. The piece on the left in Figure 32 is the cutting guide. This guide has 2 recessed surfaces to ensure uniform sample thickness. It also served to provide support to that free edge during cutting. Since the rings were being cut to a thickness of 0.25”, it would not have been safe to hold them during the cutting procedure.

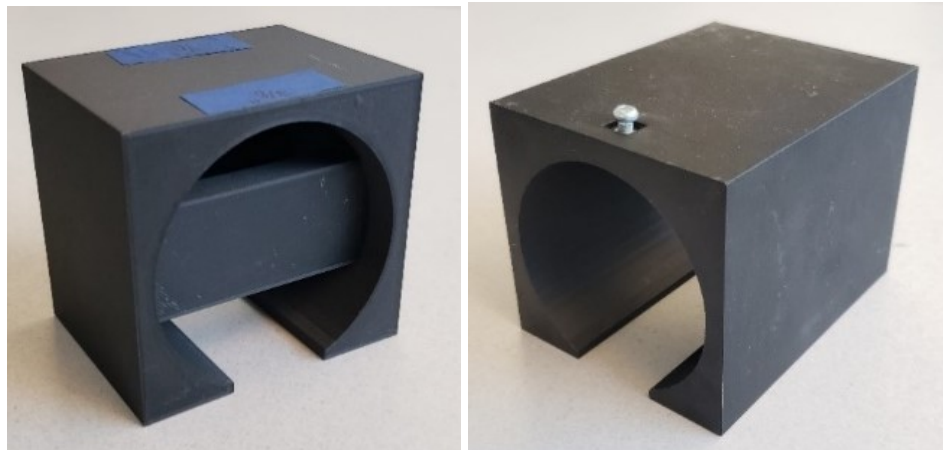


Figure 32: 2-part cutting jig oblique view, the grip (right) and cutting guide (left)

4.6 Experimental procedure

4.6.1 Strain gages

After careful consideration of the data collection methods presented in the introduction, strain gages were selected for their ease of installation and given that they were readily available. They are a mature and reliable technology that could provide repeatable results. They were also in-stock with local suppliers. Non-destructive testing and the additional complexities associated with these techniques were deemed unnecessary because samples were going to be manufactured

specifically for this experiment. Given that cylindrical geometry was the focus of this experiment, slitting the rings [13], [27] was deemed the easiest way to observe the residual stresses. The strain gages would be installed to the individual rings after annealing was performed, but before they were slit.

Table 16: Manufacturer data for strain gages

		Linear gages	Rectangular Rosette	Stacked Rosette
Manufacturer		Micro-Measurements	Micro-Measurements	Micro-Measurements
Part number		C4A-06-235SL-350-39P	C5K-06-S5198-350-33F	C2A-06-031WW-120
Item code		MMF404146	MMF402103	MMF315450
Lot number		A106AD1039-671520	K104BD1016-709290	A86AD850
Resistance		350.0 Ω \pm 0.3%	350.0 Ω \pm 0.5%	120.0 Ω \pm 0.6%
Gage factor	Grid 1	2.09	1.86	2.175 \pm 0.5%
	Grid 2		1.79	
	Grid 3		1.86	
Transverse sensitivity	Grid 1	+0.5 \pm 0.2%	+1.9 \pm 0.2%	+1.8 \pm 0.2%
	Grid 2		+3.6 \pm 0.2%	
	Grid 3		+1.9 \pm 0.2%	
Application		Unidirectional hoop-wound samples	Asymmetric $[90_4, 45_4]_T$ and $[45_4, 90_4]_T$ samples	Substitution on unannealed $[45_4, 90_4]_T$ sample

A combination of linear strain gages and rectangular rosettes were used to collect data in this experiment. All of the gages were manufactured by Micro-Measurements and their manufacturing data can be seen in Table 16. The linear gages in the first column of Table 16 were placed on the inside and outside surfaces of the 6 unidirectional hoop-wound samples. The rectangular rosettes in the middle column of Table 16 were placed on the inner and outer surfaces of the asymmetric laminates. One of the rectangular rosettes broke during installation and had to be replaced by the stacked rosette seen in the final column of Table 16. This substitution was not ideal given that the rectangular and stacked rosettes had a different resistance and gage factors, but the substitution was necessary because of the lead time for re-ordering a set of the rectangular rosettes.

A pair of linear gages installed on the inner and outer surfaces of a unidirectional sample can be seen in Figure 33. The rectangular rosette installed on all the asymmetric samples can be seen in Figure 34. The grids on the rosettes are numbered from one to three (from left to right) and were always plugged into the data collection system in this order to ensure consistency. Note that in Figure 34, the circumferential strain is measured by grid one on the outer surface and grid three on the inner surface. This orientation was tracked carefully to ensure accurate results.

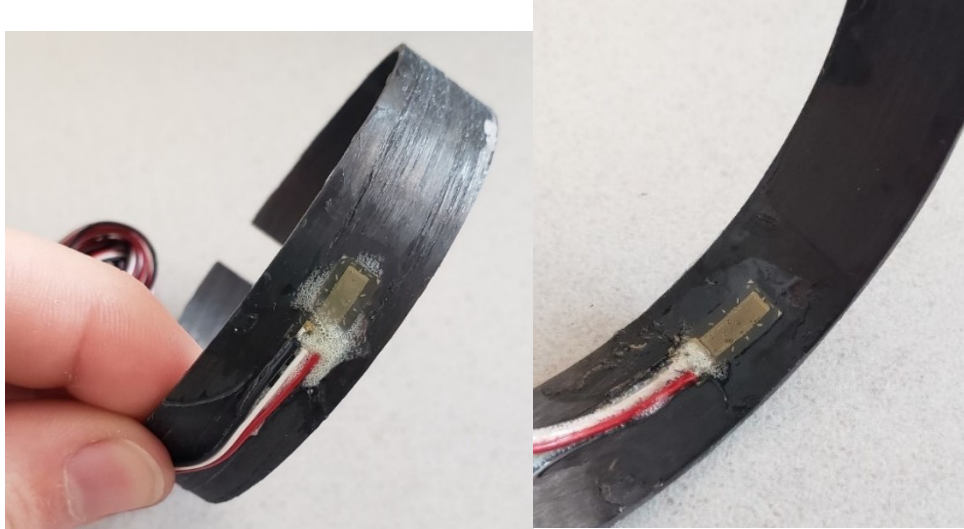


Figure 33: Linear strain gage installed on outer surface (left) and inner surface (right) of annealed unidirectional hoop-wound sample

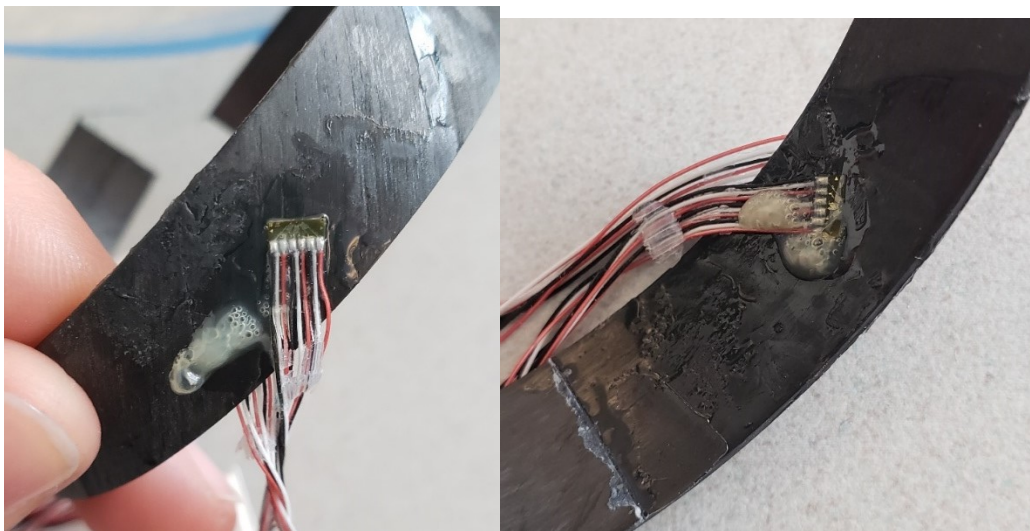


Figure 34: Rectangular rosettes installed on outer surface (left) and inner surface (right) of not annealed $[90_4, 45_4]_T$ sample

4.6.2 Strain gage installation

The strain gage installation process involved 3 overall steps: surface preparation, gage installation, and weatherproofing. The surface preparation insures a clean and smooth surface for the gage installation. The installation involves adhering and aligning the gages with the samples. The diamond saw used to cut the samples is water cooled, so weatherproofing was necessary to prevent a short circuit while measurements were taken. Main tool used for the installation can be seen in Figure 35 and are listed in Table 17.

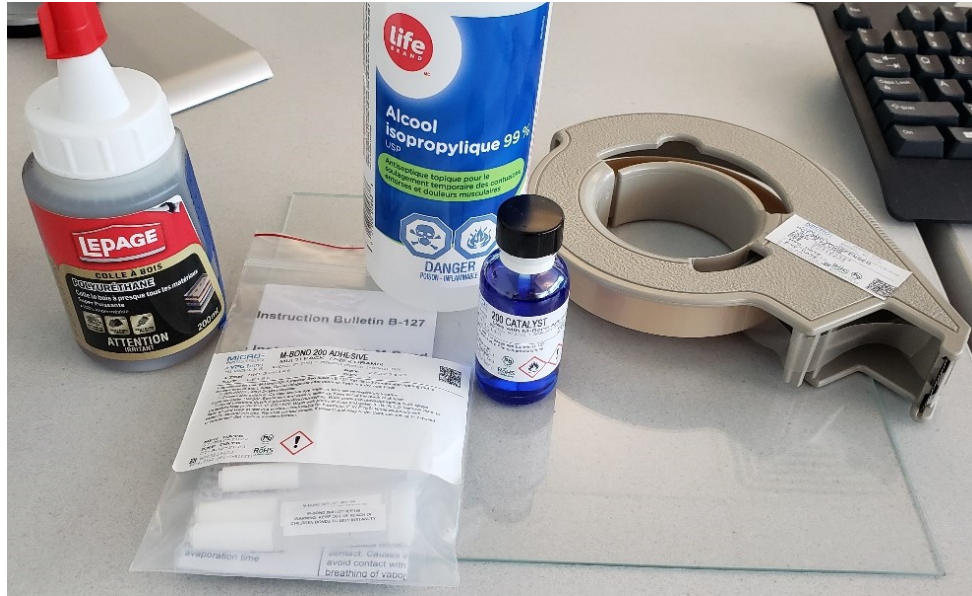


Figure 35: Strain gage installation material including waterproof coating, M-Bond 200 adhesive and catalyst, 99% isopropyl alcohol, PCT installation tape and glass sheet

Table 17: Breakdown of tools used for strain gage application

Surface Preparation	Gage Installation	Weatherproofing
180grit sandpaper 320grit sandpaper 99% isopropyl alcohol	M-Bond 200 adhesive [98] M-Bond 200 catalyst PCT transfer tape Sheet of glass	LePage polyurethane glue

For the surface preparation, the gage installation sites were initially sanded with 180grit sandpaper, then 320grit sandpaper to refine and equalize the texture. To remove the sanding dust, the sanded surfaces were scrubbed with a disposable dust-free cloth and 99% isopropyl alcohol, which is considered an adequate degreaser for carbon fiber composites [99]. The surface was then wiped down 3-5 more times in a single direction with a clean cloth and more 99% isopropyl alcohol [100].

For testing at room temperature, M-Bond 200 is the recommended adhesive [98]. To begin the installation, the strain gages are picked up from a sheet of glass using a 2” strip of transfer tape called PCT tape [100]. To lift the gage, the tape was lifted off the glass at a 45° angle [100], as seen in Figure 36.



Figure 36: Rectangular rosette being lifted from glass sheet at a 45° angle

The gages must now be aligned with the fibers in the sample. A diagram of the intended gage alignment for each layup can be seen in Figure 37. Note that the sizes of the gages are exaggerated for ease of viewing. The strain gages were installed using a headband magnifier for more precision and placed using the direction of the fibers as a guide, instead of the edge of the sample. Although the hoop-wound samples have been referred to as 90° laminae, they are laid down at 88° to allow for the head to translate across the mandrel. The rosettes are aligned such that the first, second and third gages are aligned with the hoop, shear, and transverse directions respectively.

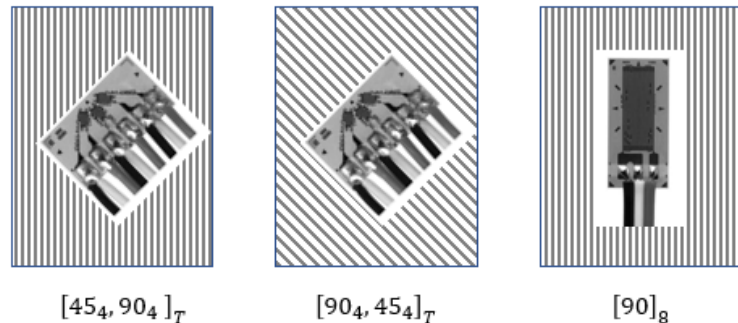


Figure 37: Strain gage alignment on the outer surface of different layups, diagram not to scale [101], [102]

The gage can then be transferred to the sample using the PCT tape and carefully aligned with the fibers. If the alignment is off, the gage can be lifted from the sample by pulling up the tape at 45° and its position can then be adjusted. The excess tape was trimmed such that a 0.25” flap was left past the gage. This tab was then folded over the edge of the sample to act as a small hinge. This assembly can be seen in Figure 38 (left). Once the alignment is good and the flap is secured, the gage is lifted at 45° and folded as shown in Figure 38 (right).

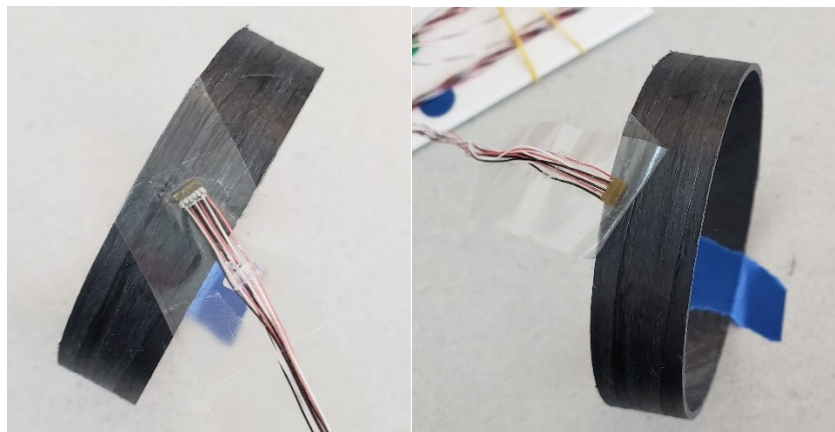


Figure 38: Alignment of rectangular rosette on a 90° outer ply (left) and rectangular rosette pulled back to allow the glue application (right)

The gage is then coated in a very thin layer of catalyst. After a one-minute drying period, a single drop of glue was placed at the folded edge of the tape. Then, the tape was brought to a 30° with the sample [100] and a piece of the dust-free cloth was used to “squeegee” the glue across the gage. Finger pressure was then applied to the gage. Manufacturers recommend at least 1 minute [100]. For gages applied to the inner radii of the rings, 2 minutes of thumb pressure was

used. For gages applied to the outside of the sample, 4 minutes was found to work best. This difference in time is because the strain gages are slightly concave and did not make good contact with the outer radius and the extra time is needed to avoid the gage lifting. After the pressure has been applied, the tape was left on for at least 2 more minutes and removed by pulling it back over itself [100].

In order to prevent the cooling water from the tile cutting saw from creating a short circuit in the strain gages, the gages were all coated in a thin layer of waterproof polyurethane glue. Toothpicks were used to apply the glue to the rectangular rosettes due to their small size. The polyurethane glue was left to cure for 24h [103].

The strain gages must be connected to the data acquisition system through 8-pin RJ45 connectors [104]. The linear gages were pre-cabled with the correct gage of wire for RJ45 connectors. The rectangular rosettes came pre-cabled with thin wires that could not be crimped directly into RJ45 connectors. A 6" piece of cable was soldered into every rectangular rosette to act as an intermediary.

4.6.3 Data collection system

Strain data was collected using Micro-Measurements' System 8000-8-SM, which can be seen in Figure 39. This data collection system connects to an external computer via an ethernet cable. This system is compact, easy to transport, and supports up to 8 channels. The System 8000 is controlled from the computer using StrainSmart 8000 V1.5.4 software. This software allows users to connect gages, specify their gage factor, zero the gages, collect data and export the data in several file formats [105]. The strain was recorded as a function of time. This meant that data before, during and after the cut was recorded. The System 8000 has a resolution of 0.5 microstrain [106], which was deemed to be sufficient for this application since the strain recorded was generally in the order of magnitude of several hundred microstrain.

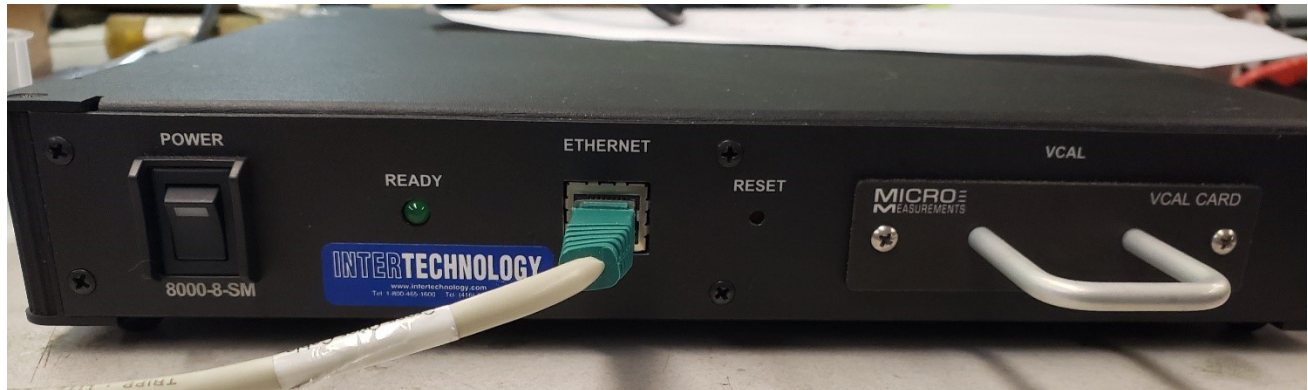


Figure 39: System 8000-8-SM for data collection

4.6.4 Radius

In addition to the strain measurements, the change in a sample's radius can be used to quantify the samples' deformation. The outer radius of each sample was measured using an image analysis software called Digimizer. The samples were labeled, and images of each sample were taken before and after cutting. Each photograph was labeled and taken with a ruler to provide scale. The radius was measured using the arc measurement tool [107].

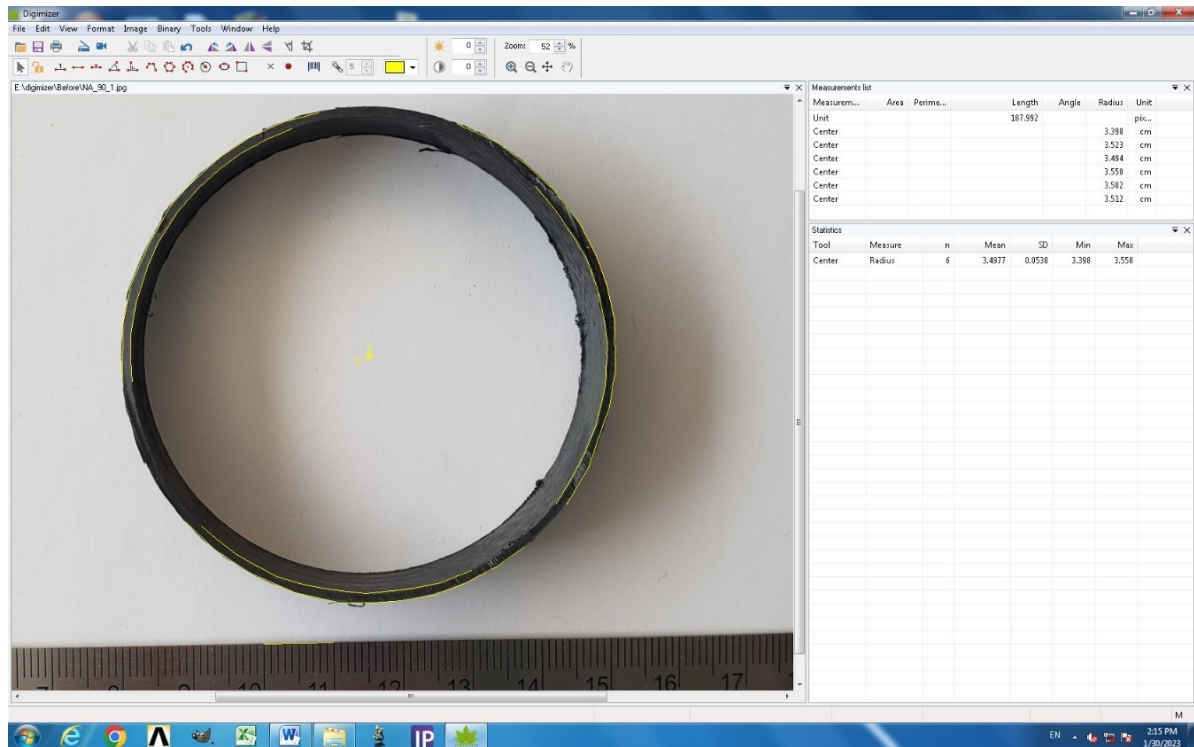


Figure 40: Inner and outer radius measured using the arc measurement tool[107]

When using the arc measurement tool, users click points along their arc. The software uses these points to estimate where the center of the arc lies [107]. Best results were obtained by measuring 3 arcs, each representing over a third of the circle each. Each arc contained between 6 and 8 points. Using smaller arcs created variation in the radius measurement. Giving preference to larger arcs mitigated this problem. An example of how the measurements were taken can be seen in Figure 40. Only measurements for the outer radii were reported because higher contrast between the outer edge and the white background made it easier to distinguish the points. The inner radius was harder to distinguish reliably from the inner surface of the samples and so they were not recorded for this experiment.

4.7 Data collection for sample characterization

Data collection was necessary to characterize the samples, and to perform the experiment. To characterize the samples, a micrograph analysis was performed to determine the fiber volume fraction and the void content of samples. Additionally, the crystallinity before and after annealing was measured using differential scanning calorimetry (DSC).

4.7.1 Micrograph analysis

All of the images were captured with a Fein Optic optical microscope. A ProgRes SpeedXT Core 5 camera from Jenoptik is used to interface between the microscope and a desktop computer. ProgRes CapturePro 2.10.0.1 software is used to record the images. All of the subsequent image analysis was performed in ImageJ. In order to assess the quality of the laminate, fiber volume fraction and void content were measured.

4.7.1.1 Sample preparation

The composite samples must first be affixed in a resin puck and then highly polished before imaging. Samples were first cut into pieces roughly 1 cm long by 1 cm wide. The samples were then placed in blue spacers that can be seen in Figure 41. The spacers were then placed in red molds, also visible in Figure 41. The bottom of the mold was sealed with Teflon tape. The molds were then filled with a mixture of D.E.R. 324 epoxy (233-R) and 11% of D.E.H 24 hardener (233-H) from Anamet Canada. The epoxy was left to cure for 24h at room temperature and removed from their molds. They were then post-cured at 100°C for 1 hour.

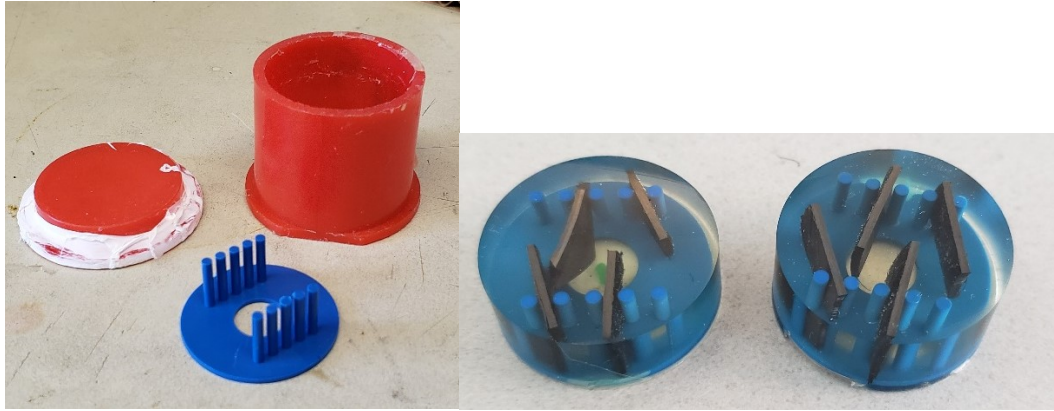


Figure 41: Mold and sample holder (left), polished puck (right)

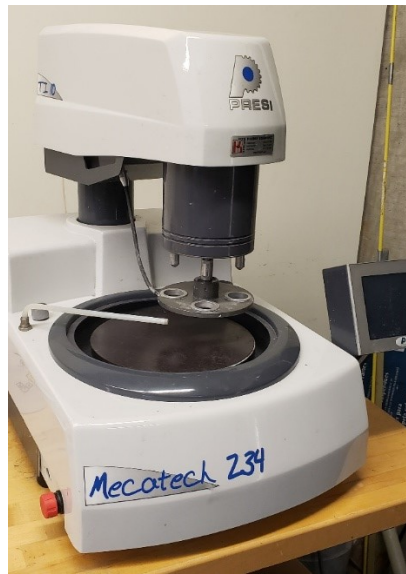


Figure 42: PRESI - MECATECH 234 polishing machine

Once they were fully cured and had cooled, the samples were polished using the MECATECH 234 manufactured by PRESI, which can be seen in Figure 42. The exact procedure used for sanding and polishing the samples can be seen in Table 18. An example of pucks that are fully polished can be seen in the right of Figure 41. The samples are now ready for imaging.

Table 18: Polishing procedure

	Sanding			Polishing	
Grit	P180 sandpaper	P320 sandpaper	P600 sandpaper	9 μ polishing pad sprayed with 9 μ suspension and lubricant	3 μ polishing pad sprayed with 3 μ suspension and lubricant
Lubricant	Water	Water	Water	Lubricant	Lubricant
Lubricant flow	Constant	Constant	Constant	2.5mL every 20s	2.5mL every 20s
Cycle time	120s	120s	120s	120s	120s
RPM of base	300-400 RPM	400 RPM	400 RPM	500 RPM	500 RPM
RPM of head	100 RPM	100 RPM	100 RPM	125 RPM	150 RPM
Force	3N	3N	2N	1N	1N
Note	Repeat rough sanding until the composite is exposed to the puck's surface		At end of sanding, wash samples with water to not contaminate polishing pads	Repeat polishing a second time, rinse with water	Repeat polishing a second time

4.7.1.2 Fiber volume fraction

The image analysis was performed in ImageJ using an image analysis procedure by Conklin [108]. The goal of this procedure is to transform the colour images taken with the microscope into black and white binary images to highlight the fibers. At the end of the analysis, the fibers should be visible as white dots on a solid black background. The fibers should remain round and distinct from another. Touching fibers should not merge. Conklin's [108] procedure was slightly modified to yield better results. Images at 20 times and 10 times magnification were used for analyzing the tapes and laminates respectively. At 20 times magnification, it was not possible for the entire laminate to be in the shot. The step-by-step used to analyse the images can be seen below.

1. Image > Type > 8 bit
2. Image > Adjust > Threshold
3. Process > Smooth
4. Process > Binary > Make Binary, check 3 boxes
5. Process > Binary > Open
6. Process > Binary > Watershed
7. Select the region
8. Analyze > Analyze particles

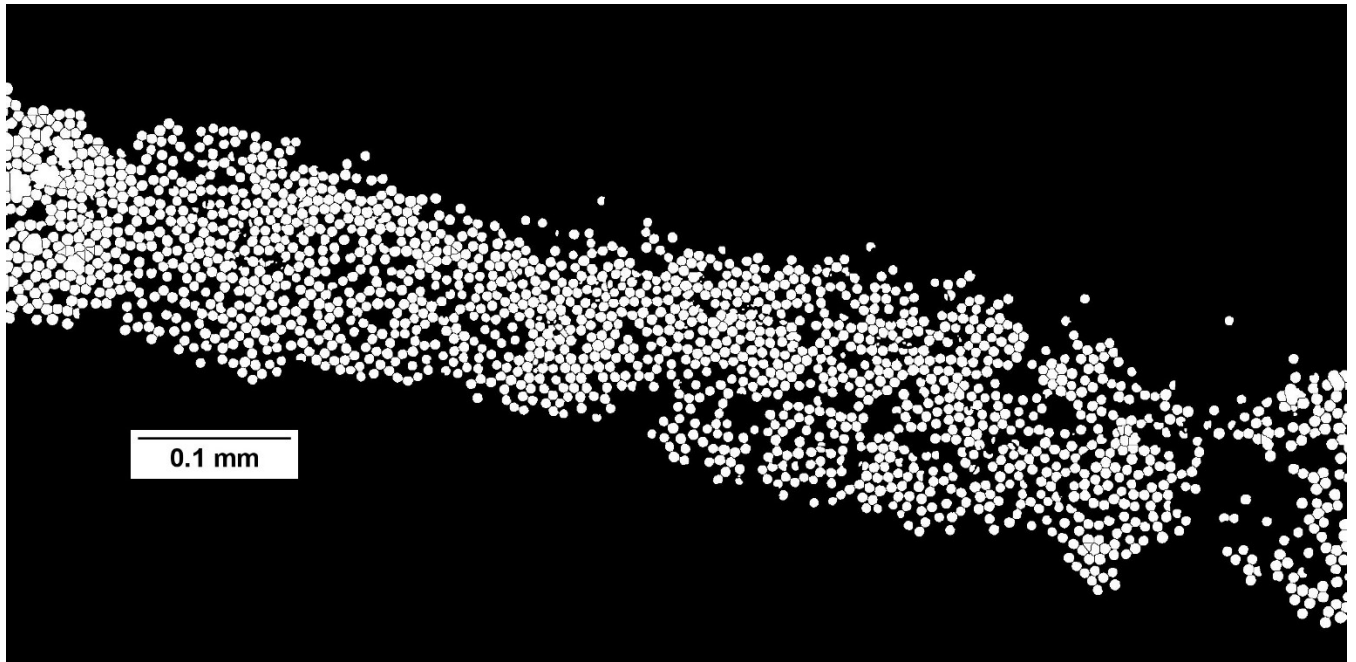


Figure 43: Image of thermoplastic tape (20X magnification) transformed using adapted procedure

The final result for the adjusted procedure can be seen in Figure 43. Note that the fibers are all round and distinct from one another. There is only clumping towards the edge of the image. This edge distortion is unavoidable because the depth of focus is very shallow with this microscope, and the center of the image is more sharply in focus.

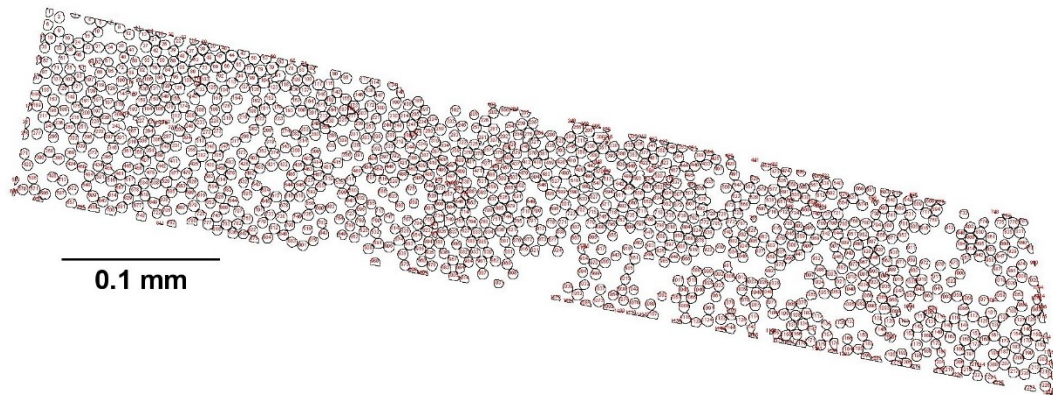


Figure 44: Number of fibers and their respective surface area being calculated in ImageJ for thermoplastic tape at 20X magnification

Once the transformation to a black and white binary image is complete, a representative area of the sample must be selected. A built-in analysis tool in ImageJ called “Analyze particles” can then be used to calculate the number of fibers in the image and the percentage of the cross-sectional area they represent. A sample from that analysis can be seen in Figure 44. Each fiber is

circled and numbered. These analysis results were always consulted to make sure that the analysis tool was calculating the area of the fibers, rather than the matrix area.

4.7.1.3 Void content

The void content of these samples was measured using a procedure adapted from Conklin [108] and Morales et al. [109]. Conklin's [108] procedure was used to transform the image into a black and white binary image. Morales et al. [109] was used as a guide for selecting the correct threshold for selecting the voids. Note that it is very important that the images contain no scratches leftover from the polishing process. These scratches are similar in colour and saturation to the voids and would be picked up along with the voids. Like with the fiber volume fraction analysis, the tape was analyzed using images at 20 times magnification, while the laminates were analyzed using images at 10 times magnification.

In the previous section on fiber volume analysis, the images were cropped after the image was transformed into a black and white binary image. This was possible because the fibers were clearly visible and it was easy to deduce the boundary between the sample and the epoxy puck. However, for the void content analysis, the samples must be cropped first. With only the voids visible as black specks on a white background, it was impossible to deduce the boundary between the sample and the epoxy puck.

1. Image > Crop
2. Save as a new file
3. Image > Type > 8 bit
4. Image > Adjust > Threshold to achieve selection in Figure 45
5. Process > Smooth
6. Process > Binary > Make Binary, check all 3 boxes
7. Analyze > Analyze particles

The procedure used to calculate the void content of the samples can be seen above. What is key in this procedure is selecting the correct threshold value. An example is shown in Figure 45. While the exact numerical value may vary from image to image, it is important that only the darkest intensity pixels be selected [109]. This means that the threshold selection should end before the image's peak.

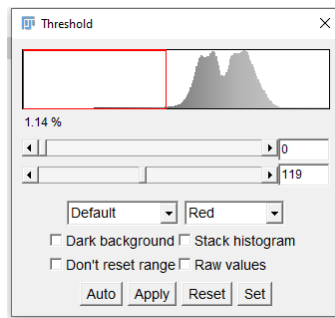


Figure 45: Threshold necessary for void analysis

Some crucial steps in the image analysis procedure can be seen in Figure 46, Figure 47, and Figure 48. All of these images are at 10 times magnification. Figure 46 shows a cropped version of a larger micrograph to isolate a representative portion of the layup. Figure 47 shows the image after the threshold has been applied and the image is converted to binary. Only the

voids are still visible. Figure 48 shows the result of the ‘Analyze particles’ function in ImageJ where all the particles are counted, and their surface area calculated.

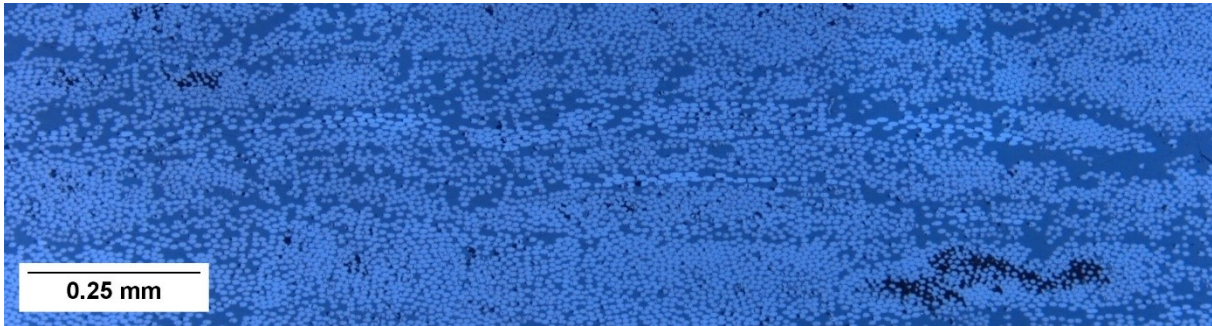


Figure 46: Annealed [45₄, 90₄]_T sample cropped to retain a representative portion of the 45° layers at 20X magnification

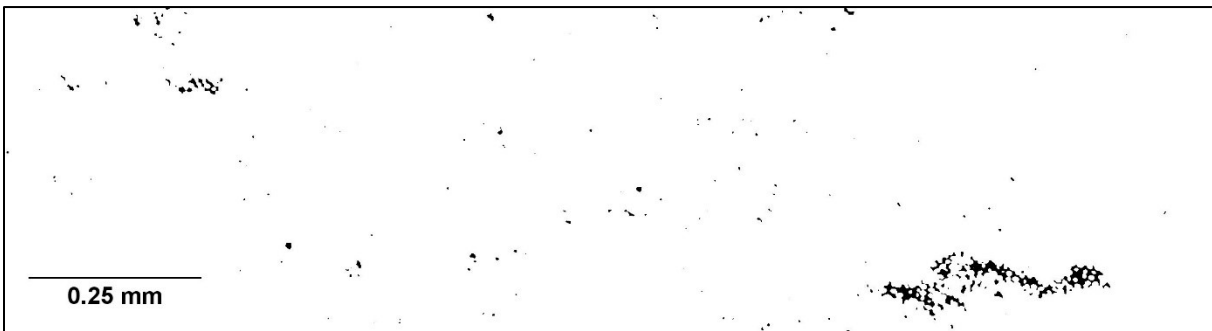


Figure 47: Annealed [45₄, 90₄]_T sample with the threshold adjusted to select only for the voids 20X magnification

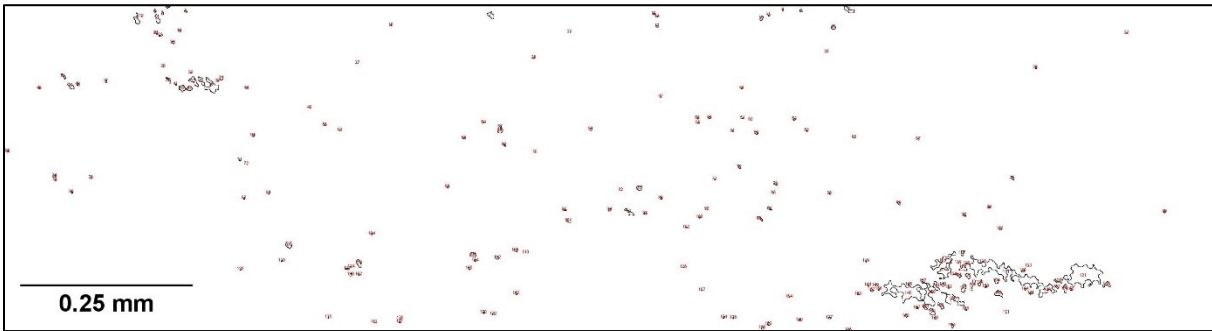


Figure 48: Annealed [45₄, 90₄]_T sample with voids counted using 'Analyze Particles' function 20X magnification

4.7.2 Crystallinity

DSC Q200 and Refrigerated Cooling System (RCS) 90 from TA instruments were used to characterize the thermal properties of these samples. The goal of the DSC analysis was to determine the crystallinity of the samples before and after annealing. The crystallinity of the samples could be impacted by the annealing process. Crystallinity was also commonly measured in other annealing experiments [52], [53], [56], [58], [60], [74]. The testing procedure selected for this analysis can be seen in Table 19. Each different layup was processed three times to help normalize the data. The crystallinity of the carbon fiber reinforced thermoplastic tape from the supplier was also measured three times to serve as a reference.

Table 19: Testing procedure for DSC

Pan type	Aluminum hermetic
Sample weight	10-13 mg
Testing procedure	Heat/Cool/Heat
Starting temperature	0°C
Heating rate	10°C/min
Upper temperature	380°C
Cooling rate	10°C/min
Lower temperature	0°C

Aluminum hermetic pans were selected because they can hold larger samples. Given that less than half of the composite material was made of the matrix, it was important that there be enough thermoplastic to get repeatable DSC results. At the highest temperature, it is important that the sample be fully melted. The upper temperature of 380°C was selected because it is nearing the processing temperature of the thermoplastic [77], [95] and had been used by other researchers characterising the thermal properties of PEEK [110]. The heating rate and cooling rates of 10°C/min were selected because of their use by other research groups [110] and at the recommendation of CONCOM technical staff. With the chosen temperature and rates, each DSC cycle took approximately two hours to run.

For each sample, the melt temperature, enthalpy of melting, recrystallization temperature, and enthalpy of recrystallization were measured. When visible, the enthalpy of cold crystallization, cold crystallization temperature, and glass transition temperature were also recorded. Not all samples experienced cold crystallization. The glass transition temperature was not clearly visible in all samples either. The temperatures were not necessary for the crystallinity calculations, but they were recorded and compared against supplier data to validate the testing procedure. The glass transition, cold crystallization, melting, and recrystallization are all clearly visible on this DSC curve.

$$X = \frac{\Delta H_m - \Delta H_c}{(1 - \alpha)\Delta H_f} \quad (15)$$

Equation (15) was used to calculate the crystallinity, X, of the DSC samples [58], [111]. The enthalpy of fusion at melting, which is an endothermic peak, is represented by ΔH_m , while the enthalpy of cold crystallization is presented by ΔH_c [58], [111]. If there was no cold crystallization present, the value of this exothermic peak was set to 0. The values of both ΔH_m and ΔH_c were calculated using the “Integrate Peak – Linear” function in the TA Universal Analysis 2000 software [112]. The enthalpy of fusion for PEEK that is fully crystalline is represented by ΔH_f . This is reference value, which was taken to be 130J/g [58], [111], [113] for this experiment. Since 130J/g is the value for neat PEEK [58], [111], [113], the weight of the fibers must be subtracted. The constant α represents the weight fraction of the fibers [58], [111]. The manufacturer states that the weight fraction of the resin is 34% [77], [95], meaning that $1 - \alpha = 0.34$.

Chapter 5: Ring annealing results

The results from the annealing trials of the cylindrical samples are presented in this section. First is an overview of the samples laminate properties, including fiber volume fraction, void content, and crystallinity. These properties were measured for annealed and in-situ consolidated rings to see if the heat-treatment would have a negative impact on laminate properties. The fiber volume fraction and the void content were calculated using image analysis, while the crystallinity was measured with DSC. The respective procedures were outlined in section 4.7.

To determine effectiveness of the annealing on relieving the residual process stresses cylindrical samples, the strain was measured for cylindrical samples as they were being cut on a diamond saw. The hoop strain was recorded for the hoop-wound samples. The hoop, axial, and shear strains were recorded for the asymmetric samples.

5.1 Sample characterization

5.1.1 Fiber volume fraction

Given the annealing cycle was just the application of heat without the infiltration of any new polymer nor any compaction, the fiber volume fraction was not expected to change during annealing. At least 7 micrographs were taken per sample group. The layups were all photographed at 10 times magnification, while the tape was photographed at 20 times magnification. Fiber volume fraction results for tape, in-situ consolidated samples and annealed samples can be seen in Table 20. The average and standard deviation for each layup and each heat treatment can be seen at the bottom of the table.

Table 20: Fiber volume fraction for carbon fiber reinforced tape, in-situ consolidated samples and annealed samples

	Tape		In-situ			Annealed		
			90	45/90	90/45	90	45/90	90/45
Magnification:	20X		10X	10X	10X	10X	10X	10X
Pic #	Fiber %		Fiber %			Fiber %		
1	51.64%	50.83%	52.10%	46.93%	48.81%	48.85%	51.84%	52.14%
2	46.08%	51.95%	52.50%	50.21%	50.57%	48.89%	47.21%	52.62%
3	43.18%	46.25%	46.81%	53.08%	50.03%	47.65%	47.95%	55.40%
4	50.38%	54.65%	47.01%	53.94%	48.56%	50.47%	47.83%	49.06%
5	51.92%	52.04%	51.32%	49.72%	55.49%	50.11%	46.27%	50.51%
6	48.70%	48.11%	48.29%	55.85%	51.10%	52.37%	46.89%	45.93%
7	49.06%	49.93%	51.80%	51.65%	48.50%	49.95%	42.74%	52.70%
8	60.03%							50.04%
9								51.32%
10								54.05%
11								44.37%
Average	50.32%		49.98%	51.63%	50.44%	49.76%	47.25%	50.74%
			50.68%			49.49%		
Standard Dev.	3.81%		2.55%			2.96%		

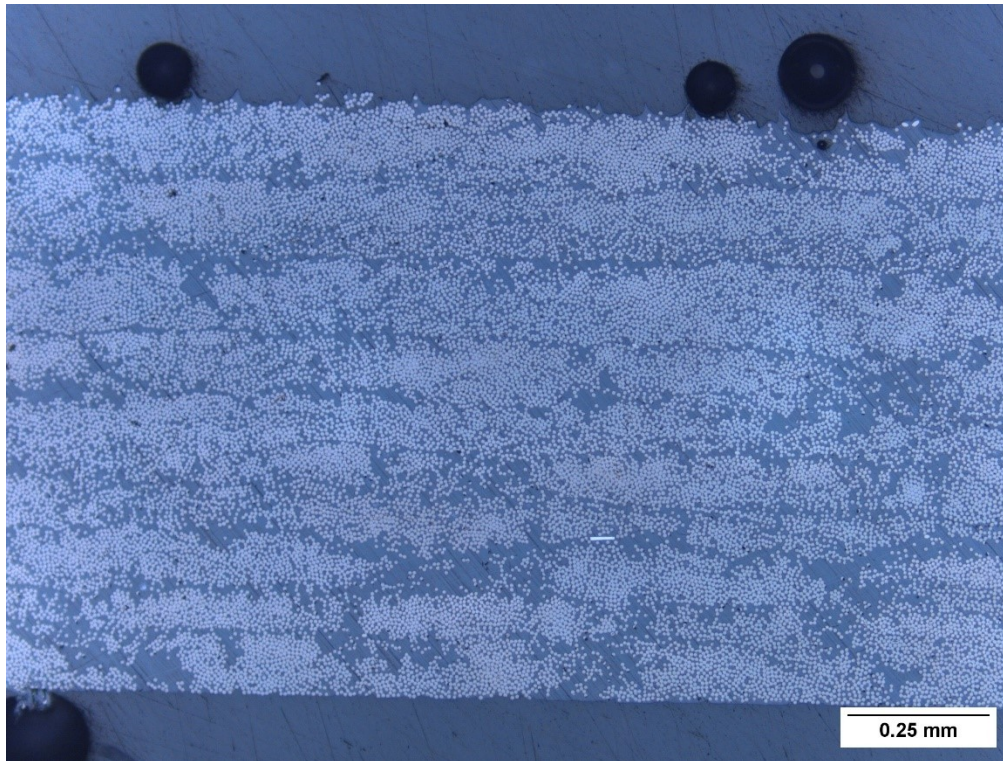


Figure 49: Micrograph for in-situ hoop-wound sample at 10 times magnification

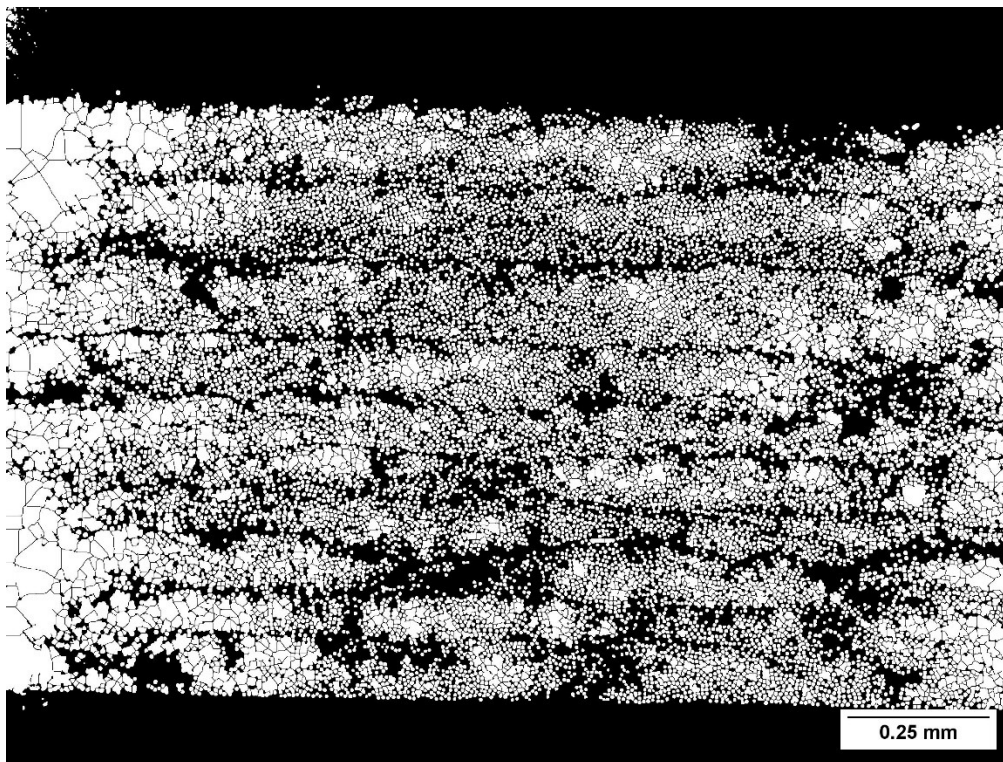


Figure 50: Binary image to isolate the fibers for in-situ hoop-wound sample (original image Figure 49) at 10 times magnification

Some representative micrographs were included in this section. The first set of images were taken from an in-situ consolidated hoop-wound sample. Figure 49 shows the original micrograph at 10 times magnification. Using the procedure outlined in section 4.7.1, that micrograph was converted into the binary black and white image seen in Figure 50. A representative area was cropped out of the center of the image. This region was then used by ImageJ to count the number of fibers present and what area they represented. The micrographs showed samples of good quality: there are few voids, a fairly even distribution of fibers, and few of the fibers appear to be broken. There are several resin rich pockets within and between the plies.

The next series of micrographs are from an annealed $[90_4, 45_4]_T$ sample. Figure 51 and Figure 52 show the original micrograph and the binary transformation of the image. This sample also appears to be of good quality and has resin rich pockets similar to the previous sample. In an attempt to explain where the resin rich areas came from, micrographs of the tape were also included in Figure 53.

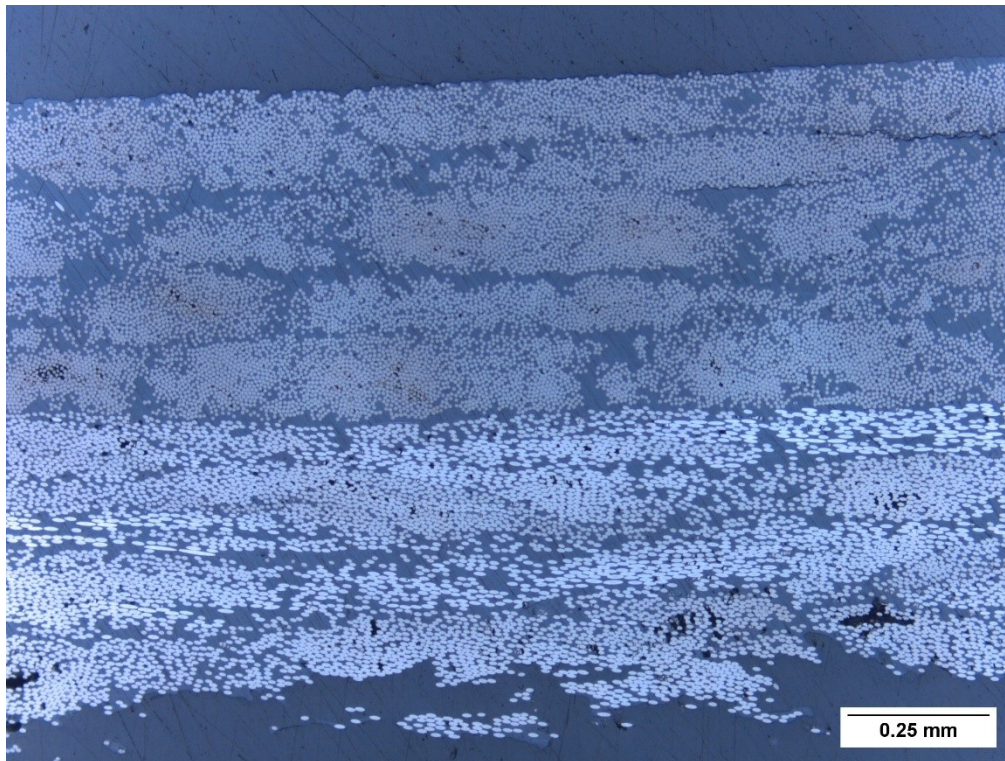


Figure 51: Micrograph for an annealed $[90_4, 45_4]_T$ sample at 10 times magnification

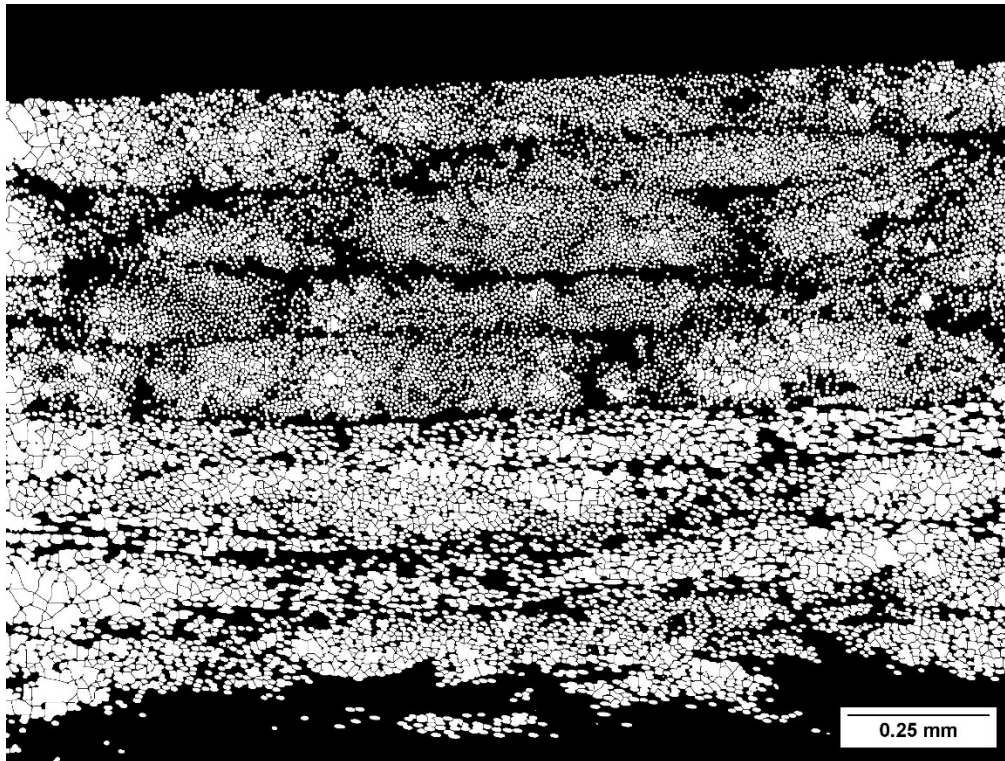


Figure 52: Binary image to isolate the fibers for an annealed $[90_4, 45_4]_T$ sample (original image Figure 51) at 10 times magnification

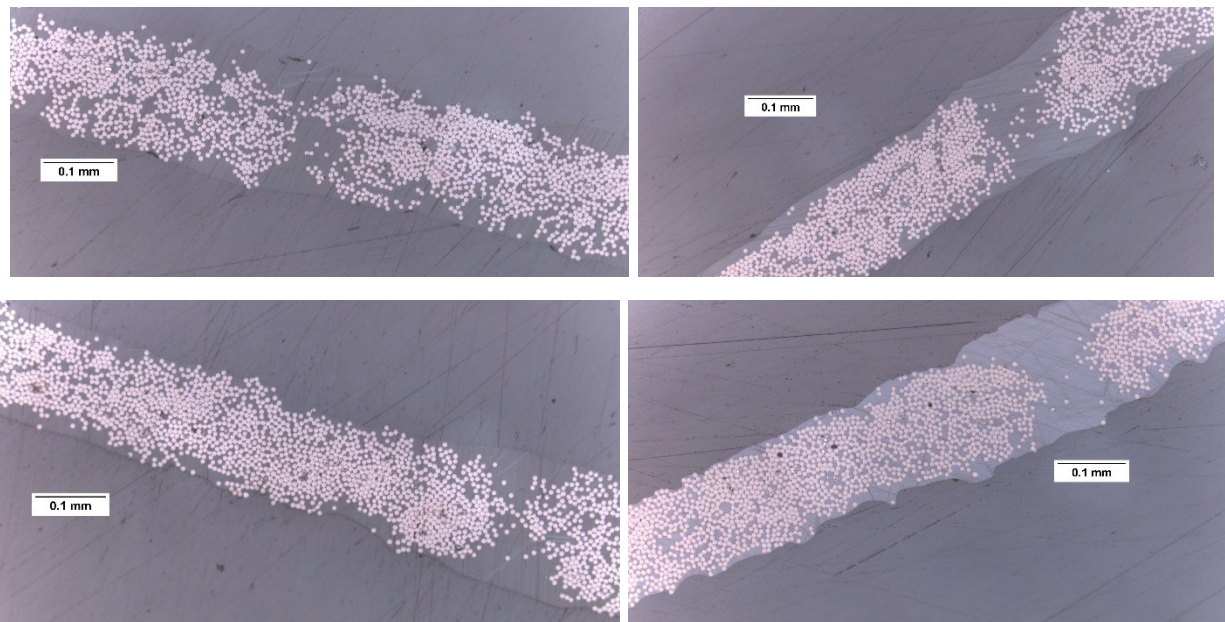


Figure 53: Compilation of tape micrographs with resin rich areas (20X magnification)

Most of the resin rich pockets seen in Figure 49 and Figure 51 are within the plies, rather than between them. This would suggest that those resin rich areas are a consequence of the tape quality rather than the manufacturing process. This was confirmed by the tape micrographs in Figure 53. The fibers were not uniformly distributed in the tape, leaving resin rich gaps.

5.1.2 Void content

No pressure was applied to the cylindrical samples during annealing. For this reason, the void content was not expected to change with annealing. In the aerospace industry, the permissible void content of primary structures is of 1% [114]. For secondary components, the permissible void content is of 5% [114]. This sets a target void content for these samples. The void content was calculated using image analysis. The results for the manufacturer’s tape, in-situ samples and annealed samples can be seen in Table 21. At least 6 measurements were taken for each layup. An average for each layup with the standard deviation, as well as an average for each heat treatment, can be seen at the bottom of the table.

Table 21: Void content for carbon fiber reinforced tape, in-situ consolidated samples and annealed samples

	Tape		In-situ			Annealed		
			90	45/90	90/45	90	45/90	90/45
Magnification:	20X		10X	10X	10X	10X	10X	10X
Pic #	Void %		Void %			Void %		
1	0.15%	0.31%	0.09%	0.98%	0.47%	0.31%	0.55%	0.27%
2	0.05%	0.55%	0.39%	3.22%	0.31%	0.11%	0.96%	0.21%
3	1.02%	0.20%	0.14%	1.38%	0.53%	0.18%	1.10%	0.39%
4	0.26%	1.05%	0.36%	1.56%	0.47%	0.28%	0.57%	0.16%
5	0.79%	0.30%	0.21%	0.90%	0.57%	0.48%	0.89%	0.53%
6	0.06%	3.34%	0.30%	1.01%	1.11%	0.44%	0.87%	1.51%
7	0.39%	0.38%	0.55%	1.03%	0.88%	0.68%		0.70%
8	0.18%	1.16%		1.49%	0.40%			1.53%
9	1.32%	0.61%						0.67%
10	0.23%							0.87%
11								0.25%
Average	0.45%		0.29%	1.45%	0.59%	0.36%	0.82%	0.64%
			0.78%			0.60%		
Standard Dev.	0.74%		0.67%			0.38%		

The micrograph analysis of two representative samples can be seen in the following pages. Figure 54 and Figure 55 show the initial micrograph and binary transformation for an annealed $[45_4, 90_4]_T$ sample. Note that these images were cropped prior to the image analysis. It would have been difficult to select a representative portion of the image with only the voids present. The micrograph and binary transformation for an in-situ consolidated $[90_4, 45_4]_T$ can be seen in Figure 56 and Figure 57 respectively. In both Figure 54 and Figure 56, it seems as though

most of the voids appear within each ply, rather than between this. This was true for the majority of the samples characterized here.

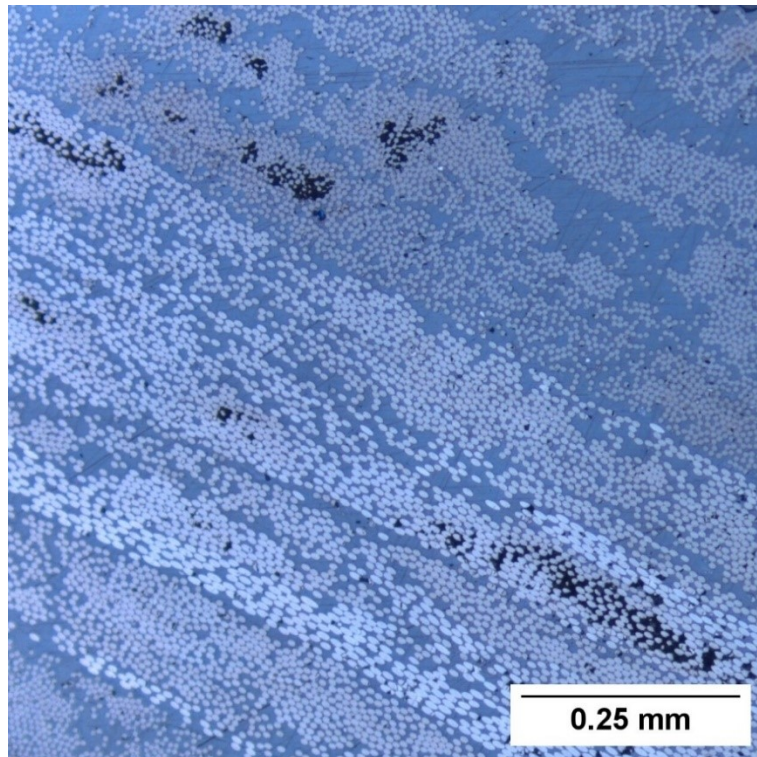


Figure 54: Cropped micrograph for annealed $[45_4, 90_4]_T$ sample

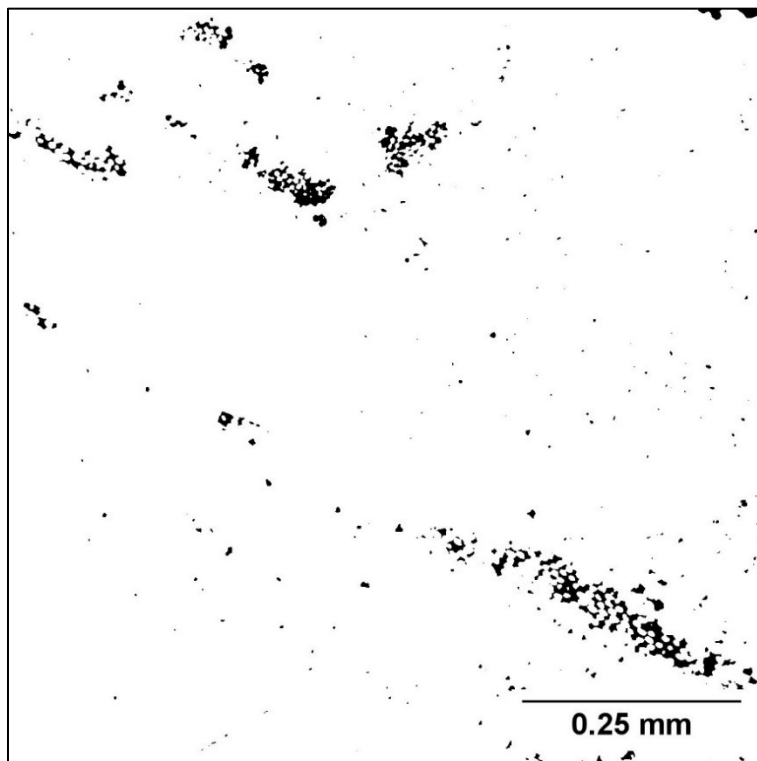


Figure 55: Binary transformation of annealed $[45_4, 90_4]_T$ sample to select the voids in the laminate

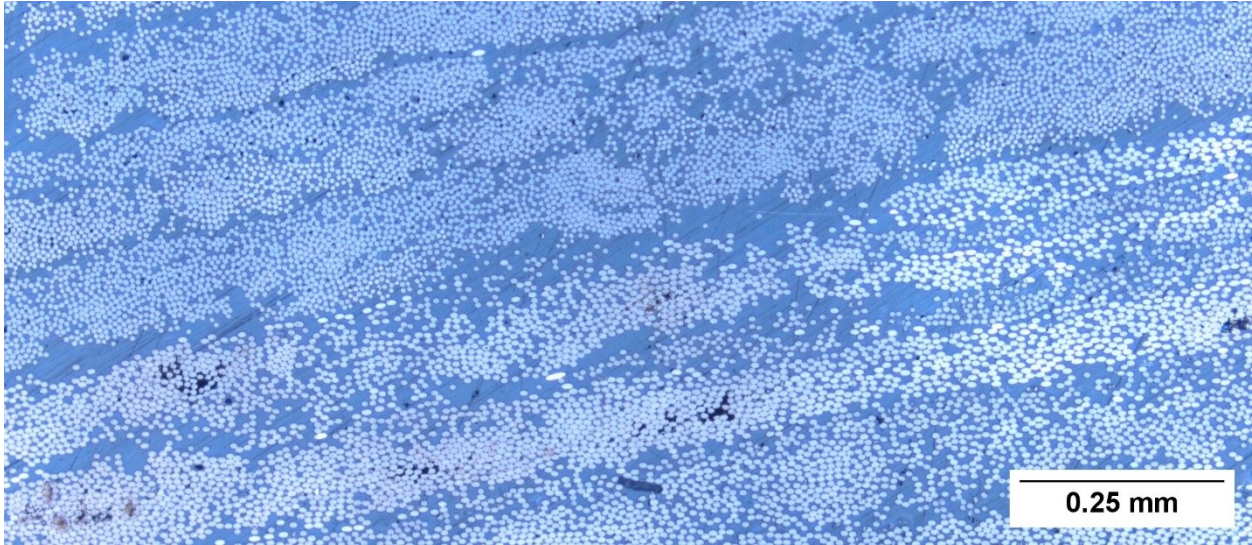


Figure 56: Cropped micrograph for in-situ $[90_4, 45_4]_T$ sample

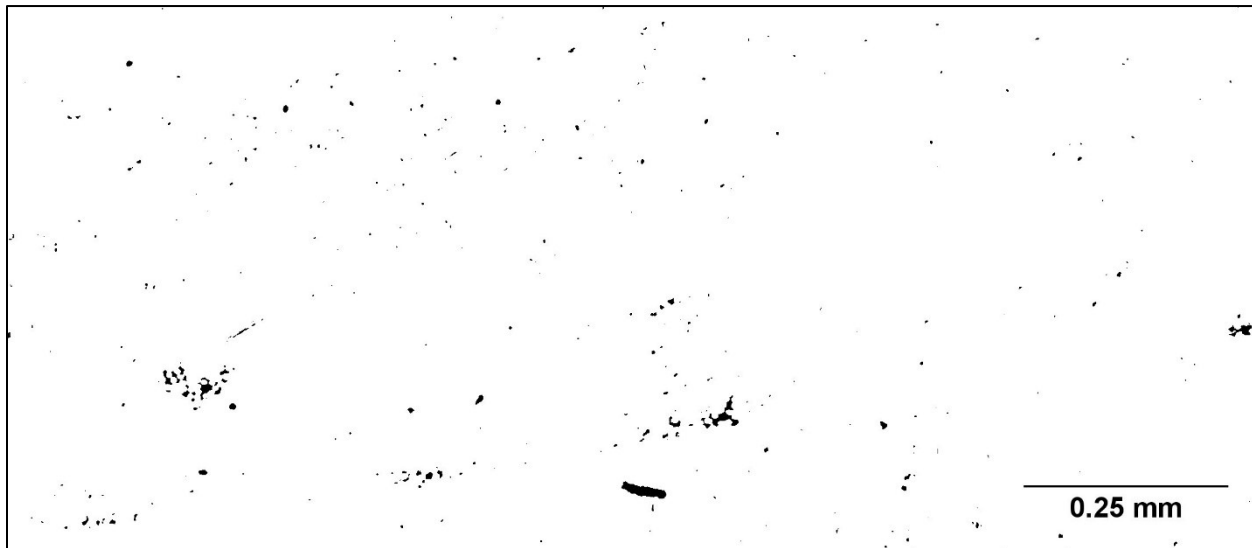


Figure 57: Binary transformation of annealed $[90_4, 45_4]_T$ sample to select the voids in the laminate

5.1.3 DSC crystallinity results

The glass transition temperature and cold crystallization temperature of PEEK are 143°C [77] and 180°C respectively [16]. Given that the samples were annealed to 200°C , which is significantly above cold crystallization temperature, the crystallinity of the samples was expected to increase with heat treatment. The crystallinity of the samples was measured using DSC at three stages during the sample manufacturing. First, the tape from the supplier was tested. Next, in-situ consolidated samples were tested after manufacturing. Finally, samples were tested after annealing. The crystallinity from these three stages as well as the standard deviation (σ) for each group can be seen in Table 22.

Table 22: Crystallinity for tape, un-annealed samples and annealed samples

Heat treatment	Layup	Glass Transition temperature (°C)	Enthalpy of Cold Crystallization (J/g)	Enthalpy of Melt (J/g)	Crystallinity	Average Crystallinity	Average Crystallinity
None	Tape	145.71	8.719	12.21	8%	8% $\sigma = 1\%$	Tape: 8%
		144.53	9.173	13.36	9%		
		145.37	7.749	10.56	6%		
In-situ	[90] ₈	-	0	9.691	22%	23% $\sigma = 1\%$	In-situ: 20% $\sigma = 4\%$
		-	0	10.51	24%		
		-	0	10.79	24%		
	[90 ₄ , 45 ₄] _T	145.99	2.993	12.13	21%	16% $\sigma = 4\%$	
		145.05	2.743	7.824	11%		
		-	1.299	8.667	17%		
	[45 ₄ , 90 ₄] _T	-	1.651	10.26	19%	19% $\sigma = 0\%$	
		146.06	3.393	11.94	19%		
		-	1.034	9.379	19%		
Annealed	[90] ₈	-	0	12.29	28%	25% $\sigma = 2\%$	Annealed: 27% $\sigma = 5\%$
		143.73	0	11.08	25%		
		-	0	9.803	22%		
	[90 ₄ , 45 ₄] _T	-	0	13.23	30%	33% $\sigma = 2\%$	
		-	0	15.16	34%		
		-	0	14.95	34%		
	[45 ₄ , 90 ₄] _T	-	0	11.33	26%	23% $\sigma = 2\%$	
		-	0	9.65	22%		
		-	0	9.397	21%		

Some representative DSC curves are shown in the following figures. Figure 58 shows the data for the reinforced thermoplastic tape. It is labeled to show the glass transition temperature, cold crystallization, melting, and recrystallization behavior of the thermoplastic. Figure 59 shows the curve for an annealed [90]₈ sample. None of the hoop-wound samples showed any cold crystallization peaks. Figure 60 presents the data for an in-situ consolidated [90₄, 45₄]_T sample. Note that all of the in-situ consolidated bi-directional laminates had cold crystallization. Figure 61 shows the results for an annealed [45₄, 90₄]_T laminate. None of the annealed asymmetric samples exhibited any cold crystallization.

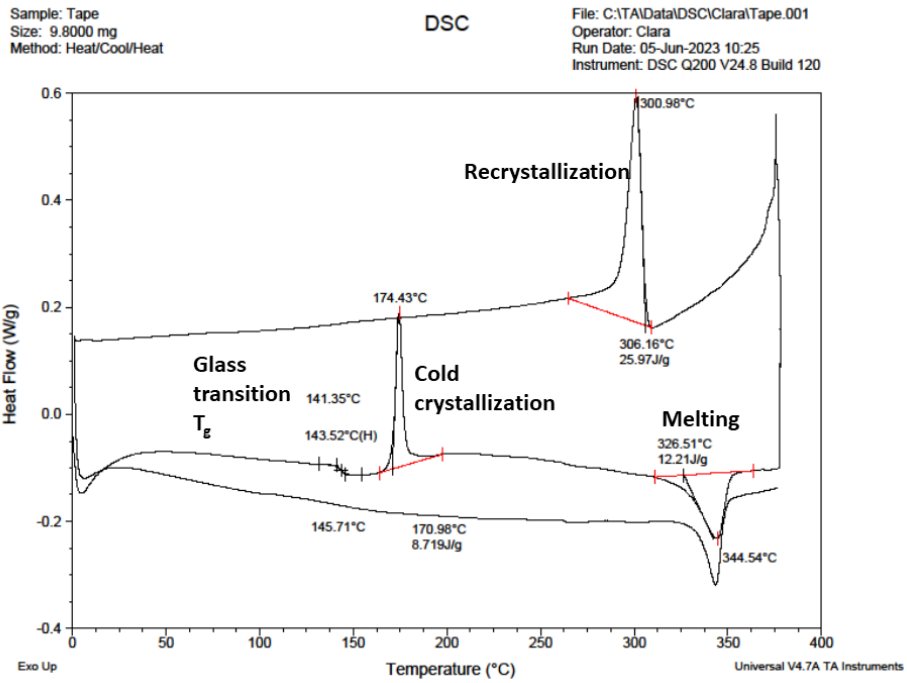


Figure 58: DSC results for a sample of carbon fiber reinforced thermoplastic tape

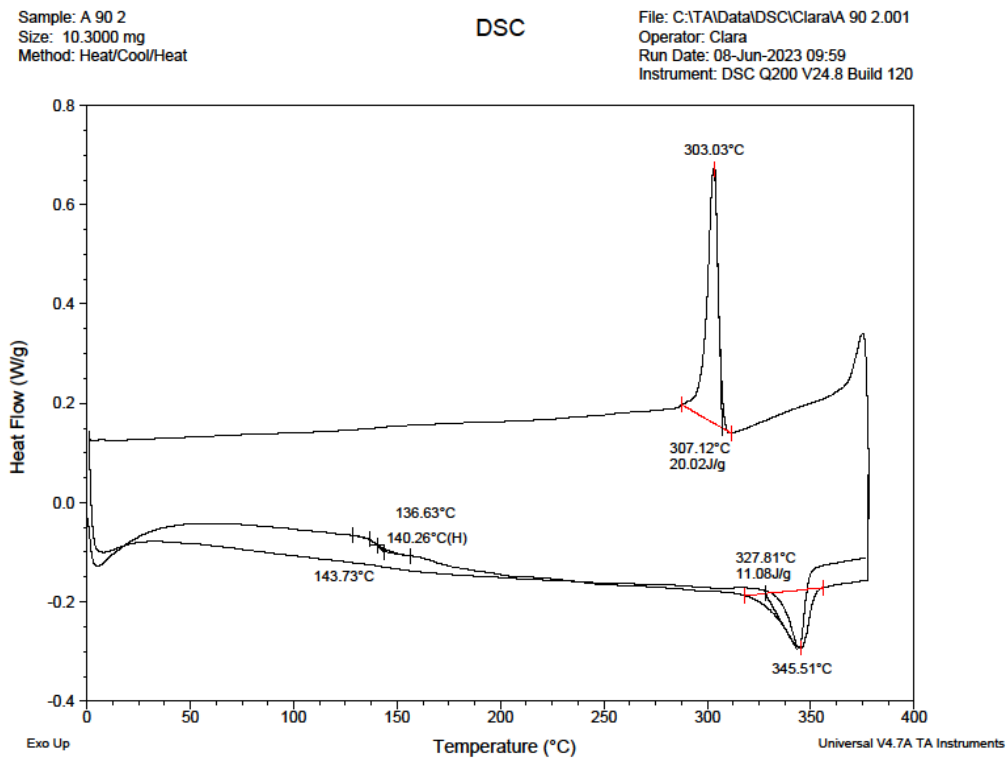


Figure 59: DSC results for a sample for annealed $[90]_8$ sample

Sample: NA 90 45 3
Size: 13.1000 mg
Method: Heat/Cool/Heat

DSC

File: C:\TA\Data\DSC\Clara\NA 90 45 3.001
Operator: Clara
Run Date: 14-Jun-2023 10:49
Instrument: DSC Q200 V24.8 Build 120

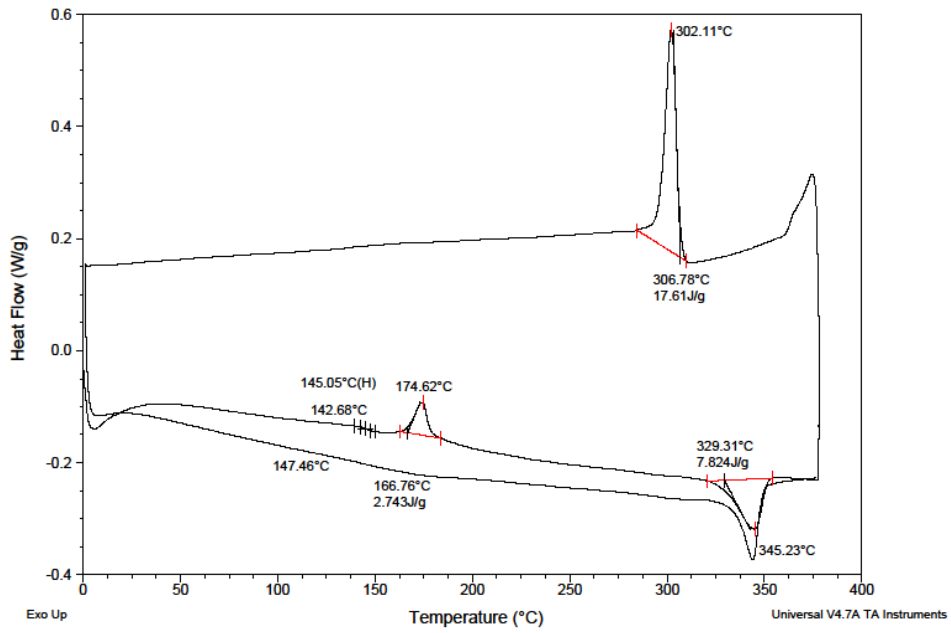


Figure 60: DSC results for a sample for not annealed $[90_4, 45_4]_T$ sample

Sample: A 45 90 2
Size: 10.1000 mg
Method: Heat/Cool/Heat

DSC

File: C:\TA\Data\DSC\Clara\A 45 90 2.001
Operator: Clara
Run Date: 12-Jun-2023 10:07
Instrument: DSC Q200 V24.8 Build 120

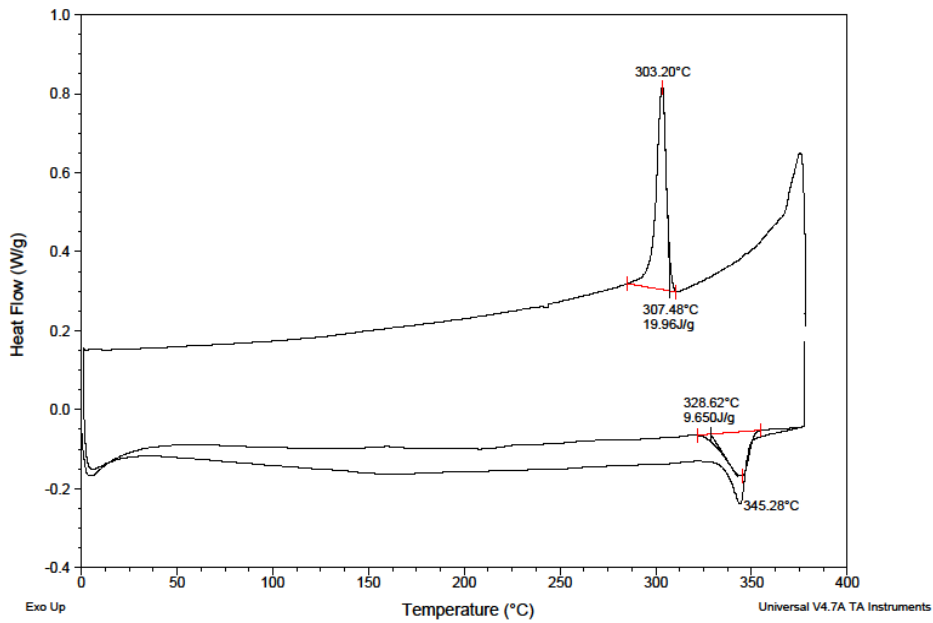


Figure 61: DSC results for a sample for annealed $[45_4, 90_4]_T$ sample

5.2 Strain measurements

Strain measurements were gathered using strain gages and the Model 8000-8-SM data acquisition system manufactured by Micro-Measurements. This system connects to a laptop via an ethernet cable and all the data collection is managed with a proprietary software called StrainSmart 8000. The manufactured tubes were annealed (if applicable) and then sectioned into rings. Next, the strain gages were then installed. Finally, the samples were slit.

5.2.1 Unidirectional samples

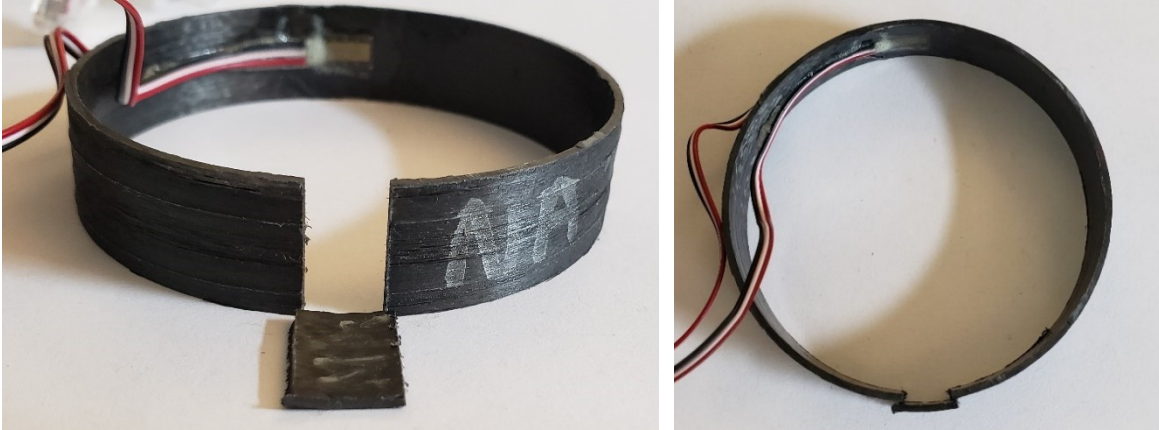


Figure 62: In-situ hoop-wound sample exhibiting spring in behavior

All of the unidirectional hoop-wound samples sprung inwards in the circumferential direction without any twisting. This meant that 2 cuts were necessary to fully relieve the residual stresses. The first cut only partially relieved the stresses because the two cut edges sprang back together, butting against each other. To fully relieve the residual stresses, a second cut had to be made, approximately half an inch away from the first one. This gap was then sufficiently large for the sample to spring inwards its full extent. This fully deformed sample is going to be considered the ring's stress-free state, meaning that all these residual strains that were initially trapped in the solid ring have been released and measured. Once cut, the sample had a free edge and the residual stresses can be observed. The sample is now at equilibrium. In Figure 62, a sample after both cuts can be seen next to the portion of the ring which was removed. Note that approximately 3mm (1.5mm per cut) of material is lost due to the kerf of the blade.

Table 23: Measured Residual strain for in-situ and annealed hoop-wound samples

Heat treatment		Cut 1: Strain (microstrain)						Cut 2: Strain (microstrain)						Difference	
		Outer Surface			Inner Surface			Outer Surface			Inner Surface			Out	In
		Before	After	Diff	Before	After	Diff	Before	After	Diff	Before	After	Diff		
In-situ	1				0	23	23				3	-224	-227		-250
	2	-7	-5	2	-2	-77	-75	11	344	333	8	-280	-288	331	-213
	3			0			0	1	410	409	2	-370	-372	409	-372
Standard Deviation													39	68	
Anneal	1				11	-93	-104			0	72	-152	-224		-120
	2	1	44	43	4	-9	-13	0	344	344	4	-337	-341	301	-328
	3			0			0	-1	402	403	-1	-364	-363	403	-363
Standard Deviation													51	107	

Table 23 shows all the strain data collected on the inner and outer surfaces for the hoop-wound samples. ‘Cut 1’ refers to the initial cut which partially relieves the strain. The strain values are so small at this stage because the strain was only relieved in the 1.5mm wide cutaway section. ‘Cut 2’ represents the second cut, which fully relieves the strain in the sample. For each cut, the difference between the initial near-zero strain and the final strain after cutting represents the total strain relieved. The final difference recorded is the difference between the overall strain from cuts 2 and 1.

Figure 63 shows the strain as a function of time for ‘Cut 2’ of the second annealed sample from Table 23. The data acquisition system used only allows for strain to be measured as a function time. The graph has an initial plateau, a noisy transition time while the cut is being performed, and a final plateau which represents the final strain. The strain variation during the cutting is not of interest. Instead, the strain recorded before and after are what are being retained. Despite zeroing the gages before the cutting, most of the gages read a small initial strain value. The difference between the plateau values before and after cutting is taken to be the strain relieved in that cut. The difference between cut 1 and cut 2 represents the total strain relieved.

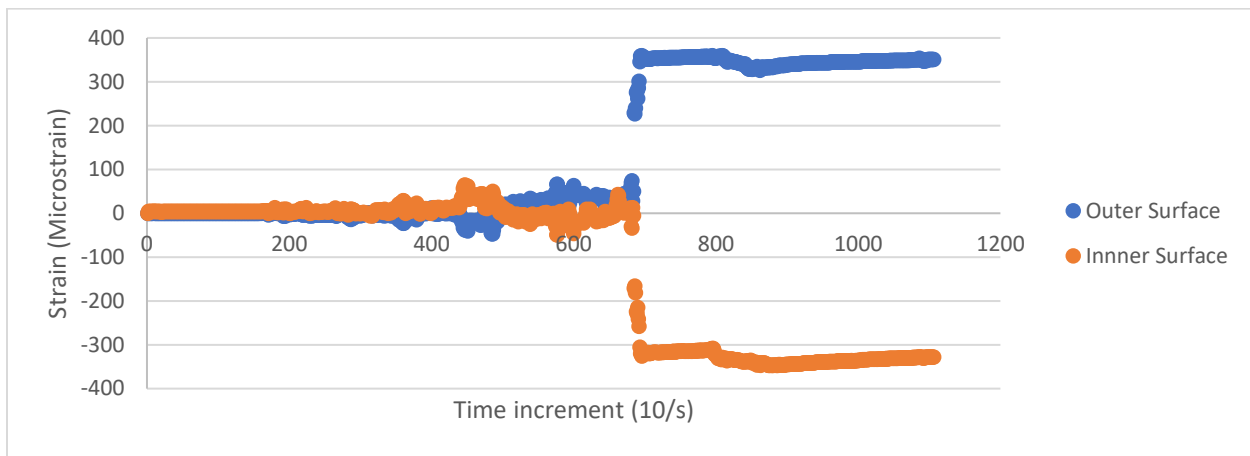


Figure 63: Strain as a function of time (10 datapoints per second) for annealed hoop-wound sample 2, cut 2

There are a few things to note in Table 23 with regards to missing data. For the first trial of both samples, the strain gages on the outer surfaces broke during installation. The strain gages are naturally slightly concave. This means that they are opposite in curvature to the outer surface of the samples and need to be held in place longer for them to cure fully which may have potentially damaged one of the contacts. Additional care was used for the subsequent installations of gages on the outer surfaces of the rings to avoid any more breakage. Given that a single strain reading is not sufficient to satisfy the two boundary conditions needed for the ODE in section 6.2, these entries could not be plotted. When the first 2 trials did not show any significant change with annealing, the protocol for the third pair of rings was revised slightly. For the third pair of rings, the first cut was made on the samples, then the annealed sample was re-annealed to 200°C. Given that this sample now had a free edge, it was hypothesized that the annealing might have a greater effect. After the re-annealing, the strain gages were attached to both rings and the second cut was made. In this case, it was not possible record the strain relieved during the first cut because the gages would not have been able to survive the heat treatment. The small amount of strain that would have been relieved was assumed to be zero.

Another way to quantify the deformation of the samples is to measure their radii before and after the destructive testing. The results for all of the hoop-wound samples can be seen in Table 24. These measurements were made using the image analysis software Digimizer. The outer radii of each sample were measured 3 times and averaged.

Table 24: Outer radii of in-situ and annealed samples before and after cutting

Heat treatment	Outer radius (cm)									
	Before Cutting					After Cut 2				
	1	2	3	AVG	AVG	1	2	3	AVG	AVG
In-situ	3.5579	3.5017	3.5123	3.5240	3.6810	3.667	3.586	3.652	3.635	3.5447
	3.7533	3.8546	3.7338	3.7806		3.498	3.500	3.463	3.487	
	3.7279	3.7145	3.7727	3.7384		3.516	3.516	3.503	3.512	
Annealed	3.5694	3.5623	3.6171	3.5830	3.6263	3.576	3.669	3.684	3.643	3.6087
	3.6106	3.5798	3.5902	3.5935		3.716	3.685	3.695	3.699	
	3.6857	3.7563	3.6655	3.7025		3.481	3.500	3.473	3.485	
In-situ	Difference:			-1.3629mm		Average standard deviation:			0.99mm	
Annealed	Difference:			-0.1764mm		Average standard deviation:			0.83mm	

5.2.2 Asymmetric samples

All of the asymmetric samples in this experiment were comprised of 4 consecutive layers at 90° and 4 consecutive layers at 45°. The $[90_4, 45_4]_T$ samples, which have the 90° plies as the innermost layers sprung open and twisted when cut. An example can be seen in Figure 64. The $[45_4, 90_4]_T$ samples all sprung closed and also twisted when cut. They had the 45° layers towards the centre. Figure 65 shows an example of a $[45_4, 90_4]_T$ sample. All of the asymmetric samples twisted enough that 1 cut was necessary to fully relieve the residual stresses. The direction of the springing was anticipated when these samples were designed. Given the more complex nature of the deformation, rosettes were used to capture the strain in the samples before, during, and after, cutting. Gages were placed on the inner and outer surfaces such that they capture the circumferential (or hoop) direction, the shear (at 45°) direction, and the transverse direction (along the length of the cylinder). The strain of cutting as a function of time for an in-situ consolidated $[90_4, 45_4]_T$ sample can be seen in Figure 66. The time elapsed was the duration of the cut. The difference between the initial near-zero plateau and the final strain values represents the strain relieved in these samples, since only one cut was necessary for the samples to reach their stress-free state.

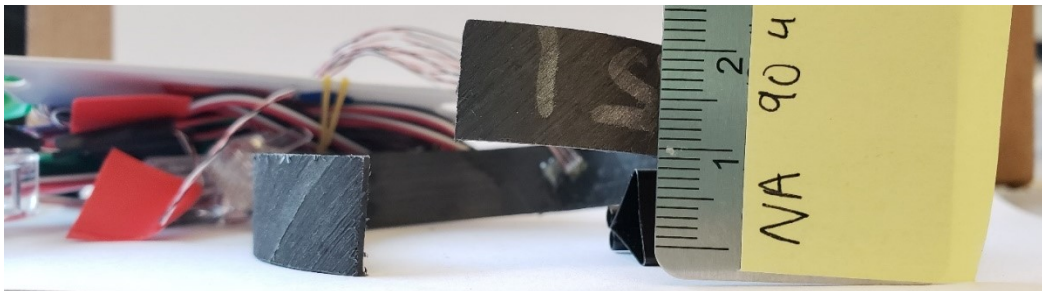


Figure 64: In-situ consolidated $[90_4, 45_4]_T$ sample with one cut experiencing spring out behavior

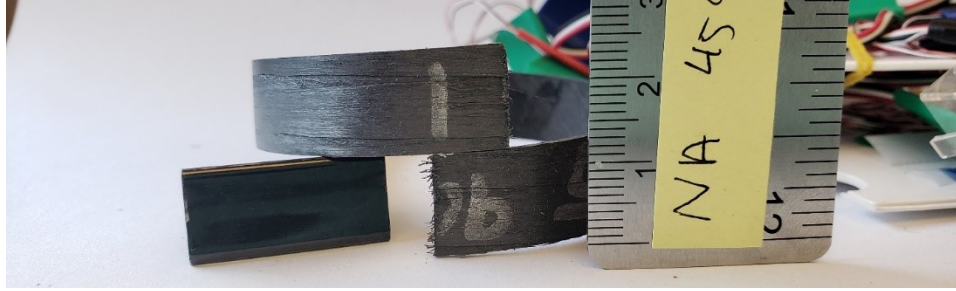


Figure 65: In-situ consolidated $[45_4, 90_4]_T$ sample with one cut experiencing spring in behavior

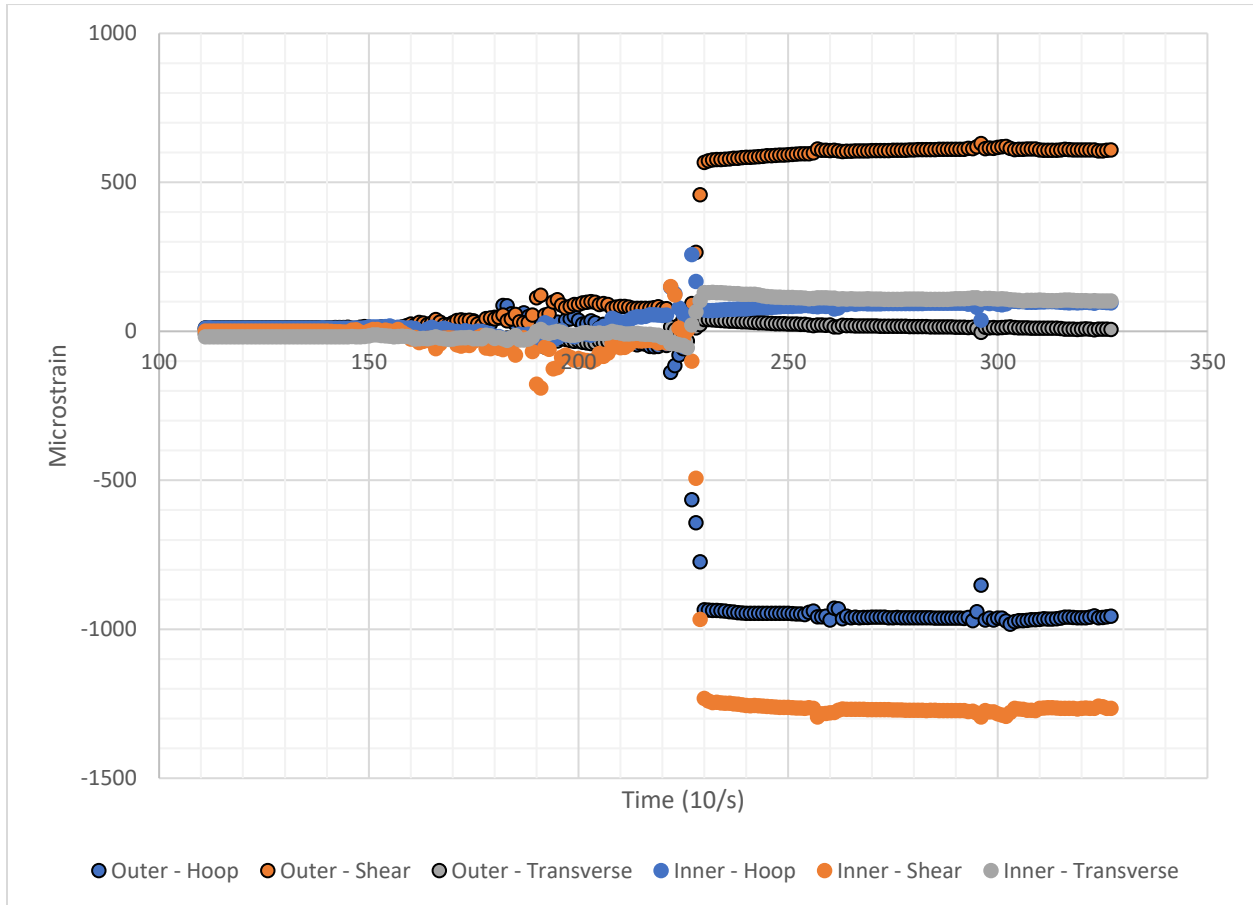


Figure 66: Strain as a function of time (10 datapoints per second) during cutting procedure for in-situ $[90_4, 45_4]_T$ sample

The residual strain that was relieved from all of the $[90_4, 45_4]_T$ samples can be seen in Table 25. Table 26 contains all of the strain data for the $[45_4, 90_4]_T$ samples. The average strain values as well as the standard deviations for the circumferential strain are also indicated in each table. This data is organized according to the sample layup and heat-treatment. Note that there are only 2 in-situ samples for the $[45_4, 90_4]_T$ layup. One of the contacts on the strain gage broke off during handling. In an effort to get useable data, a secondary gage was placed next to the original rosette. Unfortunately, this gage provided data different from the other samples in this category. This likely happened because the gage was not aligned with the cut made to relieve the strain.

Table 25: Measured Residual strain for in-situ and annealed [90₄, 45₄]_T samples

Heat treatment	Strain (microstrain)										
	Outer Strain Gage										
	Hoop (Grid 1)					Shear (Grid 2)			Transverse (Grid 3)		
	Before	After	Diff	AVG	Std. Dev.	Before	After	Diff	Before	After	Diff
In-situ	6	-959	-965	-787	206	11	609	598	-9	14	23
	-5	-503	-498			1	643	642	0	-341	-341
	3	-894	-897			20	518	498	-11	-74	-63
Annealed	-1	-1330	-1329	-1004	236	-3	521	524	1	112	111
	5	-899	-904			11	855	844	-15	-160	-145
	1	-777	-778			13	837	824	-22	-288	-266
Heat treatment	Inner Strain Gage										
	Hoop (Grid 3)										
	Hoop (Grid 3)					Shear (Grid 2)			Transverse (Grid 1)		
	Before	After	Diff	AVG	Std. Dev.	Before	After	Diff	Before	After	Diff
In-situ	12	92	80	155	56	1	-1271	-1272	-19	107	126
	0	172	172			1	-1323	-1324	3	-34	-37
	18	231	213			9	-1027	-1036	-17	-108	-91
Annealed	-4	427	431	281	109	-3	-1374	-1371	2	-331	-333
	19	192	173			5	-1432	-1437	-23	-209	-186
	21	260	239			1	-1562	-1563	-36	-153	-117

Table 26: Measured Residual strain for in-situ and annealed [45₄, 90₄]_T samples

Heat treatment	Strain (microstrain)										
	Outer Strain Gage										
	Hoop (Grid 1)					Shear (Grid 2)			Transverse (Grid 3)		
	Before	After	Diff	AVG	Std. Dev.	Before	After	Diff	Before	After	Diff
In-situ	-1	718	719	469	496	0	-1010	-1010	2	-168	-170
	-2	909	911			7	-993	-1000	-5	-535	-530
Annealed	-1	341	342	669	461	-1	-1193	-1192	-2	477	479
	-2	343	345			-3	-869	-866	-3	260	263
	5	1326	1321			14	-666	-680	-32	-545	-513
Heat treatment	Inner Strain Gage										
	Hoop (Grid 3)										
	Hoop (Grid 3)					Shear (Grid 2)			Transverse (Grid 1)		
	Before	After	Diff	AVG	Std. Dev.	Before	After	Diff	Before	After	Diff
In-situ	0	-667	-667	-363	377	-2	594	596	2	-916	-918
	-3	-594	-591			-10	792	802	-9	-792	-783
Annealed	1	-1010	-1011	-1228	362	-1	879	880	-1	-1084	-1083
	1	-934	-935			0	670	670	-1	-581	-580
	13	-1726	-1739			21	658	637	-20	-426	-406

The radius of all the samples before and after cutting was also recorded. Table 27 contains the radius values for the $[90_4, 45_4]_T$ samples, while Table 28 had all the radii for the $[45_4, 90_4]_T$ samples. These tables show the average outer radius measurements for each sample, as well as the average for each heat treatment. The difference in radius before and after cutting indicates how much the samples sprang in or out during annealing.

Table 27: Outer radii of $[90_4, 45_4]_T$ in-situ and annealed samples before and after cutting

Heat treatment	Outer radius (cm)									
	Before Cutting					After Cutting				
	1	2	3	AVG	AVG	1	2	3	AVG	AVG
In-situ	3.6128	3.6609	3.6280	3.6339	3.6310	3.904	3.977	4.071	3.984	3.9775
	3.6667	3.6754	3.6653	3.6691		3.907	3.977	4.109	3.998	
	3.5717	3.6283	3.5697	3.5899		3.875	3.904	4.074	3.951	
Annealed	3.6703	3.6577	3.6542	3.6607	3.6256	3.830	3.921	4.070	3.941	3.9361
	3.5728	3.5582	3.5587	3.5633		3.900	4.004	4.008	3.971	
	3.6807	3.6312	3.6466	3.6528		3.837	3.859	3.994	3.897	
In-situ	Difference:			3.4649mm		Average standard deviation:			0.64mm	
Annealed	Difference:			3.1046mm		Average standard deviation:			0.68mm	

Table 28: Outer radii of $[45_4, 90_4]_T$ in-situ and annealed samples before and after cutting

Heat treatment	Outer radius (cm)									
	Before Cutting					Before Cutting				
	1	2	3	AVG	AVG	1	2	3	AVG	AVG
In-situ	3.6166	3.6974	3.6438	3.6526	3.6517	3.638	3.603	3.485	3.575	3.4896
	3.6443	3.6744	3.6847	3.6678		3.452	3.403	3.326	3.393	
	3.6152	3.6740	3.6146	3.6346		3.537	3.517	3.446	3.500	
Annealed	3.7817	3.7117	3.6281	3.7072	3.7377	3.461	3.498	3.601	3.520	3.4886
	3.7316	3.7203	3.8910	3.7810		3.648	3.489	3.417	3.518	
	3.7119	3.7613	3.7019	3.7250		3.463	3.442	3.378	3.428	
In-situ	Difference:			-1.6209mm		Average standard deviation:			0.65mm	
Annealed	Difference:			-2.4915mm		Average standard deviation:			0.79mm	

Chapter 6: Stress from strain calculations

This section is going to outline the equations used to calculate the residual stresses present in the samples from the experimentally measured strains. This will allow for a comparison between residual stresses present in the in-situ consolidated samples and the annealed samples. These stresses were calculated using classical laminate theory or a coordinate transformation from cartesian coordinates to cylindrical coordinates. First, the strains measured on the inner and outer surfaces of the ring were used to calculate the strain gradient within the sample. From this gradient, the residual stresses within the samples could be calculated.

The mechanical properties used for calculating the stresses from the measured strains can be seen in Table 29 along with their respective sources. The laminae are assumed to be transversely isotropic, meaning that the properties perpendicular to the fibers in the 2 direction and through the thickness of the laminae are the same [22].

Table 29: Mechanical properties used to calculate residual stresses

0° Young's modulus	E_1	138 GPa	[77]
0° Poisson's ratio	ν_{12}	0.30	[77]
90° Young's modulus	E_2, E_3	10.3 GPa	[77]
Shear modulus	G_{12}, G_{13}	5.7 GPa	[77]
90° Poisson's ratio through thickness	ν_{23}	0.32	[115]

6.1 Classical laminate theory (CLT)

Classical laminate theory is the traditional method of calculating stress from strain for flat laminates. An approximation of the coordinate system when applied to cylindrical geometries can be seen in Figure 67 [22]. The x-axis is along the length of the cylinder, while the y-axis described the circumferential (hoop) direction. The stresses through the thickness of the laminate (in the radial direction) are not being considered [22]. However, one of the advantages of this approach is that it can describe any twisting motion as movement along the y-axis.

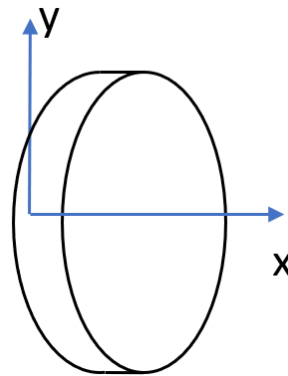


Figure 67: Coordinate system for CLT

The approach by Hyer in *Stress Analysis of Fiber-Reinforced Composite Materials* [22] was used here. More specifically, chapters 4, 6, and 7 which describe plane stress behavior, Kirchhoff's hypothesis, and definition of the ABD matrix were used [22]. The shear in the x and

y directions would be measured using the installed rectangular rosettes. Given that these gages are 90° apart, the shear strain is simply the difference between these 2 values [116].

$$\begin{Bmatrix} N_x \\ N_y \\ N_{xy} \\ M_x \\ M_y \\ M_{xy} \end{Bmatrix} = \begin{bmatrix} A_{11} & A_{12} & A_{16} & B_{11} & B_{12} & B_{16} \\ A_{12} & A_{22} & A_{26} & B_{12} & B_{22} & B_{26} \\ A_{16} & A_{26} & A_{66} & B_{16} & B_{26} & B_{66} \\ B_{11} & B_{12} & B_{16} & D_{11} & D_{12} & D_{16} \\ B_{12} & B_{22} & B_{26} & D_{12} & D_{22} & D_{26} \\ B_{16} & B_{26} & B_{66} & D_{16} & D_{26} & D_{66} \end{bmatrix} \begin{Bmatrix} \varepsilon_x^0 \\ \varepsilon_y^0 \\ \gamma_{xy}^0 \\ \kappa_x^0 \\ \kappa_y^0 \\ \kappa_{xy}^0 \end{Bmatrix} \quad (16)$$

Kirchhoff's hypothesis assumes a linear strain distribution throughout the laminate caused by the bending of the laminate [22]. From the strains measured on the inner and outer surfaces of the samples, it is possible to interpolate the strain at every ply interface since the distribution is assumed to be linear. From there, the strains at the midplane ($\varepsilon_x^0, \varepsilon_y^0, \gamma_{xy}^0$) is assumed to be a consequence of the force resultants N_x, N_y, N_{xy} . The midplane strain can then be subtracted from the strain at each interface, leaving behind the strain caused by the bending moment resultants (M_x, M_y, M_{xy}). Dividing these strains by their distance from the midplane provides the curvature ($\kappa_x^0, \kappa_y^0, \kappa_{xy}^0$). Using the midplane strain, curvature, and the sample's ABD matrix, it is possible to calculate the force and moment resultants in each sample using equation (16) [22].

It was also assumed that the laminae were transversely isotropic and subject to plane stress conditions. The properties of the laminae perpendicular to the fiber direction and through the laminae's thickness were assumed to be the same.

6.2 Stress-strain relations for thin cylindrical shells

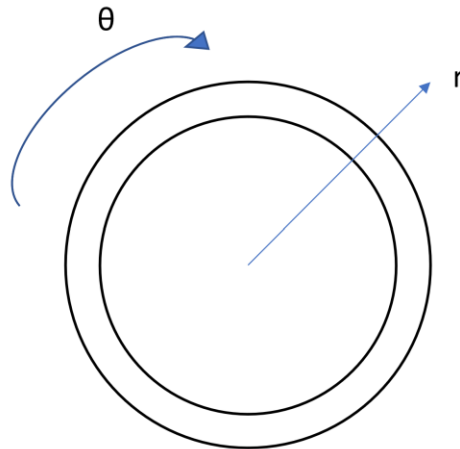


Figure 68: Cylindrical coordinates, showing the circumferential and radial directions

An alternative to using CLT is to approximate the composite rings as short, thin cylindrical shells and transform the measured strains into cylindrical coordinates. The approach by Hyer in *Stress Analysis of Fiber-Reinforced Composite Materials* [22] was only to calculate 3D compliance matrix for these samples. From there, it would be possible to transform the

material properties into cylindrical coordinates. This coordinate system can be seen in Figure 68. The major difference between this coordinate system and CLT is that stresses through the laminate (in the radial direction) are a critical component. Instead, the stresses along the length of the tube are considered to be zero since the ring is short when compared to its radius [64].

The stresses in the circumferential direction are assumed to not vary with the angle (axisymmetric) [37]. This assumption is counterintuitive, since the cut ring is obviously not axisymmetric in its strain distribution given the presence of the slit. However, the cut ring represents the stress-free state of the ring, since all the strain was released during the destructive test. These stresses must have all been present in the solid ring beforehand. The stressed ring, before cutting, is what is being represented by this system of equations. Given that the geometry is still closed at this stage, it can be assumed to be axisymmetric.

6.2.1 Compliance matrix transformation

Before any stress or strain calculations can be done, it is important to first transform the compliance matrix for the transversely isotropic composite into cylindrical coordinates. From Hyer [22], the 6 by 6 compliance matrix for a transversely isotropic composite can be defined by equations (17) and (18).

$$\begin{Bmatrix} \varepsilon_1 \\ \varepsilon_2 \\ \varepsilon_3 \\ \gamma_{23} \\ \gamma_{13} \\ \gamma_{12} \end{Bmatrix} = \begin{bmatrix} S_{11} & S_{12} & S_{13} & 0 & 0 & 0 \\ S_{12} & S_{22} & S_{23} & 0 & 0 & 0 \\ S_{13} & S_{23} & S_{33} & 0 & 0 & 0 \\ 0 & 0 & 0 & S_{44} & 0 & 0 \\ 0 & 0 & 0 & 0 & S_{55} & 0 \\ 0 & 0 & 0 & 0 & 0 & S_{66} \end{bmatrix} \begin{Bmatrix} \sigma_1 \\ \sigma_2 \\ \sigma_3 \\ \tau_{23} \\ \tau_{13} \\ \tau_{12} \end{Bmatrix} \quad (17)$$

$$[S] = \begin{bmatrix} S_{11} & S_{12} & S_{12} & 0 & 0 & 0 \\ S_{12} & S_{22} & S_{23} & 0 & 0 & 0 \\ S_{12} & S_{23} & S_{22} & 0 & 0 & 0 \\ 0 & 0 & 0 & S_{44} & 0 & 0 \\ 0 & 0 & 0 & 0 & S_{55} & 0 \\ 0 & 0 & 0 & 0 & 0 & S_{55} \end{bmatrix} = \begin{bmatrix} \frac{1}{E_1} & -\frac{\nu_{12}}{E_1} & -\frac{\nu_{12}}{E_1} & 0 & 0 & 0 \\ -\frac{\nu_{12}}{E_1} & \frac{1}{E_2} & -\frac{\nu_{23}}{E_2} & 0 & 0 & 0 \\ -\frac{\nu_{12}}{E_1} & -\frac{\nu_{23}}{E_2} & \frac{1}{E_2} & 0 & 0 & 0 \\ 0 & 0 & 0 & \frac{2(1+\nu_{23})}{E_2} & 0 & 0 \\ 0 & 0 & 0 & 0 & \frac{1}{G_{12}} & 0 \\ 0 & 0 & 0 & 0 & 0 & \frac{1}{G_{12}} \end{bmatrix} \quad (18)$$

Siegl and Ehrlich [38] define the 3D transformation matrix in equation (19) where α is the wind angle of the composite measured with respect to the length of the tube. A hoop-wound sample would have $\alpha = 90^\circ$, while a tube where the fiber run parallel to the axis of the tube have a wind angle of $\alpha = 0^\circ$.

$$[T]_{3D} = \begin{bmatrix} \cos^2 \alpha & \sin^2 \alpha & 0 & 0 & 0 & 2 \sin \alpha \cos \alpha \\ \sin^2 \alpha & \cos^2 \alpha & 0 & 0 & 0 & -2 \sin \alpha \cos \alpha \\ 0 & 0 & 1 & 0 & 0 & 0 \\ 0 & 0 & 0 & \cos \alpha & -\sin \alpha & 0 \\ 0 & 0 & 0 & \sin \alpha & \cos \alpha & 0 \\ -\sin \alpha \cos \alpha & \sin \alpha \cos \alpha & 0 & 0 & 0 & \cos^2 \alpha - \sin^2 \alpha \end{bmatrix} \quad (19)$$

Applying the transformation as seen in equation (20) gives a transformed compliance matrix. This matrix is applied for any wind angle α as seen in equation (21).

$$[\bar{S}] = [T]^T_{3D} [S] [T]_{3D} \quad (20)$$

$$\{\varepsilon\}_{\bar{z}\theta r} = [\bar{S}]\{\sigma\}_{\bar{z}\theta r} \quad (21)$$

However, the strain and stress tensors seen in equation (22) are not in the traditional order for cylindrical coordinates. Typically, the r coordinate is first, followed by the θ , then the z [38]. To re-order the entries in the transformed compliance matrix, the permutation matrix seen in equation (23) is introduced.

$$\begin{Bmatrix} \varepsilon_{\bar{z}} \\ \varepsilon_{\theta} \\ \varepsilon_r \\ \gamma_{\theta r} \\ \gamma_{\bar{z}r} \\ \gamma_{\bar{z}\theta} \end{Bmatrix} = \begin{bmatrix} \bar{S}_{11} & \bar{S}_{12} & \bar{S}_{13} & 0 & 0 & \bar{S}_{16} \\ \bar{S}_{12} & \bar{S}_{22} & \bar{S}_{23} & 0 & 0 & \bar{S}_{26} \\ \bar{S}_{13} & \bar{S}_{23} & \bar{S}_{33} & 0 & 0 & \bar{S}_{36} \\ 0 & 0 & 0 & \bar{S}_{44} & \bar{S}_{45} & 0 \\ 0 & 0 & 0 & \bar{S}_{45} & \bar{S}_{55} & 0 \\ \bar{S}_{16} & \bar{S}_{26} & \bar{S}_{36} & 0 & 0 & \bar{S}_{66} \end{bmatrix} \begin{Bmatrix} \sigma_{\bar{z}} \\ \sigma_{\theta} \\ \sigma_r \\ \tau_{\theta r} \\ \tau_{\bar{z}r} \\ \tau_{\bar{z}\theta} \end{Bmatrix} \quad (22)$$

$$[P] = \begin{bmatrix} 0 & 0 & 1 & 0 & 0 & 0 \\ 0 & 1 & 0 & 0 & 0 & 0 \\ 1 & 0 & 0 & 0 & 0 & 0 \\ 0 & 0 & 0 & 0 & 0 & 1 \\ 0 & 0 & 0 & 0 & 1 & 0 \\ 0 & 0 & 0 & 1 & 0 & 0 \end{bmatrix} \quad (23)$$

The permutation matrix is applied according to equation (24), resulting in the compliance matrix in cylindrical coordinates $[\bar{L}]$. The definitions for $[\bar{L}]$ can be seen in equations (25) and (26). This compliance matrix cylindrical coordinates $[\bar{L}]$ now described the mechanical properties in the radial, circumferential, and axial direction.

$$[\bar{L}] = [P][\bar{S}][P] \quad (24)$$

$$\begin{Bmatrix} \varepsilon_r \\ \varepsilon_\theta \\ \varepsilon_z \\ \gamma_{\theta z} \\ \gamma_{rz} \\ \gamma_{r\theta} \end{Bmatrix} = \begin{bmatrix} \overline{L}_{11} & \overline{L}_{12} & \overline{L}_{13} & \overline{L}_{14} & 0 & 0 \\ \overline{L}_{12} & \overline{L}_{22} & \overline{L}_{23} & \overline{L}_{24} & 0 & 0 \\ \overline{L}_{13} & \overline{L}_{23} & \overline{L}_{33} & \overline{L}_{34} & 0 & 0 \\ \overline{L}_{14} & \overline{L}_{24} & \overline{L}_{34} & \overline{L}_{44} & 0 & 0 \\ 0 & 0 & 0 & 0 & \overline{L}_{55} & \overline{L}_{56} \\ 0 & 0 & 0 & 0 & \overline{L}_{56} & \overline{L}_{66} \end{bmatrix} \begin{Bmatrix} \sigma_r \\ \sigma_\theta \\ \sigma_z \\ \tau_{\theta z} \\ \tau_{rz} \\ \tau_{r\theta} \end{Bmatrix} \quad (25)$$

$$\{\varepsilon\}_{cyl} = [\overline{L}]\{\sigma\}_{cyl} \quad (26)$$

6.2.2 Stress equilibrium in cylindrical coordinates

Assuming that the rings are elastic and deforming under plane stress conditions, the radial, circumferential, and axial strains can be defined by equations (27), (28), and (29) respectively [37], where u_r described the displacement in the radial direction and u_z is the displacement in the transverse direction.

$$\varepsilon_r = \frac{\partial u_r}{\partial r} \quad (27)$$

$$\varepsilon_\theta = \frac{u_r}{r} \quad (28)$$

$$\varepsilon_z = \frac{\partial u_z}{\partial z} \quad (29)$$

From equation (25), it is possible to rewrite the radial and circumferential strains in terms of their stresses, shown in equations (30) and (31). In this case, there is assumed to be no variation in temperature [37].

$$\varepsilon_r = \overline{L}_{11}\sigma_r + \overline{L}_{12}\sigma_\theta \quad (30)$$

$$\varepsilon_\theta = \overline{L}_{12}\sigma_r + \overline{L}_{22}\sigma_\theta \quad (31)$$

Conversely, isolating for the radial and circumferential stresses and substituting these equations in equations (27) and (28) provides equations for the radial and circumferential stress in terms of radial displacement seen in equations (32) and (33).

$$\sigma_r = \left(\frac{\overline{L}_{22}}{\overline{L}_{22}\overline{L}_{11} - \overline{L}_{12}^2} \right) \left(\frac{\partial u_r}{\partial r} - \frac{\overline{L}_{12}}{\overline{L}_{22}} \frac{u_r}{r} \right) \quad (32)$$

$$\sigma_{\theta} = \left(\frac{\overline{L_{11}}}{L_{22}\overline{L_{11}} - \overline{L_{12}}^2} \right) \left(\frac{u_r}{r} - \frac{\overline{L_{12}}}{\overline{L_{11}}} \frac{\partial u_r}{\partial r} \right) \quad (33)$$

The equilibrium equations in the radial and circumferential direction is represented by equation (34) [37], [41].

$$\frac{d\sigma_r}{dr} + \frac{\sigma_r - \sigma_{\theta}}{r} = 0 \quad (34)$$

Substituting equations (32) and (33) into equation (34) provides the ordinary differential equation (ODE) seen in equation (35) [37]. This equation is a Cauchy-Euler equation with a known solution [117].

$$r^2 \frac{d^2 u_r}{dr^2} + \frac{du_r}{dr} r + \left(-\frac{\overline{L_{11}}}{\overline{L_{22}}} \right) u_r = 0 \quad (35)$$

Equation (35) is rewritten into equation (36) for MATLAB's symbolic solver [118].

$$\frac{d^2 u_r}{dr^2} = \left(\frac{\overline{L_{11}}}{\overline{L_{22}}} \right) \frac{u_r}{r^2} - \frac{du_r}{dr} \frac{1}{r} \quad (36)$$

The homogenous solution for this Cauchy-Euler equation can be seen in equation (37), where A and B are constants [37]. The exponent k is defined in equation (38) and is the ratio of the properties in the radial and circumferential direction. Given that there is no temperature variation, the particular solution in terms of temperature is not necessary [37]. With the variation in temperature equal to zero, the entire term would also be zero.

$$u_r = Ar^k + Br^{-k} \quad (37)$$

$$k = \sqrt{\frac{\overline{L_{11}}}{\overline{L_{22}}}} \quad (38)$$

Substituting the ODE solution into the original expressions for radial and circumferential strain in equations (27) and (28) provides equations for the radial and circumferential strains as a function of the sample's radius [37]. These can be seen in equations (39) and (40).

$$\varepsilon_r = Ak r^{k-1} - Bk r^{-k-1} \quad (39)$$

$$\varepsilon_{\theta} = Ar^{k-1} + Br^{-k-1} \quad (40)$$

The expressions for radial and circumferential stress can be seen in equations (41) and (42) [37]. These are calculated by substituting equations (37) into equations (32) and (33).

$$\sigma_r = \left(\frac{\overline{L_{22}}}{\overline{L_{22}}\overline{L_{11}} - \overline{L_{12}}^2} \right) \left[\left(k - \frac{\overline{L_{12}}}{\overline{L_{22}}} \right) Ar^{k-1} + \left(-k - \frac{\overline{L_{12}}}{\overline{L_{22}}} \right) Br^{-k-1} \right] \quad (41)$$

$$\sigma_\theta = \left(\frac{\overline{L_{11}}}{\overline{L_{22}}\overline{L_{11}} - \overline{L_{12}}^2} \right) \left[\left(1 - k \frac{\overline{L_{12}}}{\overline{L_{11}}} \right) Ar^{k-1} + \left(1 + k \frac{\overline{L_{12}}}{\overline{L_{11}}} \right) Br^{-k-1} \right] \quad (42)$$

6.3 Approach for hoop-wound samples

For the hoop-wound samples, the thin shell approach in cylindrical coordinates presented in 6.2 was selected. Given that these samples only sprung inwards, circumferential and radial coordinates were sufficient to describe all of the samples' movements. There was no movement along the length of the cylinder, and so an axial component is not necessary.

6.3.1 Sample calculations

This solution is for the second in-situ consolidated hoop-wound sample. It was calculated using MATLAB's symbolic ODE solver [118]. This sample had a strain on its inner and outer surfaces of $-213\mu\epsilon$ and $331\mu\epsilon$ respectively in the circumferential direction. The ODE describing the radial displacement can be seen in equation (43), where the coefficient is the ratio of the circumferential and the radial properties. The homogeneous solution to this ODE can be seen in equation (44). As expected, the exponents are the positive and negative roots of the coefficient. To generate this solution, 2 initial conditions were necessary. These initial conditions were taken to be known strains at the inner and outer surfaces of the sample. Given that there was no change in the material properties throughout the thickness of the sample, the same solution is valid over the entire range of radii. This satisfies the condition that the displacements and stresses be continuous at each plie interface [37], [42], [45], [64].

$$\frac{d^2 u_r}{dr^2} = (13.3981) \frac{u_r}{r^2} - \frac{du_r}{dr} \frac{1}{r} \quad (43)$$

$$u_r = 17.624 r^{3.660} - 2.118 \times 10^{-10} r^{-3.660} \quad (44)$$

From this solution and equations (41) and (42), the radial and circumferential stresses can be calculated as seen in equations (45) and (46).

$$\sigma_r = 723.791 r^{2.660} + 7.3801 \times 10^{-9} r^{-4.660} \quad (45)$$

$$\sigma_\theta = 2649.32 r^{2.660} - 2.7014 \times 10^{-8} r^{-4.660} \quad (46)$$

6.3.2 Result

The methodology presented in the sample calculation was then extended to all the hoop-wound samples. There were 2 successful trials per heat treatment, their results can be seen in Table 30. There were 2 trials (sample 1 in-situ and sample 1 annealed) presented in Table 23 that only had strain results for the inner surfaces. Calculations could not be performed on those samples because strain measurements on both the inner and outer surfaces was necessary to solve the equations presented in this chapter. Table 30 contains the circumferential and radial stresses which were calculated from the measured circumferential strains. It also presents an average circumferential strain for each heat treatment to serve as a comparison.

Table 30: Circumferential and radial stresses for the outer and inner surfaces of the hoop-wound samples calculated using stress from strain calculations from Chapter 6

		In-Situ				In-situ	
		Sample 2		Sample 3		Average	
		Inner	Outer	Inner	Outer		
Strain (μm)		-213	331	-372	409	Circumferential stress (MPa)	
Stress (MPa)	Circum.	14.298	88.281	11.175	117.29	Inner	Outer
	Radial	145.64	142.01	208.37	202.82	12.74	102.79
		Annealed				Annealed	
		Sample 2		Sample 3		Average	
		Inner	Outer	Inner	Outer		
Strain (μm)		-328	301	-363	403	Circumferential stress (MPa)	
Stress (MPa)	Circum.	4.9877	90.406	11.222	115.3	Inner	Outer
	Radial	167.51	162.89	204.39	198.95	8.10	102.85

Figure 69 shows the circumferential strain distribution throughout the thickness of all the hoop-wound samples calculated as thin cylindrical shells. Note that the legend refers to the heat treatment of the sample (either annealed or in-situ consolidated), and the number (2 or 3) refers to the sample number seen in Table 23 and Table 30. The midplane of the laminate is indicated by a black vertical line. The x-axis represents the position throughout the laminate's thickness, with a radius of 0.03175m being the inner radius and 0.03303m being the outer radius of the laminate. Over a small scale, this variation in strain appears to be linear and near zero at the midplane. The strain functions are exponential functions, but when plotted over such a small range of radii, the behavior appears to be linear. Most of the samples have a strain near zero at their midplane, which would indicate that the laminates are primarily subjected to a bending load rather than a tensile load. It is very similar to what CLT would calculate for a strain distribution given that Kirchhoff's principal assumes a linear strain distribution throughout the sample [22].

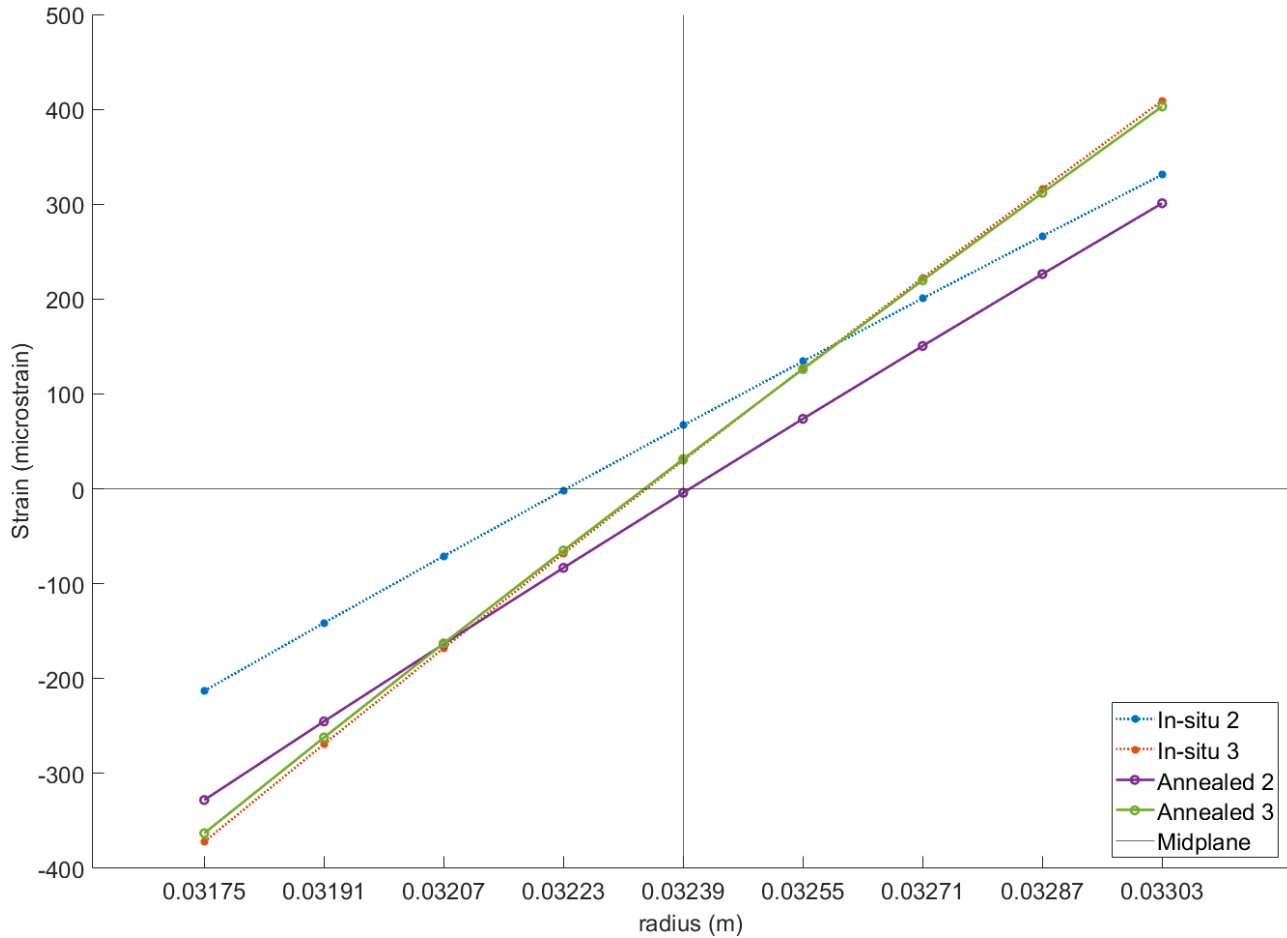


Figure 69: Circumferential strain distribution for the in-situ and annealed hoop-wound samples calculated in cylindrical coordinates

Figure 70 shows the circumferential stress for the same samples calculated in cylindrical coordinates. This graph shows a small tensile stress on the inner surface that increases linearly throughout the sample towards the outer layer. Given that the samples sprung inwards, a tensile residual stress in the circumferential direction was expected. The radials stresses in each sample can be seen in Figure 71. They are roughly constant throughout the thickness.

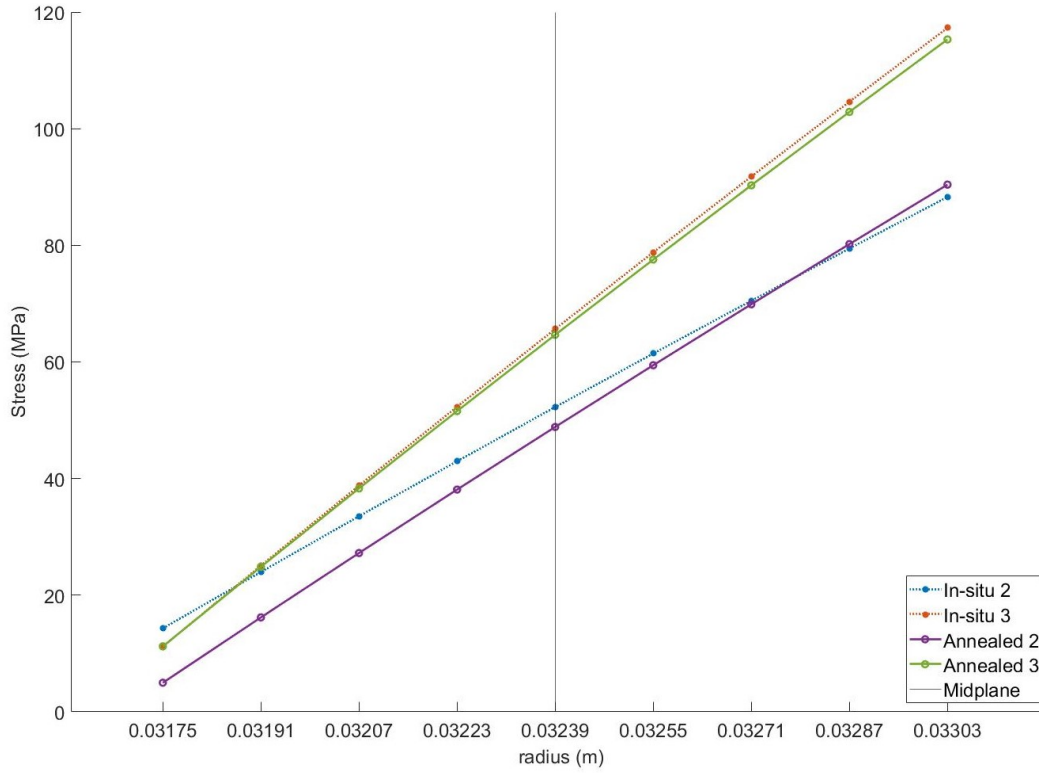


Figure 70: Circumferential stress distribution for the in-situ and annealed hoop-wound samples calculated in cylindrical coordinates

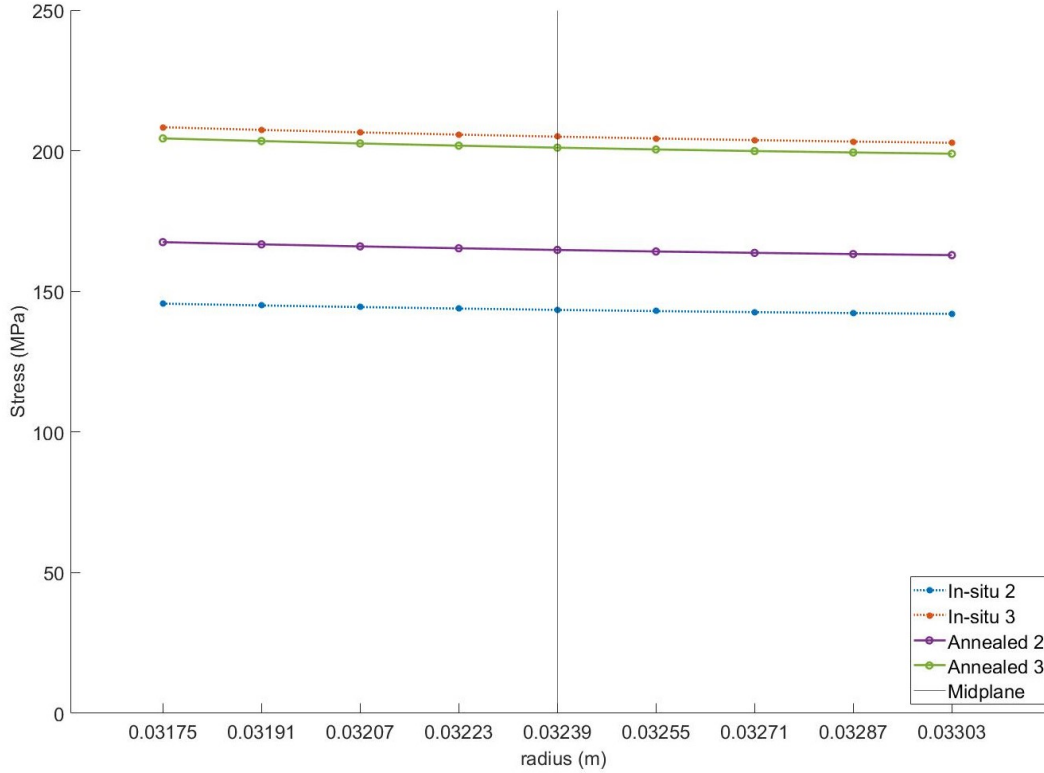


Figure 71: Radial stress distribution for the in-situ and annealed hoop-wound samples calculated in cylindrical coordinates

6.4 Approach for asymmetric samples

The thin cylindrical shell approach assumes no stress in the axial direction. Given that all the asymmetric sample twisted when cut, this approach would not be sufficient to describe their stress state. Assuming that there was no axial displacement would be an oversimplification. The CLT approach was instead used for the $[90_4, 45_4]_T$ and $[45_4, 90_4]_T$ samples since it accounts for movement in the axial (x-axis) and circumferential (y-axis) directions as shown previously in Figure 67. It assumes no strain through the samples' thickness [22]. These conditions best describe the observed deformation.

6.4.1 Sample calculations

The first step in this procedure is to calculate the strain distribution throughout the thickness of the samples. The strains in the x and y directions (ϵ_x, ϵ_y) were measured on the inner and outer surfaces of each sample using rectangular rosettes. The plane shear (γ_{xy}) on the surfaces of the samples was calculated knowing $\gamma_{xy} = \epsilon_x - \epsilon_y$ since the strain gages were 90° apart on the rosette [116]. The strain at each layer interface could then be calculated using linear interpolation, since Kirchhoff's hypothesis states the strain distribution is linear throughout the thickness [22]. The strain calculated at the midplane is taken to be the midplane strain vector $\{\epsilon^0\}$. To calculate the curvature, the midplane strain must be subtracted from the strain at the interface and then divided by the interface's position (z) with respect to the neutral axis. As expected, this provides a constant curvature throughout the sample. A breakdown of these calculations can be seen in Table 31 for the first of the annealed $[45_4, 90_4]_T$ samples. The blue cells are measured strain values, while the remaining values are calculated.

Table 31: Strain distribution for annealed $[45_4, 90_4]_T$ sample 1

Ply	z (m)	Strain ($\mu\epsilon$)			Curvature ($\mu\epsilon/\text{mm}$)		
		ϵ_x	ϵ_y	γ_{xy}	κ_x	κ_y	κ_{xy}
Inner	-6.40E-04	-1083	-1011	-72	1220	1057	163
	-4.80E-04	-888	-842	-46	1220	1057	163
	-3.20E-04	-693	-673	-20	1220	1057	163
	-1.60E-04	-497	-504	6	1220	1057	163
Midplane	0	-302	-334	32			
	1.60E-04	-107	-165	59	1220	1057	163
	3.20E-04	89	4	85	1220	1057	163
	4.80E-04	284	173	111	1220	1057	163
Outer	6.40E-04	479	342	137	1220	1057	163

Table 32: $[ABD]$ matrix for $[45_4, 90_4]_T$ laminates

[A] GPa·m	3.32E-02	2.28E-02	2.08E-02	-7.04E-06	-6.28E-06	-6.66E-06	[B] GPa·m ²
	2.28E-02	1.16E-01	2.08E-02	-6.28E-06	1.96E-05	-6.66E-06	
	2.08E-02	2.08E-02	2.60E-02	-6.66E-06	-6.66E-06	-6.28E-06	
[B] GPa·m ²	-7.04E-06	-6.28E-06	-6.66E-06	4.53E-09	3.11E-09	2.84E-09	[D] GPa·m ³
	-6.28E-06	1.96E-05	-6.66E-06	3.11E-09	1.59E-08	2.84E-09	
	-6.66E-06	-6.66E-06	-6.28E-06	2.84E-09	2.84E-09	3.55E-09	

From the midplane strain and sample curvature, it is then possible to calculate the force and moment resultant from the sample's ABD matrix. The ABD matrix for the $[45_4, 90_4]_T$ layup can be seen in Table 32.

6.4.2 Results

Like with the hoop-wound samples, the strain distribution in the symmetric samples is linear. The circumferential strain distributions were calculated using both CLT and the thin cylindrical shells approach, they provide almost identical results. The circumferential strain distribution for the in-situ consolidated and the annealed samples with the $[90_4, 45_4]_T$ layup can be seen in Figure 72. Given that these samples spring out, it was expected that the inner surface of the samples would be under tension, while the outer would be under compression. Like with the hoop-wound samples, there does not appear to be a distinction between the strain behavior of the annealed and the in-situ samples. The same can be said for the $[45_4, 90_4]_T$ samples, which can be seen in Figure 73. The inner surface of these samples is under compression, while the outer ones are under tension, like the hoop-wound samples. This was expected, given that these samples all sprung inwards. Much like the strain distributions in the previous figures, the circumferential stress distributions do not highlight a significant difference between the heat treatments.

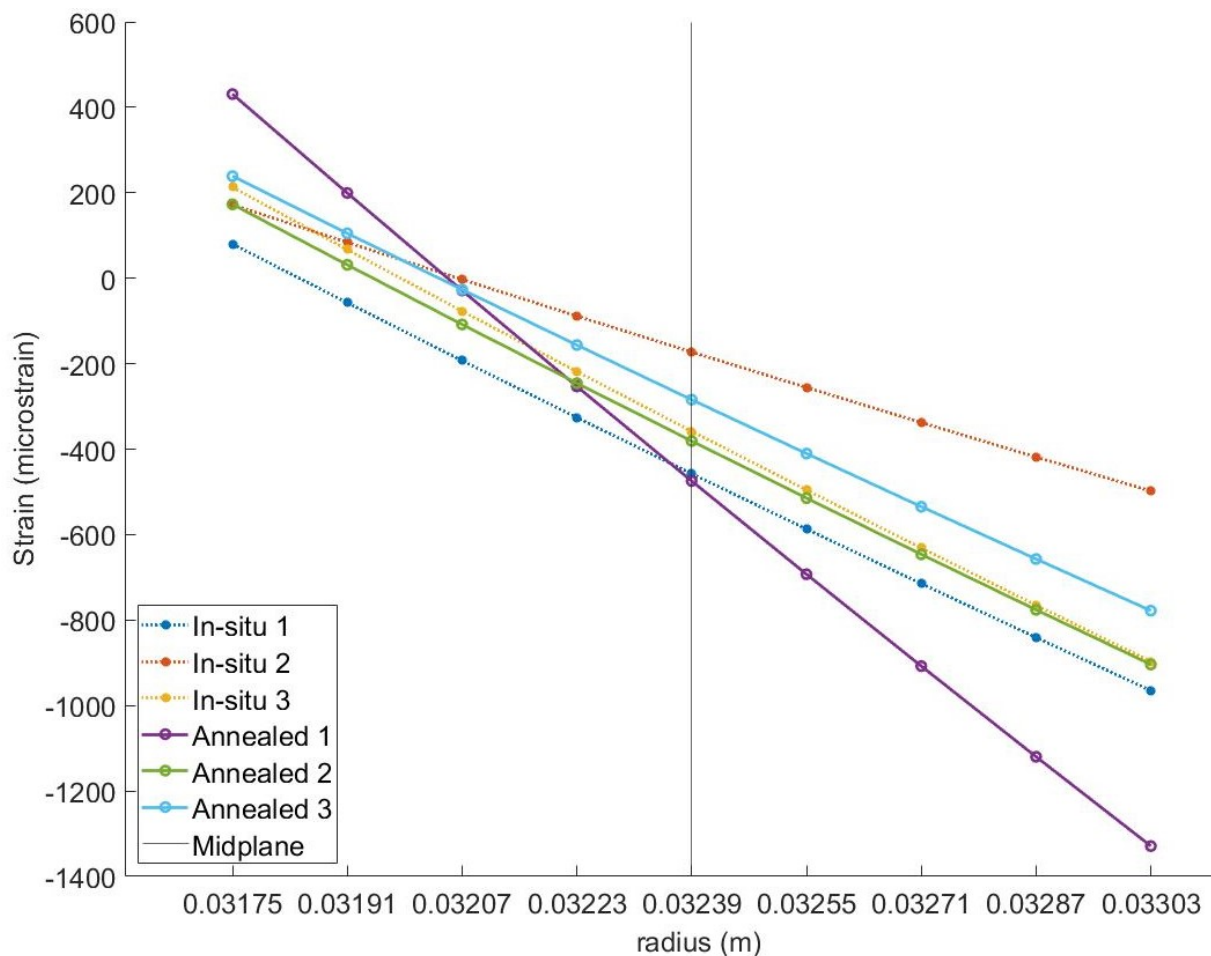


Figure 72: Circumferential strain distribution for in-situ and annealed $[90_4, 45_4]_T$ samples

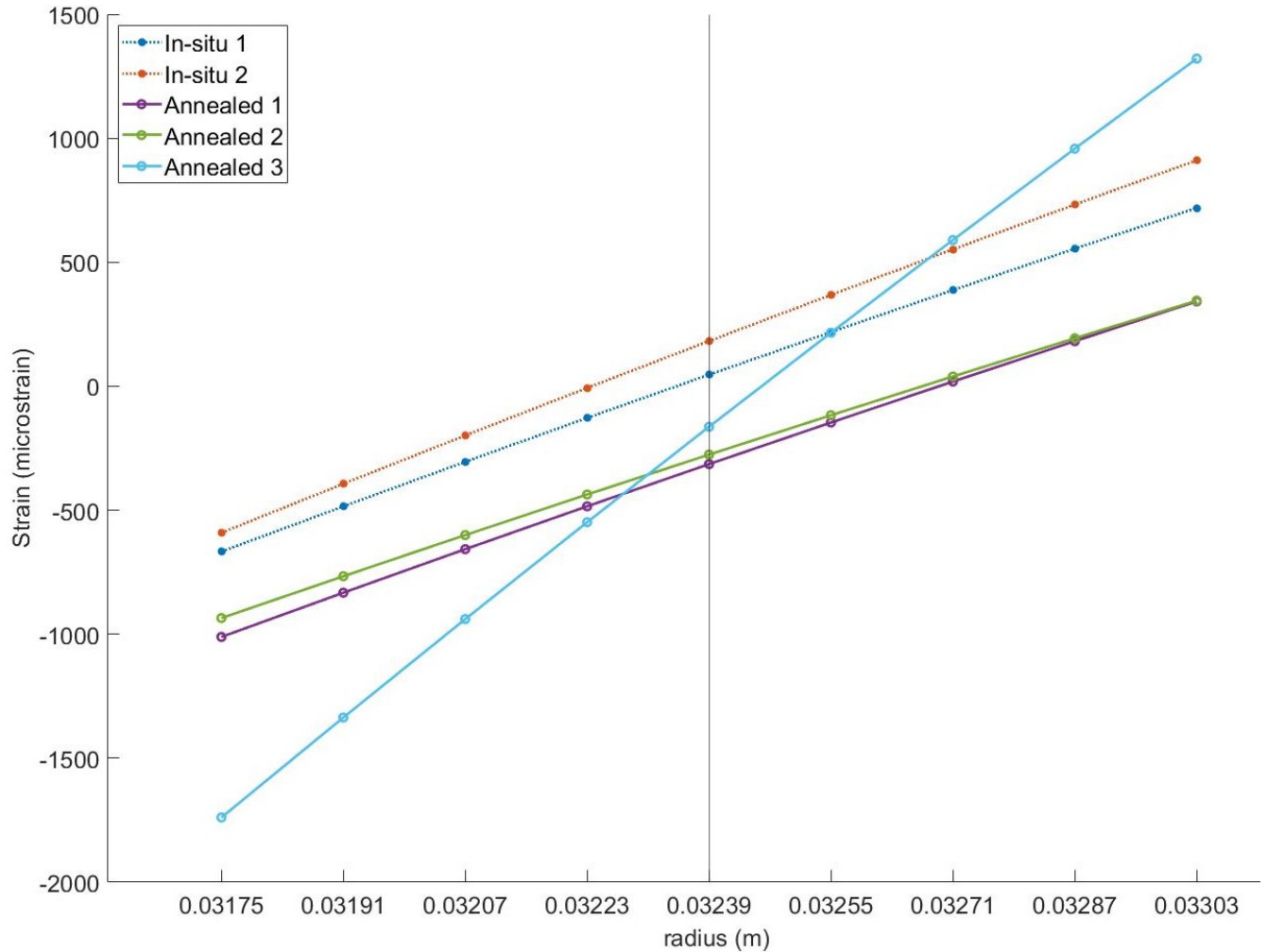


Figure 73: Circumferential strain distribution for in-situ and annealed $[45_4, 90_4]_T$ samples

Given that there is unfortunately any distinct clustering of the in-situ consolidated samples and the annealed samples in the strain data, the next step in this analysis was to calculate the force and moment resultants for each laminate. The results for the $[90_4, 45_4]_T$ samples can be seen in Table 33, while the results for the $[45_4, 90_4]_T$ samples are in Table 34. The tables show the data for each sample within their respective heat treatment. The strains on the inner and outer surfaces (ϵ_x, ϵ_y) was measured using the rectangular rosettes, while the midplane strain, sample curvature, force resultant, and moment resultant were subsequently calculated from these values using the procedure highlighted in the previous section. The cells containing measured quantities are highlighted in blue. The average force and moment resultant was also calculated for each heat treatment.

Table 33: Midplane strain and curvature used to calculate the force and moment resultants for the $[90_4, 45_4]_T$ samples

	Strain ($\mu\epsilon$)			Curvature ($\mu\epsilon/\text{mm}$)	Force Resultant (N/mm)	Moment Resultant (Nm/m)	Average Resultants (N/mm, Nm/m)					
	Inner Surface	Midplane ϵ_0	Outer Surface				N_x	N_y				
In-Situ	Sample 1						N_x	-5136				
	ϵ_x	126	74	23	κ_x	-80	N_x	2366	M_x	377	N_y	-14939
	ϵ_y	80	-443	-965	κ_y	-816	N_y	-18668	M_y	1445	N_{xy}	-2897
	γ_{xy}	46	517	988	κ_{xy}	736	N_{xy}	4446	M_{xy}	863		
	Sample 2						M_x	-1678				
	ϵ_x	-37	-189	-341	κ_x	-238	N_x	-13577	M_x	-4417	M_y	-2724
	ϵ_y	172	-163	-498	κ_y	-523	N_y	-13148	M_y	-6411	M_{xy}	-1053
	γ_{xy}	-209	-26	157	κ_{xy}	286	N_{xy}	-11270	M_{xy}	-3652		
	Sample 3											
	ϵ_x	-91	-77	-63	κ_x	22	N_x	-4197	M_x	-995		
	ϵ_y	213	-342	-897	κ_y	-867	N_y	-13002	M_y	-3207		
	γ_{xy}	-304	265	834	κ_{xy}	889	N_{xy}	-1867	M_{xy}	-368		
	Strain ($\mu\epsilon$)			Curvature ($\mu\epsilon/\text{mm}$)	Force Resultant (N/mm)	Moment Resultant (Nm/m)	Average Resultants (N/mm, Nm/m)					
	Inner Surface	Midplane ϵ_0	Outer Surface				N_x	N_y				
Annealed	Sample 1						N_x	-7549				
	ϵ_x	-333	-111	111	κ_x	347	N_x	-1598	M_x	841	N_y	-13861
	ϵ_y	431	-449	-1329	κ_y	-1375	N_y	-7178	M_y	-5534	N_{xy}	-4668
	γ_{xy}	-764	338	1440	κ_{xy}	1722	N_{xy}	1110	M_{xy}	1591		
	Sample 2						M_x	-1622				
	ϵ_x	-186	-166	-145	κ_x	32	N_x	-8891	M_x	-2116	M_y	-5113
	ϵ_y	173	-366	-904	κ_y	-841	N_y	-19649	M_y	-3338	M_{xy}	-881
	γ_{xy}	-359	200	759	κ_{xy}	873	N_{xy}	-5748	M_{xy}	-1475		
	Sample 3											
	ϵ_x	-117	-192	-266	κ_x	-116	N_x	-12158	M_x	-3590		
	ϵ_y	239	-270	-778	κ_y	-795	N_y	-14755	M_y	-6466		
	γ_{xy}	-356	78	512	κ_{xy}	678	N_{xy}	-9368	M_{xy}	-2758		

Table 34: Midplane strain and curvature used to calculate the force and moment resultants for the $[45_4, 90_4]_T$ samples

	Strain ($\mu\epsilon$)			Curvature ($\mu\epsilon/\text{mm}$)	Force Resultant (N/mm)	Moment Resultant (Nm/m)	Average Resultants (N/mm, Nm/m)					
	Inner Surface	Midplane ϵ_0	Outer Surface				N_x	N_y				
In-Situ	Sample 1						N_x	-37154				
	ϵ_x	-918	-544	-170	κ_x	584	N_x	-36913	M_x	12056	N_y	7300
	ϵ_y	-667	26	719	κ_y	1083	N_y	-346	M_y	25329	N_{xy}	-34077
	γ_{xy}	-251	-570	-889	κ_{xy}	-498	N_{xy}	-33578	M_{xy}	9992		
	Sample 2						M_x	11438				
	ϵ_x	-783	-657	-530	κ_x	198	N_x	-37395	M_x	10820	M_y	27257
	ϵ_y	-591	160	911	κ_y	1173	N_y	14946	M_y	29185	M_{xy}	9426
	γ_{xy}	-192	-817	-1441	κ_{xy}	-976	N_{xy}	-34577	M_{xy}	8860		
	Strain ($\mu\epsilon$)			Curvature ($\mu\epsilon/\text{mm}$)	Force Resultant (N/mm)	Moment Resultant (Nm/m)	Average Resultants (N/mm, Nm/m)					
	Inner Surface	Midplane ϵ_0	Outer Surface				N_x	N_y				
Annealed	Sample 1						N_x	-24736				
	ϵ_x	-1083	-302	479	κ_x	1220	N_x	-33269	M_x	13286	N_y	-8902
	ϵ_y	-1011	-334	342	κ_y	1057	N_y	-33172	M_y	16181	N_{xy}	-21205
	γ_{xy}	-72	32	137	κ_{xy}	163	N_{xy}	-28583	M_{xy}	11082		
	Sample 2						M_x	8900				
	ϵ_x	-580	-159	263	κ_x	659	N_x	-17773	M_x	7180	M_y	19540
	ϵ_y	-935	-295	345	κ_y	1000	N_y	-17375	M_y	11276	M_{xy}	6843
	γ_{xy}	355	137	-82	κ_{xy}	-341	N_{xy}	-14782	M_{xy}	5660		
	Sample 3											
	ϵ_x	-406	-459	-513	κ_x	-84	N_x	-23166	M_x	6234		
ϵ_y	-1739	-209	1321	κ_y	2391	N_y	23841	M_y	31165			
γ_{xy}	1333	-250	-1834	κ_{xy}	-2474	N_{xy}	-20250	M_{xy}	3786			

Chapter 7: Discussion

7.1 Sample characterization

When making composite laminates, characterizing their crystallinity, fiber volume fraction, and void content is a crucial step in validating the manufacturing process and the processing parameters. These properties can all have impacts on the laminate strength and so are of particular interest. Given that the goal of this experiment was to investigate the applications of annealing for composite materials, comparing the laminate properties before and after heat treatment is a necessary step in validating the process. If any of these properties suffer with annealing, the applications for this process would be limited.

Crystallinity is often measured in conjunction with other mechanical and thermal properties because it can impact laminate level properties like failure behavior [59], interlaminar shear stress [56] and interfacial shear strength [58]. Cooling rate [49], [58], [59], [61] and annealing temperature [57] are known to impact crystallinity. Some research groups have recorded crystallinity values as high as 33% when cooling at a rate of 1°C/min [58] and 35.9% when consolidating samples in an autoclave [111]. These values will serve as a target value for fully crystalline samples.

The crystallinity of the samples increased steadily with each manufacturing step. The tape, as received from the supplier, only had an average crystallinity of 8%. The in-situ manufactured samples that received no additional heat treatment had an average crystallinity of 20%. The samples that were annealed at 200°C had an average crystallinity of 27%. The standard deviations of the crystallinity for the in-situ consolidated and annealed samples are of 4% and 5% respectively, which are relatively high. This is because these averages contain crystallinity measurements for all three layups and the layups were not all equally crystalline. If instead each layup was isolated, then the standard deviation drops, and another interesting trend becomes noticeable. The hoop wound samples had the highest initial crystallinity at 23% (standard deviation of 1%) and it increased marginally to 25% (standard deviation of 2%). Given these standard deviation values, this increase is not statistically significant.

The asymmetric layups tell a different story. The $[90_4, 45_4]_T$ samples had an in-situ crystallinity of 16% (standard deviation of 4%) and an annealed crystallinity of 33% (standard deviation of 2%). The $[45_4, 90_4]_T$ samples showed a similar increase from 19% to 23% with annealing and with standard deviations of 0% and 2% respectively. In both cases, these are large and statistically significant increases. The asymmetric samples showed significant improvement to their crystallinities with annealing, while the hoop wound samples did not. This explains how the average crystallinity increased overall despite having such a large standard deviation.

There are two interesting things to remark about the in-situ consolidated samples. None of the in-situ consolidated hoop-wound samples produced a cold crystallization peak, while all the asymmetric in-situ samples had very low crystallinity and produced significant cold crystallization peaks during the initial heating by the DSC. Additionally, the hoop-wound samples had a higher average crystallinity than the asymmetric ones. One reason for this may be that the 90° layers were wound continuously without the AFP head lifting from the mandrel, while the 45° layers were laid down 1 band at a time. This means that once a tow had been wrapped around the mandrel, it needed to be cut and the head repositioned before the next band could be laid down. This additional movement meant that the bi-directional samples were heated

less uniformly than the hoop-wound ones and could potentially explain why the samples containing 45° layers showed lower in-situ crystallinity.

The average crystallinity recorded here was not as high as some other heat treatment experiments [58], [111]. In order to achieve higher degree of crystallinity, a slower cooling rate may have been necessary [58]. Regardless, the annealing time and temperature were sufficient for the samples to have fully crystallized and not produce a cold crystallization peak.

The average fiber volume fraction for the in-situ consolidated samples was 50.68% and the annealed samples was 49.49%. They have standard deviations of 2.55% and 2.96% respectively. These averages are within 1.19% of each other, which is smaller than both their standard deviation values. This difference is not statistically significant difference. This would indicate that the heat treatment did not have an impact on the fiber volume fraction, which was expected given that no compaction was used nor was any resin added during annealing. The fiber volume fraction measured using micrographs is dependent on many things, including the image quality, image focus, selected threshold, and which region of the photo is selected. All of these factors explain the small amount of spread in the data. However, given the large number of photos treated, the data is fairly consistent.

The average fiber volume fractions of 50.68% and 49.49% for the in-situ consolidated and annealed samples were somewhat lower than expected, considering that the laminate properties in the manufacturer datasheets is given for typical laminates with a 60% fiber volume fraction [77], [95]. To attempt to figure out why this was the case, the unprocessed tape from the manufacturer was also characterized. The tape was found to have a fiber volume fraction of 50.32%, which is between the values measured for the in-situ consolidated and annealed laminates. This would indicate that the low fiber volume fraction was a consequence of the tape quality, rather than the manufacturing process. Micrographs of the tape showed uneven fiber distribution and resin rich pockets, which likely contributed to the low fiber volume fraction.

The void content of the in-situ and the annealed samples were of 0.78% and 0.60% respectively. Their standard deviations were of 0.67% and 0.38%. These are large standard deviations are possibly caused by the variations in laminate quality. Given these large standard deviations and the variability associated with image analysis, this is not considered to be a statistical difference. As expected, heat treatment did not impact the void content of the laminates. On average, the laminates met the target of having a void content of under 1%. In reality, in only 15 of the 66 images did samples have void contents above 1%, leaving the majority compliant with the standard [114]. None of the samples exceeded a void content of 5%. The highest void content was found to be 3.34% in a piece of tape.

To serve as a baseline, the void content of the composite tape was measured and found to be 0.45% on average and have a standard deviation of 0.74%. The reality is there was a large variation in the tape quality; the void contents varied from 0.05% to 3.34%. This is likely due to how thin the tape is, meaning that any defects represent a larger proportion of their surface area. Regardless, the majority of the tape samples would have been compliant with the 1% standard.

On average, the composite tape had a smaller void content than the laminates. Inter-ply voids and delamination could account for this difference, although the majority of the large voids appeared to be within the plies. One of the main difficulties when performing this kind of image

analysis is that scratches appear to be same colour of voids, and so they get included in the binary selection. Given that the laminates had a larger cross-sectional area than the tapes, the images were more likely to contain scratches, which could artificially inflate their void content. Given that the samples had an overall average void content less than 1%, this was not considered to be of concern.

Overall, the annealing procedure did not have a significant impact on the fiber volume fraction or the void content. This is encouraging, considering that these parameters are often tightly controlled in the aerospace industry [77], [95], [114]. The annealing did improve the crystallinity, although the cooling rate would likely need modifying to create samples with higher crystallinities.

7.2 Hoop-wound samples

There is no statistically significant difference between the strain recorded in the in-situ consolidated and the annealed samples. For this comparison, strain on the inner surfaces of the samples will be considered, since there are more datapoints. The in-sit consolidated samples had an average circumferential strain of $-278\mu\epsilon$ and a standard deviation of $68\mu\epsilon$. The annealed samples had an average circumferential strain of $-270\mu\epsilon$ with a standard deviation of $107\mu\epsilon$. There was significant spread in the measured strain values, leading to high standard deviations. These averages are extremely close, and considering the significant standard deviation for each group, are not statistically distinct from one another. This means that the annealing did not make a significant impact on the measured circumferential strains present within the samples. This null result can be explained by the fact that the fibers properties are dominant in the circumferential direction, while the annealing impacts the PEEK matrix.

When looking at the strain distribution in Figure 69 and the circumferential stress plotted in Figure 70, there is no obvious distinction or grouping between the annealed and the in-situ samples. There is no clustering within the sample groups. The average circumferential stresses calculated on the inner and the outer surfaces were of the in-situ consolidated samples were of 12.74MPa and 102.79 MPa respectively. For the annealed samples, these stresses were of 8.10MPa and 102.85MPa. There is no apparent difference between the residual stresses present in the annealed and the in-situ consolidated samples. These stresses are calculated from strain values that did not show any statistically significant difference, and so these close averages were expected.

It is somewhat surprising that the stress from strain calculations in cylindrical coordinates presented in Chapter 6 produce radial stress distributions that are constant. It is usually expected for the radial stress to be zero at the outer surfaces, and largest in the middle of the laminates [119]. This solution was attempted. Instead of using the strain on the inner and outer surfaces as boundary conditions, the strain on the inner surface and zero radial stress at the inner surface were used. The result can be seen in Figure 74. The strains at the outer surfaces does not approach the actual measured values, as if setting the additional boundary condition of the radial stress being 0 at the surface artificially stiffened the samples. For this reason, this set of boundary conditions was rejected.

The radii measured before and after cutting from Table 24 can also be used to gage the impact of annealing on the samples' deformation. On average, the outer radii of the in-situ consolidated samples decreased in radius by 1.363mm when the strain was full relieved. For the annealed samples, this decrease was of 0.176mm. This means that on average, the in-situ consolidated samples sprang in by 1.2mm more than the annealed ones. Unfortunately, although the measurements do show a consistent trend, a difference of 1.2mm is not statistically significant given that the radius measurements had an average standard deviation of 0.99mm for the in-situ samples and of 0.83mm for the annealed ones. This variation in the image analysis could be due to the angle between the sample and the camera when the photo was taken. It could also arise from the fact that the pixels used to compute the arcs were chosen manually. Even if it cannot be shown to be statistically significant for this number of samples, this trend could be explained by rigid body deformation, which is a translation or rotation of the sample, rather than a deformation of the sample [120]. Rigid body deformation is typically assumed to be zero in an elastic solution in cylindrical coordinates [41].

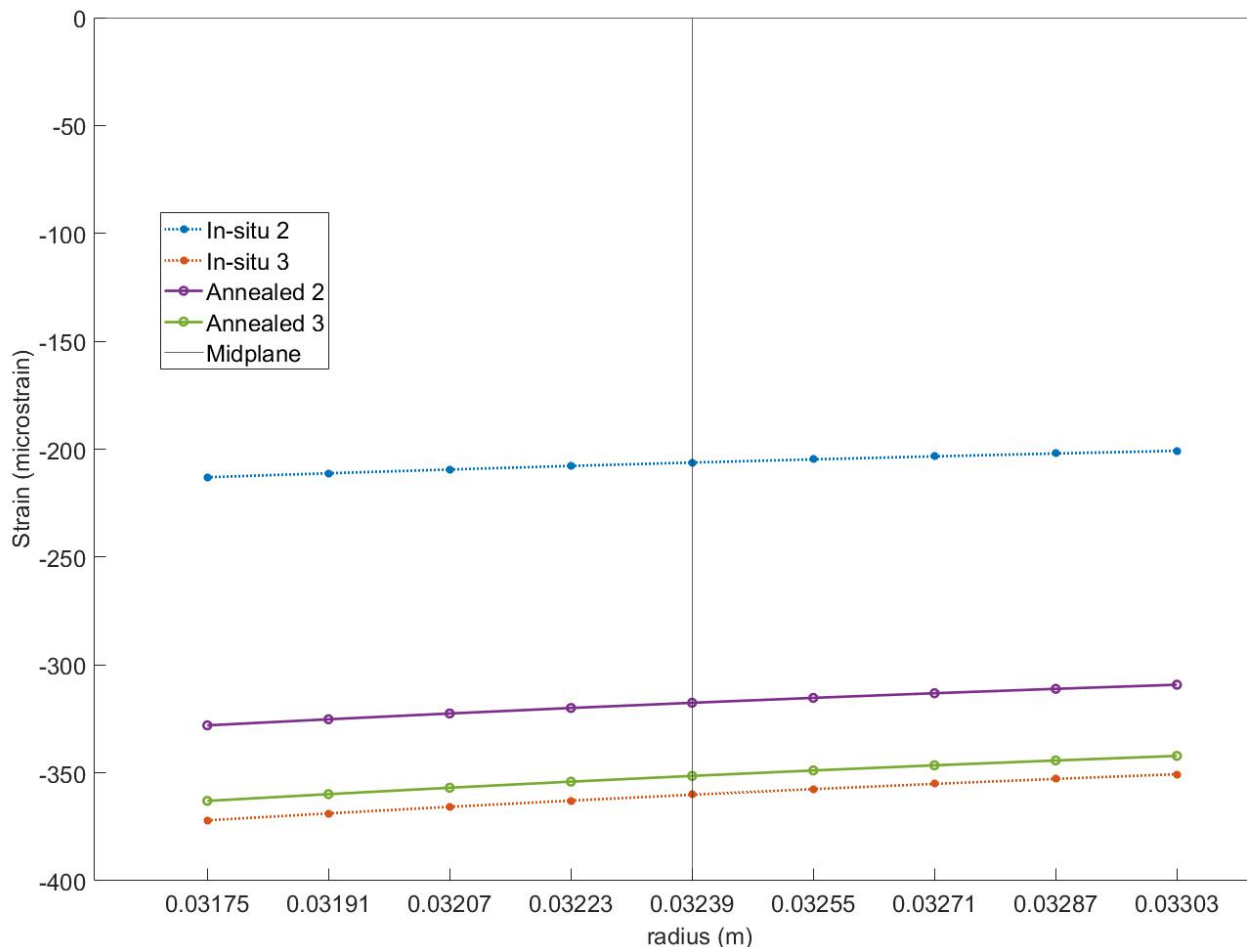


Figure 74: Circumferential strain distribution when radial stress at the inner surface is set to zero

Variations within the strain data can be explained by a variety of factors. The first is imperfect alignment between the fibers and the axis of the strain gages. Achieving perfect alignment in small, curved samples was difficult, even when using magnification. Another factor

was aligning the two cuts such that the center of the gap would be exactly opposite the center of the gage. The location of the cuts was measured and marked beforehand, but there was still variation due to the width of the cutting slot on the saw and the kerf of the blade. Finally, any imperfect gage adhesion or interference from that waterproof coating are equally possible.

7.3 Asymmetric samples

The $[90_4, 45_4]_T$ and $[45_4, 90_4]_T$ samples sprung out and sprung in respectively. They all twisted when cut, which was expected. There is a lot of spread in the recorded strain data, leading to high standard deviations. For the $[90_4, 45_4]_T$ samples, the recorded strain on the inner surfaces of the in-situ consolidated and the annealed samples were of $155\mu\epsilon$ and $281\mu\epsilon$. Their standard deviations are of $56\mu\epsilon$ and $109\mu\epsilon$ respectively, which shows significant overlap between these two groups. Similar overlap is noted on the outer surfaces of the samples. The $[45_4, 90_4]_T$ samples have even higher standard deviations. The strains recorded on the outer surfaces were of $469\mu\epsilon$ for the in-situ consolidated samples and of $669\mu\epsilon$ for the annealed samples. Their respective standard deviations were of $496\mu\epsilon$ and $461\mu\epsilon$. There is significant overlap in these calculated intervals, meaning that the difference between these averages is not statistically significant.

Much like the hoop-wound samples, they were assumed to have a linear variation in strain throughout their thickness. Their circumferential strain distributions can be seen in Figure 72 and Figure 73. When looking at these figures, there is no distinct clustering or grouping within the data that would indicate that the annealed samples had less residual circumferential strain. There is also significant spread in the strain data within each heat treatment. Unfortunately, like with the hoop-wound samples, the measured strain values and calculated stress values did not show a clear distinction between the annealed and the in-situ consolidated samples.

For the $[90_4, 45_4]_T$ samples, the average force and moment resultants were $(-5136, -14939, -2897)\text{N/mm}$ and $(-1678, -2724, -1053)\text{Nm/m}$ respectively for the in-situ consolidated samples and of $(-7549, -13861, -4668)\text{N/mm}$ and $(-1622, -5113, -881)\text{Nm/m}$ for the annealed samples. When comparing the force and moment resultants for these two different heat treatments, there does not appear to be a significant difference between these averages. Given that these resultants are calculated from strains that are not considered to be statistically significant, these values are also not considered to be statistically significant.

A similar result was found for the $[45_4, 90_4]_T$ samples. The in-situ samples had force and moment resultants of $(-37154, 7300, -34077)\text{N/mm}$ and $(11438, 27257, 9426)\text{Nm/m}$ respectively. The annealed samples had force and moment resultants of $(-24736, -8902, -21205)\text{N/mm}$ and $(8900, 19540, 6843)\text{Nm/m}$ for the laminates. Given the spread in the data and very close averages, there is no significant impact from the annealing on the laminate stresses for either of these asymmetric layups.

The lack of difference recorded in this experiment could indicate one of two things: either the strain measurements are not sufficiently precise to resolve a difference, or the annealing had no significant impact on the residual stresses of the samples comprised of 90° and 45° layers. Like with the hoop-wound samples, spread in the data was likely due to imperfections in the alignment and adhesion of the gages to the samples.

The radii of the samples after cutting could help to determine whether annealing impacted the deformation of the samples. For the samples with a $[90_4, 45_4]_T$ layup, the in-situ consolidated samples had an average increase in their outer radii by 3.4649mm. The annealed samples experienced an average increase of 3.1046mm for the outer radii. This means that on average, the annealed samples experienced approximately 0.36mm less spring out. This could indicate that the annealing relieved some residual stresses in the 45° layers reducing the overall spring out of the samples. While consistent, this result is not statistically significant because these in-situ and annealed radii measurements had an average standard deviation of 0.64mm and 0.68mm respectively. A possible reason for this standard deviation is that, due to the twisting motion, these samples did not lie in a single plane and parallax from the camera could have become a bigger issue.

The radii of the $[45_4, 90_4]_T$ samples tell a similar story. On average, the outer radii of the in-situ samples sprung in by 1.621mm, while the annealed samples sprung in by 2.4915mm. While it would appear as though the annealed samples sprung in by about 0.87mm more, this result is not statistically conclusive because the in-situ and annealed measurements had an average standard deviation of 0.65mm and 0.79mm. At this stage, it remains unclear as to whether the annealing had an impact on the residual strain of asymmetric samples. Neither optical nor strain measurements were able to make a statistical distinction.

Chapter 8: Conclusion

The goal of the project was to relieve the residual process stress and reduce the deformation from thermoplastic composite samples manufactured using AFP. A secondary goal was to achieve this without compromising some key laminate properties. Flat unidirectional samples served as a proof of concept when selecting annealing cycle parameters. Unwanted curvature perpendicular to the fiber direction could be largely removed from thin flat unidirectional samples using a 3h hold at 200°C with a vacuum bag pressure of 15 torr. These samples came within 2mm of flat. Method of heat application did not have a significant impact as long as the glass transition temperature was reached. This procedure worked best for eliminating residual process stresses perpendicular to the fiber direction. This kind of post-treatment may be sufficient, depending on the tolerances of the application. On the field corrections could also be done with a sufficiently powerful heat blanket. Despite having a longer hold time, the thin symmetric sample consisting of 90°, 0°, and ±45° plies saw relatively little improvement compared to the unidirectional ones.

This annealing cycle was then applied to cylindrical samples with three different layups. These layups included hoop-wound samples as a control and two different asymmetric layups comprised of 4 plies of 90° (hoop-wound) fibers and 4 plies of 45° fibers. The main difference was that vacuum bagging was not deemed necessary because the cylindrical geometry is self-constrained. These layups were selected because they are more representative of what may be used in aerospace or pressure vessel applications.

Strain gage measurements indicated that no significant amount of residual circumferential strain from the hoop-wound cylinders was relieved with annealing: there was no distinct clustering within the strain data. Meanwhile, the annealed samples sprung in by 1.2mm less than the in-situ consolidated ones. While a consistent trend was discernible in the radius data, the difference was too small to be statistically significant. This discrepancy could mean that strain gages may not be able to fully characterize the deformation occurring in these samples. Rigid body motion could contribute to the deformation, while causing no strain to be relieved. Given the behavior observed in the unidirectional flat samples, it was expected that annealing would have little impact along the fibers of hoop-wound samples. This could limit the applicability of the technology given that internal pressure acts along the circumferential direction.

Results were similar for the asymmetric samples. The $[90_4, 45_4]_T$ samples all spring out when cut. When measured using rosettes, the circumferential, axial, and shear strains did not vary significantly with annealing. The annealed samples sprung out by 0.3mm less on average than their in-situ consolidated counterparts. However, this difference was smaller than the standard deviation and therefore not statistically significant. The annealed $[45_4, 90_4]_T$ samples consistently sprung in by about 1mm more less than the in-situ consolidated ones, although this difference was again not found to be statistically significant. The rosettes showed no distinct trend in strain data. In both cases, the strain data measured using rosettes was unable to back up the trend seen in the radius measurements. More samples would be needed to reduce the standard deviation of the radius measurements.

The annealing had no significant impact on the fiber volume fraction nor the void content of these samples, measured at an average of 50.1% and 0.68% respectively. The relatively low fiber volume fraction seems to arise from the tape itself, rather than the manufacturing process. The void content is under 1%, which would be sufficiently low for primary aircraft structures

[114]. The crystallinity, particularly that of the asymmetric samples, was shown to improve with annealing. The in-situ and annealed samples had an average crystallinity of 20% and 27% respectively. While the annealing cycle could possibly be modified to achieve higher crystallinity values, this was still a significant improvement.

While there was a discernible improvement in the residual process stresses found in the flat samples, this was not the case for the thin rings. Several different things could explain these results. First, the dominant residual stresses in the rings could have been macro-mechanical or micromechanical stresses, which could not be corrected with annealing. Alternatively, the strain gages may not have been sensitive enough to discern a pattern. Finally, it is possible that the annealing parameters for rings may need adjustment. At this stage, it is not possible to tell which of these factors it could be. However, it was shown that annealing can increase the crystallinity of cylindrical samples without compromising the void content of fiber volume fraction. This presents an alternative application for the work presented here: annealing could be used to increase or normalize the crystallinity of thermoplastic parts manufactured using AFP. The original research goal of relieving residual process stress was met for flat samples, but not cylindrical ones.

8.1 Contributions

Several things are unique about the work presented here. First, there is no readily available standard that specifically prescribes tolerances for small thermoplastic reinforced composite sheets [80], [81], [82], [83]. Instead, inspiration had to be drawn from references for thermoset matrix composites and machined metal. This experiment provides a unique look into the deviation found in thermoplastic reinforced composites manufactured using AFP and to what degree that curvature can be reduced. It also highlights the fact that curvatures perpendicular to the fibers are what can be reduced, limiting the usefulness for layups most commonly found in pressure vessels. Finally, this work shows a discrepancy between the crystallinity recorded for hoop-wound and asymmetrical samples, which arises due to the manufacturing method.

The development of the annealing cycle (Chapter 3: Design of heat treatment cycle using flat panels) was presented at the American Society for Composites - Thirty-eight Technical Conference. This included a presentation with slides and a paper in the conference proceedings.

C. Scattolin and S. V. Hoa, “Shape Control for Thermoplastic Composites Made by Automated Fiber Placement Using Annealing,” in *Proceedings of the American Society for Composites - Thirty-eight Technical Conference*, Woburn, Massachusetts: DEStech Publications, Inc, Sep. 2022, p. 17.

8.2 Future work

Future work could take several forms. First, the annealing cycle for flat samples could be further optimized. It may be possible to achieve similar improvements to the flat samples with a shorter hold time and lower temperature. Slowing the cooling rate may further improve the sample crystallinity. For the rings, another system of measurement may be able to better measure the samples’ residual strains. The single point provided by strain gages may not have been sufficient. Image analysis, DIC, or videography may provide a more complete picture. However, these techniques have their own challenges, including how images or footage could be captured during the cutting process given that much of the view is obstructed by the saw.

Chapter 9: Manufacturing recommendations

Annealing thermoplastic composites has a variety of advantages and limitations. Advantages include more crystalline samples and reduced curvature in flat unidirectional parts. The main limitation of the annealing cycle tested here is that it seems unable to relieve residual stresses for thin hoop wound and asymmetric rings.

One distinct benefit of annealing is that it could be used to increase and normalize the crystallinity of samples without sacrificing the fiber volume fraction or void content. This is particularly relevant in samples constructed with angle plies. In this experiment, layups with 45° plies had the lowest in-situ crystallinity, likely due to the AFP head needing to lift and reposition between each tape. This would cause more rapid cooling than continuous winding, leading to lower crystallinity in samples containing off-axis plies. Annealing was able to increase the crystallinity of the samples with 45° plies so that they are on par with the hoop-wound samples.

Another advantage is that some of the warping found in thin unidirectional flat panels can be reversed. Samples with significant curvature were brought to within 2mm of flat. In a lab environment, this heat treatment could help flatten AFP samples before cutting them into coupons for subsequent destructive testing. This could include making dog-bone samples for tensile testing. In a more commercial environment, this could be used to correct the geometry of parts that have a generous tolerance. This kind of correction could also be done on the go or with limited space using a heat blanket.

One of the major limitations is that the annealing cycle presented here did not effectively relieve the residual stresses in samples with fully constrained geometries like rings. No significant amount of residual stress was relieved from the circumferential or radial directions of the rings. It also did not significantly impact the spring in or spring out behavior of the rings. This means that making curved structures using the procedure proposed in Figure 25 does not seem to be possible using the annealing cycle tested here. If the curved sample was laid up on a round mandrel and then cut away from the excess, the sample would likely spring, like it would when made on a conventional mandrel with free edges. It is possible that varying other manufacturing parameters like using a heated mandrel or changing the tape tension [27] could provide different results. The key to making this kind of manufacturing possible may be to modify the process parameters during manufacturing, rather than trying to remove during post processing.

References

- [1] A. Björnsson, “Automated layup and forming of prepreg laminates,” Doctoral Thesis, Linköping University, Linköping, Sweden, 2017. Accessed: Jan. 31, 2022. [Online]. Available: 10.3384/diss.diva-137488
- [2] W. D. Callister and D. G. Rethwisch, *Materials Science and Engineering: An Introduction*, 9th ed. Wiley, 2013.
- [3] J. R. Davis, “Guide to Materials Selection,” in *Engineered Materials Handbook Desk Edition*, M. M. Gauthier, Ed., ASM International, 1995, pp. 106–154. doi: 10.31399/asm.hb.emde.a0003005.
- [4] E. Oromiehie, B. G. Prusty, P. Compston, and G. Rajan, “Automated fibre placement based composite structures: Review on the defects, impacts and inspections techniques,” *Compos. Struct.*, vol. 224, p. 110987, Sep. 2019, doi: 10.1016/j.compstruct.2019.110987.
- [5] S. V. Hoa, *Principles of the Manufacturing of Composite Materials*, 2nd ed. Lancaster: DEStech, 2018.
- [6] K. Debnath, M. R. Choudhury, and A. E. W. Jarfors, “Primary Manufacturing of Thermoplastic Polymer Matrix Composites,” in *Primary and Secondary Manufacturing of Polymer Matrix Composites*, 1st ed., CRC Press, 2017, pp. 17–41. Accessed: May 03, 2022. [Online]. Available: <https://doi-org.lib-ezproxy.concordia.ca/10.1201/9781351228466>
- [7] S. Van Hoa, M. Duc Hoang, and J. Simpson, “Manufacturing procedure to make flat thermoplastic composite laminates by automated fibre placement and their mechanical properties,” *J. Thermoplast. Compos. Mater.*, vol. 30, no. 12, pp. 1693–1712, Dec. 2017, doi: 10.1177/0892705716662516.
- [8] C. Grant, “Automated processes for composite aircraft structure,” *Ind. Robot Int. J.*, vol. 33, no. 2, pp. 117–121, Jan. 2006, doi: 10.1108/01439910610651428.
- [9] Y. D. Boon, S. C. Joshi, and S. K. Bhudolia, “Review: Filament Winding and Automated Fiber Placement with In Situ Consolidation for Fiber Reinforced Thermoplastic Polymer Composites,” *Polymers*, vol. 13, no. 12, Art. no. 12, Jan. 2021, doi: 10.3390/polym13121951.
- [10] A. Brasington, C. Sacco, J. Halbritter, R. Wehbe, and R. Harik, “Automated fiber placement: A review of history, current technologies, and future paths forward,” *Compos. Part C Open Access*, vol. 6, p. 100182, Oct. 2021, doi: 10.1016/j.jcomc.2021.100182.
- [11] K. Yassin and M. Hojjati, “Processing of thermoplastic matrix composites through automated fiber placement and tape laying methods: A review,” *J. Thermoplast. Compos. Mater.*, vol. 31, no. 12, pp. 1676–1725, Dec. 2018, doi: 10.1177/0892705717738305.
- [12] S. T. Peters and J. L. McLarty, “Filament Winding,” in *Composites*, D. B. Miracle and S. L. Donaldson, Eds., ASM International, 2001, pp. 536–549. doi: 10.31399/asm.hb.v21.a0003416.
- [13] M. Schlottermuller, H. Lu, Y. Roth, N. Himmel, R. Schledjewski, and P. Mitschang, “Thermal Residual Stress Simulation in Thermoplastic Filament Winding Process,” *J. Thermoplast. Compos. Mater.*, vol. 16, no. 6, pp. 497–519, Nov. 2003, doi: 10.1177/089270503035407.
- [14] N. Bakhshi and M. Hojjati, “Effect of compaction roller on layup quality and defects formation in automated fiber placement,” *J. Reinf. Plast. Compos.*, vol. 39, no. 1–2, pp. 3–20, Jan. 2020, doi: 10.1177/0731684419868845.

- [15] Y. Qin, J. Summerscales, J. Graham-Jones, M. Meng, and R. Pemberton, “Monomer Selection for In Situ Polymerization Infusion Manufacture of Natural-Fiber Reinforced Thermoplastic-Matrix Marine Composites,” *Polymers*, vol. 12, no. 12, Art. no. 12, Dec. 2020, doi: 10.3390/polym12122928.
- [16] O. Olabisi and K. Adewale, Eds., *Handbook of Thermoplastics*, 2nd ed. Boca Raton: CRC Press, 2016. doi: 10.1201/b19190.
- [17] J. Barroeta Robles, M. Dubé, P. Hubert, and A. Yousefpour, “Repair of thermoplastic composites: an overview,” *Adv. Manuf. Polym. Compos. Sci.*, vol. 8, no. 2, pp. 68–96, Apr. 2022, doi: 10.1080/20550340.2022.2057137.
- [18] M. Flanagan *et al.*, “Out-of-autoclave manufacturing of a stiffened thermoplastic carbon fibre PEEK panel,” *AIP Conf. Proc.*, vol. 1896, no. 1, p. 030014, Oct. 2017, doi: 10.1063/1.5008001.
- [19] P. P. Parlevliet, H. E. N. Bersee, and A. Beukers, “Residual stresses in thermoplastic composites—A study of the literature—Part I: Formation of residual stresses,” *Compos. Part Appl. Sci. Manuf.*, vol. 37, no. 11, pp. 1847–1857, Nov. 2006, doi: 10.1016/j.compositesa.2005.12.025.
- [20] S. Béland, *High Performance Thermoplastic Resins and Their Composites*. New Jersey: Noyes Publications, 1990. [Online]. Available: <https://app.knovel.com/hotlink/toc/id:kpHPTRTC0F/high-performance-thermoplastic/high-performance-thermoplastic>
- [21] H. Ghayoor and S. Hoa, “Viscoelastic Analysis of Process-induced Stresses in Manufacturing of Thermoplastic Composites by Automated Fiber Placement Technology,” presented at the The 20th International Conference on Composite Materials, Copenhagen, Jul. 2015. Accessed: Sep. 10, 2021. [Online]. Available: https://www.researchgate.net/publication/311540800_Viscoelastic_Analysis_of_Process-induced_Stresses_in_Manufacturing_of_Thermoplastic_Composites_by_Automated_Fiber_Placement_Technology
- [22] M. Hyer W., *Stress Analysis of Fiber-Reinforced Composite Materials*. Pennsylvania, USA: DEStech Publications, Inc., 2009.
- [23] R. M. Jones, *Mechanics Of Composite Materials*, Second edition. Boca Raton, FL: CRC Press, 2014. [Online]. Available: <https://search.ebscohost.com/login.aspx?direct=true&scope=site&db=nlebk&db=nlabk&AN=1802660>
- [24] Y. Arao, J. Koyanagi, Y. Okudo, M. Otsuka, and H. Kawada, “Residual Stress Relaxation in CFRP Cross-ply Laminate,” *J. Solid Mech. Mater. Eng.*, vol. 4, no. 11, pp. 1595–1604, 2010, doi: 10.1299/jmmp.4.1595.
- [25] J. A. Barnes and G. E. Byerly, “The formation of residual stresses in laminated thermoplastic composites,” *Compos. Sci. Technol.*, vol. 51, no. 4, pp. 479–494, Jan. 1994, doi: 10.1016/0266-3538(94)90081-7.
- [26] A. Turnbull, A. S. Maxwell, and S. Pillai, “Residual stress in polymers—evaluation of measurement techniques,” *J. Mater. Sci.*, vol. 34, pp. 451–459, 1999, doi: <https://doi-org.lib-ezproxy.concordia.ca/10.1023/A:1004574024319>.
- [27] M. Schlottermuller, R. Schledjewski, and P. Mitschang, “Influence of process parameters on residual stress in thermoplastic filament-wound parts,” *Proc. Inst. Mech. Eng. Part J. Mater. Des. Appl.*, vol. 218, no. 2, pp. 157–164, Apr. 2004, doi: 10.1177/146442070421800209.

- [28] M. E. Fitzpatrick, A. T. Fry, P. Holdway, F. A. Kandil, J. Shackleton, and L. Suominen, "Determination of residual stresses by X-ray diffraction.," no. 2. National Physical Laboratory, Teddington, Sep. 2005. Accessed: Jul. 12, 2022. [Online]. Available: <https://eprintspublications.npl.co.uk/2391/>
- [29] F. Chinesta *et al.*, "First steps towards an advanced simulation of composites manufacturing by automated tape placement," *Int. J. Mater. Form.*, vol. 7, no. 1, pp. 81–92, Mar. 2014, doi: 10.1007/s12289-012-1112-9.
- [30] E. Oromiehie, B. G. Prusty, P. Compston, and G. Rajan, "Characterization of process-induced defects in automated fiber placement manufacturing of composites using fiber Bragg grating sensors," *Struct. Health Monit.*, vol. 17, no. 1, pp. 108–117, Jan. 2018, doi: 10.1177/1475921716685935.
- [31] L. Sorensen, T. Gmür, and J. Botsis, "Residual strain development in an AS4/PPS thermoplastic composite measured using fibre Bragg grating sensors," *Compos. Part Appl. Sci. Manuf.*, vol. 37, no. 2, pp. 270–281, Feb. 2006, doi: 10.1016/j.compositesa.2005.02.016.
- [32] N. Yadav, K. Wachtarczyk, P. Gąsior, R. Schledjewski, and J. Kaleta, "In-line residual strain monitoring for thermoplastic automated tape layup using fiber Bragg grating sensors," *Polym. Compos.*, pp. 1–13, doi: 10.1002/pc.26480.
- [33] F. Shadmehri and S. Hoa, "Digital Image Correlation Applications in Composite Automated Manufacturing, Inspection, and Testing," *Appl. Sci.*, vol. 9, p. 2719, Jul. 2019, doi: 10.3390/app9132719.
- [34] O. A. Tafreshi, S. V. Hoa, F. Shadmehri, D. M. Hoang, and D. Rosca, "Heat transfer analysis of automated fiber placement of thermoplastic composites using a hot gas torch," *Adv. Manuf. Polym. Compos. Sci.*, vol. 5, no. 4, Dec. 2019, doi: 10.1080/20550340.2019.1686820.
- [35] F. Sonmez, H. Hahn, and M. Akbulut, "Analysis of Process-Induced Residual Stresses in Tape Placement," *J. Thermoplast. Compos. Mater.*, vol. 15, pp. 525–544, Nov. 2002, doi: 10.1177/0892705702015006207.
- [36] Q. Miao, Z. Dai, G. Ma, F. Niu, and D. Wu, "Analysis of spring-back deformation of CF/PEEK thin angled laminates by laser-assisted forming," *Compos. Struct.*, vol. 321, p. 117288, Oct. 2023, doi: 10.1016/j.compstruct.2023.117288.
- [37] C. Dedieu, A. Barasinski, F. Chinesta, and J.-M. Dupillier, "About the origins of residual stresses in in situ consolidated thermoplastic composite rings," *Int. J. Mater. Form.*, vol. 10, no. 5, pp. 779–792, Oct. 2017, doi: 10.1007/s12289-016-1319-2.
- [38] M. Siegl and I. Ehrlich, "Transformation of the Mechanical Properties of Fiber-Reinforced Plastic Tubes from the Cartesian Coordinate System into the Cylindrical Coordinate System for the Application of Bending Models," *Athens J. Technology Eng.*, vol. 4, no. 1, pp. 47–62, Feb. 2017, doi: 10.30958/ajte.4-1-4.
- [39] C. Dedieu, A. Barasinski, F. Chinesta, and J.-M. Dupillier, "On the prediction of residual stresses in automated tape placement," *Int. J. Mater. Form.*, vol. 10, no. 4, pp. 633–640, Aug. 2017, doi: 10.1007/s12289-016-1307-6.
- [40] M. Cirino and R. B. Byron Pipes, "In-situ consolidation for the thermoplastic composite ring—residual stress state," *Compos. Manuf.*, vol. 2, no. 2, pp. 105–113, Jan. 1991, doi: 10.1016/0956-7143(91)90187-L.

- [41] M. W. Hyer and C. Q. Rousseau, “Thermally Induced Stresses and Deformations in Angle-Ply Composite Tubes,” *J. Compos. Mater.*, vol. 21, no. 5, pp. 454–480, May 1987, doi: 10.1177/002199838702100504.
- [42] J. T. Tzeng, “Predictions and Experimental Verification of Residual Stresses in Thermoplastic Composite Cylinders,” *J. Thermoplast. Compos. Mater.*, vol. 8, no. 2, pp. 163–179, Apr. 1995, doi: 10.1177/089270579500800202.
- [43] O. Sayman, “Analysis of multi-layered composite cylinders under hygrothermal loading,” *Compos. Part Appl. Sci. Manuf.*, vol. 36, no. 7, pp. 923–933, Jul. 2005, doi: 10.1016/j.compositesa.2004.12.007.
- [44] C. S. Chouchaoui and O. O. Ochoa, “Similitude study for a laminated cylindrical tube under tensile, torsion, bending, internal and external pressure. Part I: governing equations,” *Compos. Struct.*, vol. 44, no. 4, pp. 221–229, Apr. 1999, doi: 10.1016/S0263-8223(98)00068-3.
- [45] M. Xia, H. Takayanagi, and K. Kemmochi, “Analysis of multi-layered filament-wound composite pipes under internal pressure,” *Compos. Struct.*, vol. 53, no. 4, pp. 483–491, Sep. 2001, doi: 10.1016/S0263-8223(01)00061-7.
- [46] D. Fricke, L. Raps, and I. Schiel, “Prediction of warping in thermoplastic AFP-manufactured laminates through simulation and experimentation,” *Adv. Manuf. Polym. Compos. Sci.*, vol. 8, no. 1, pp. 1–10, Jan. 2022, doi: 10.1080/20550340.2021.2015212.
- [47] M. A. Khan, P. Mitschang, and R. Schledjewski, “Parametric study on processing parameters and resulting part quality through thermoplastic tape placement process,” *J. Compos. Mater.*, vol. 47, no. 4, pp. 485–499, Feb. 2013, doi: 10.1177/0021998312441810.
- [48] H. Xin, D. E. T. Shepherd, and K. D. Dearn, “Strength of poly-ether-ether-ketone: Effects of sterilisation and thermal ageing,” *Polym. Test.*, vol. 32, no. 6, pp. 1001–1005, Sep. 2013, doi: 10.1016/j.polymertesting.2013.05.012.
- [49] W. J. Unger and J. S. Hansen, “The Effect of Cooling Rate and Annealing on Residual Stress Development in Graphite Fibre Reinforced PEEK Laminates,” *J. Compos. Mater.*, vol. 27, no. 2, pp. 108–137, Feb. 1993, doi: 10.1177/002199839302700201.
- [50] X. Wang *et al.*, “Effects of thermal residual stress on interfacial properties of polyphenylene sulphide/carbon fibre (PPS/CF) composite by microbond test,” *J. Mater. Sci.*, vol. 51, no. 1, pp. 334–343, Jan. 2016, doi: 10.1007/s10853-015-9251-2.
- [51] M. Greisel, J. Jäger, J. Moosburger-Will, M. G. R. Sause, W. M. Mueller, and S. Horn, “Influence of residual thermal stress in carbon fiber-reinforced thermoplastic composites on interfacial fracture toughness evaluated by cyclic single-fiber push-out tests,” *Compos. Part A*, vol. 66, pp. 117–127, 2014, doi: 10.1016/j.compositesa.2014.07.010.
- [52] P. Cebe, “Annealing study of poly(etheretherketone),” *J. Mater. Sci.*, vol. 23, no. 10, pp. 3721–3731, Oct. 1988, doi: 10.1007/BF00540520.
- [53] J.-A. E. Manson and J. C. Seferis, “Autoclave Processing of PEEK/Carbon Fiber Composites,” *J. Thermoplast. Compos. Mater.*, vol. 2, no. 1, pp. 34–49, Jan. 1989, doi: 10.1177/089270578900200103.
- [54] J. A. Mondo and K. A. Parfrey, “Performance of In-Situ Consolidated Thermoplastic Composite Structure,” *Sampe Soc. Adv. Mater.*, vol. 27, pp. 361–370, 1995.
- [55] G. Lebrun and J. Denault, “Effect of annealing on the thermal expansion and residual stresses of bidirectional thermoplastic composite laminates,” *Compos. Part Appl. Sci. Manuf.*, vol. 41, no. 1, pp. 101–107, Jan. 2010, doi: 10.1016/j.compositesa.2009.09.009.

- [56] V.-T. Hoang *et al.*, “Postprocessing method-induced mechanical properties of carbon fiber-reinforced thermoplastic composites,” *J. Thermoplast. Compos. Mater.*, p. 0892705720945376, Aug. 2020, doi: 10.1177/0892705720945376.
- [57] S. Risteska, A. Trajkovska Petkoska, S. Samak, and M. Drienovsky, “Annealing Effects on the Crystallinity of Carbon Fiber-Reinforced Polyetheretherketone and Polyohenylene Laminate Composites Manufactured by Laser Automatic Tape Placement,” *Mater. Sci.*, vol. 26, pp. 308–316, Feb. 2020, doi: 10.5755/j01.ms.26.3.21489.
- [58] S.-L. Gao and J.-K. Kim, “Cooling rate influences in carbon fibre/PEEK composites. Part 1. Crystallinity and interface adhesion,” *Compos. Part Appl. Sci. Manuf.*, vol. 31, no. 6, pp. 517–530, Jun. 2000, doi: doi.org/10.1016/S1359-835X(00)00009-9.
- [59] H. El Kadi and J. Denault, “Effects of Processing Conditions on the Mechanical Behavior of Carbon-Fiber-Reinforced PEEK,” *J. Thermoplast. Compos. Mater.*, vol. 14, no. 1, pp. 34–53, Jan. 2001, doi: 10.1106/XDX9-U8K4-E0PM-70MX.
- [60] T. W. Giants, “Crystallinity and dielectric properties of PEEK, poly(ether ether ketone),” *IEEE Trans. Dielectr. Electr. Insul.*, vol. 1, no. 6, pp. 991–999, Dec. 1994, doi: 10.1109/94.368664.
- [61] W. J. Cantwell, P. Davies, and H. H. Kausch, “The effect of cooling rate on deformation and fracture in IM6/PEEK composites,” *Compos. Struct.*, vol. 14, no. 2, pp. 151–171, Jan. 1990, doi: 10.1016/0263-8223(90)90028-D.
- [62] T. Tsukada, S. Minakuchi, and N. Takeda, “Assessing residual stress redistribution during annealing in thick thermoplastic composites using optical fiber sensors,” *J. Thermoplast. Compos. Mater.*, vol. 33, no. 1, pp. 53–68, Jan. 2020, doi: 10.1177/0892705718804580.
- [63] S. Valvez, A. P. Silva, P. N. B. Reis, and F. Berto, “Annealing effect on mechanical properties of 3D printed composites,” *Procedia Struct. Integr.*, vol. 37, pp. 738–745, Jan. 2022, doi: 10.1016/j.prostr.2022.02.004.
- [64] D. Cohen and M. W. Hyer, “Residual stresses in cross-ply composite tubes,” Virginia Polytechnic Institute and State University, NASA-CR-173540, Apr. 1984. Accessed: Aug. 11, 2022. [Online]. Available: <https://ntrs.nasa.gov/citations/19840017700>
- [65] S. P. Timoshenko and J. N. Goodier, *Theory of Elasticity*, 3rd ed. McGraw-Hill, 1970.
- [66] T. Chapman, J. Gillespie Jr, B. Pipes, J.-A. Manson, and J. Seferis, “Prediction of Process-Induced Residual Stresses in Thermoplastic Composites,” *J Comp Mat*, vol. 24, Jun. 1990, doi: 10.1177/002199839002400603.
- [67] L. S. Srinath and Y. V. G. Acharya, “Stresses in a circular ring: Comparison of theory with experiment,” *Appl. Sci. Res.*, vol. 4, no. 3, pp. 189–194, May 1954, doi: 10.1007/BF03184950.
- [68] “Treating of steel | Britannica.” Accessed: Jun. 30, 2022. [Online]. Available: <https://www.britannica.com/technology/steel/Treating-of-steel>
- [69] S. S. Sahay, “Annealing of Steel,” in *Steel Heat Treating Fundamentals and Processes, ASM Handbook*, vol. 4A, 2013, pp. 289–304. Accessed: Jun. 30, 2022. [Online]. Available: DOI: 10.31399/asm.hb.v04a.a0005787
- [70] J. Hirsch, “Annealing of Aluminum and Its Alloys,” vol. 4E, 2016. Accessed: Jun. 30, 2022. [Online]. Available: DOI: 10.31399/asm.hb.v04e.a0006285
- [71] G. E. Totten, Ed., “Annealing and Recrystallization of Coppers,” in *Heat Treating of Nonferrous Alloys*, vol. 4E, ASM International, 2016, p. 0. doi: 10.31399/asm.hb.v04e.a0006278.

- [72] J. L. Johnson, “Annealing of Refractory Metals,” 2016. Accessed: Jun. 30, 2022. [Online]. Available: DOI: 10.31399/asm.hb.v04e.a0006255
- [73] K. R. Hart, R. M. Dunn, J. M. Sietins, C. M. Hofmeister Mock, M. E. Mackay, and E. D. Wetzel, “Increased fracture toughness of additively manufactured amorphous thermoplastics via thermal annealing,” *Polymer*, vol. 144, pp. 192–204, May 2018, doi: 10.1016/j.polymer.2018.04.024.
- [74] W. J. Unger and J. S. Hansen, “The Effect of Thermal Processing on Residual Strain Development in Unidirectional Graphite Fibre Reinforced PEEK,” *J. Compos. Mater.*, vol. 27, no. 1, pp. 59–82, Jan. 1993, doi: 10.1177/002199839302700105.
- [75] W.-M. Sim, “Residual Stress Engineering in Manufacture of Aerospace Structural Parts,” presented at the 3rd International conference on distortions engineering, Bremen, Sep. 2011, pp. 187–194. Accessed: Jul. 31, 2023. [Online]. Available: https://trimis.ec.europa.eu/sites/default/files/project/documents/20121115_114058_91510_Paper_IDE_2011.pdf
- [76] A. Madariaga, I. Perez, P. J. Arrazola, R. Sanchez, J. J. Ruiz, and F. J. Rubio, “Reduction of distortions in large aluminium parts by controlling machining-induced residual stresses,” *Int. J. Adv. Manuf. Technol.*, vol. 97, no. 1, pp. 967–978, Jul. 2018, doi: 10.1007/s00170-018-1965-2.
- [77] “Technical Data Sheet APC-2 PEEK Thermoplastic Polymer Prepreg,” Solvay, Alpharetta, GA, USA, TDS APC-2_2017_10_11, Oct. 2017.
- [78] N. Gallo, S. Pappadá, U. Raganato, and S. Corvaglia, “Development of the ‘High Pressure Repair Dome’ system for in-situ high performance repair of aeronautic structures,” *MATEC Web Conf.*, vol. 188, p. 04004, 2018, doi: 10.1051/mateconf/201818804004.
- [79] V. Srinivasan, “Computational Metrology for the Design and Manufacture of Product Geometry: A Classification and Synthesis,” *J. Comput. Inf. Sci. Eng.*, vol. 7, no. 1, pp. 3–9, May 2006, doi: 10.1115/1.2424246.
- [80] G. Henzold, Ed., “16 - General Geometrical Tolerances,” in *Geometrical Dimensioning and Tolerancing for Design, Manufacturing and Inspection (Second Edition)*, Oxford: Butterworth-Heinemann, 2006, pp. 137–151. doi: 10.1016/B978-075066738-8/50021-7.
- [81] D20 Committee, “Specification for Dimensional Tolerance of Thermosetting Glass-Reinforced Plastic Pultruded Shapes,” ASTM International. doi: 10.1520/D3917-15A.
- [82] “ASTM D5687/D5687M-20 Standard Guide for Preparation of Flat Composite Panels with Processing Guidelines for Specimen Preparation,” in *Annual Book of ASTM Standards 2020*, vol. 15.03, West Conshohocken: ASTM International, 2015.
- [83] G. Bogucki, W. McCarvill, S. Ward, and J. Tomblin, “Guidelines for the Development of Process Specifications, Instructions, and Controls for the Fabrication of Fiber-Reinforced Polymer Composites,” National Institute for Aviation Research, DOT/FAA/AR-02/110, Mar. 2003. Accessed: Jun. 02, 2022. [Online]. Available: <https://apps.dtic.mil/sti/pdfs/ADA413644.pdf>
- [84] C. Collins, N. L. Batista, and P. Hubert, “Warpage investigation of carbon/PEEK discontinuous long fibre thin panels,” *J. Compos. Mater.*, vol. 55, no. 24, pp. 3529–3537, Oct. 2021, doi: 10.1177/00219983211002247.
- [85] G. Ameta, R. Lipman, S. Moylan, and P. Witherell, “Investigating the Role of Geometric Dimensioning and Tolerancing in Additive Manufacturing,” *J. Mech. Des.*, vol. 137, no. 11, Oct. 2015, doi: 10.1115/1.4031296.

- [86] D. C. Montgomery and G. C. Runger, *Applied statistics and probability for engineers*, Sixth edition. Hoboken, NJ: John Wiley and Sons, Inc, 2014.
- [87] “Evaluating Goodness of Fit - MATLAB & Simulink.” Accessed: May 13, 2022. [Online]. Available: <https://www.mathworks.com/help/curvefit/evaluating-goodness-of-fit.html>
- [88] A. Navlani, A. Fandango, and I. Idris, “R-Squared,” in *Python Data Analysis (3rd Edition)*, 3rd ed., Packt Publishing, 2021, pp. 266–288. Accessed: May 13, 2022. [Online]. Available: <https://app-knovel-com.lib-ezproxy.concordia.ca/hotlink/pdf/id:kt012W3AU5/python-data-analysis/rmse>
- [89] F. L. Litvin and A. Fuentes, “Gaussian Curvature; Three Types of Surface Points,” in *Gear Geometry and Applied Theory*, 2nd ed., Cambridge University Press, 2004, pp. 153–201. Accessed: May 12, 2022. [Online]. Available: <https://app-knovel-com.lib-ezproxy.concordia.ca/hotlink/pdf/id:kt009XUTK2/gear-geometry-applied/gaussian-curvature-three>
- [90] A. Pressley, *Elementary Differential Geometry*. in Springer Undergraduate Mathematics Series. London: Springer London, 2010. doi: 10.1007/978-1-84882-891-9.
- [91] V. A. Toponogov, *Differential geometry of curves and surfaces: a concise guide*. Boston: Birkhäuser, 2006.
- [92] S. Timoshenko, “Analysis of Bi-Metal Thermostats,” *J. Opt. Soc. Am.*, vol. 11, no. 3, p. 233, Sep. 1925, doi: 10.1364/JOSA.11.000233.
- [93] N. Carbajal, G. Vargas, A. Arrese, and F. Mujika, “Analysis of Thermal Stresses in Unsymmetric Cross-ply Composite Strips,” *J. Compos. Mater.*, vol. 42, no. 12, pp. 1247–1266, Jun. 2008, doi: 10.1177/0021998308091735.
- [94] K. D. Cowley and P. W. R. Beaumont, “The measurement and prediction of residual stresses in carbon-fibre/polymer composites,” *Compos. Sci. Technol.*, vol. 57, no. 11, pp. 1445–1455, Jan. 1997, doi: 10.1016/S0266-3538(97)00048-1.
- [95] “Technical Data Sheet APC-2-PEEK Thermoplastic Polymer,” Cytec Engineered Materials.
- [96] I. Daniel and O. Ishai, “Appendix A: Material Properties,” in *Engineering Mechanics of Composite Materials*, 2nd ed., New York: Oxford University, 2006, pp. 373–383.
- [97] “ZX130L | Industrial Robots by Kawasaki Robotics,” Kawasaki Robotics. Accessed: Apr. 04, 2023. [Online]. Available: <https://kawasakirobotics.com/eu-africa/products-robots/zx130l/>
- [98] “Strain Gage Installation Checklist Composite and Plastic Materials,” Micro-Measurements, Raleigh, NC, USA, MS0270-1803-EN. Accessed: Oct. 25, 2022. [Online]. Available: https://docs.micro-measurements.com/?id=11353&_ga=2.67794584.869125972.1666710512-1436451991.1665777323
- [99] “Instruction Bulletin B-129-8: Surface Preparation for Strain Gage Bonding,” Micro-Measurements, Raleigh, NC, USA, 11129, Dec. 2011. Accessed: Oct. 27, 2022. [Online]. Available: http://www.vishaypg.com/docs/11129/11129_b1.pdf
- [100] “Instruction Bulletin B-127: Strain Gage Installations with M-Bond 200 Adhesive,” Micro-Measurements, Raleigh, NC, USA, BUL 11127, Feb. 2018. Accessed: Jul. 20, 2023. [Online]. Available: <https://micro-measurements.com/knowledge-base/instruction-bulletins>
- [101] “S5198 General Purpose Strain Gages—Linear Pattern,” Micro-Measurements, Raleigh, NC, USA, 11138, Apr. 2018. Accessed: Jul. 11, 2023. [Online]. Available: <https://micro-measurements.com/pca/detail/s5198>

- [102] “235SL General Purpose Strain Gages—Linear Pattern,” Micro Measurements, Raleigh, NC, USA, 11409, May 2019. Accessed: Feb. 17, 2023. [Online]. Available: <https://docs.micro-measurements.com/?id=12140>
- [103] “LePage Technical Data Sheet Polyurethane Wood Glue.” LePage, Jan. 05, 2016. Accessed: Feb. 17, 2023. [Online]. Available: <https://www.lepage.ca/en/lepage-products/build-things/wood-glue/polyurethane-wood-glue.html>
- [104] *Model 8000-8-SM Instruction Manual*, 1.12. Raleigh, NC, USA: Micro-Measurements, 2014.
- [105] “StrainSmart 8000 Getting Started Guide,” Micro-Measurements, Raleigh, NC, USA, MM130-000287, Feb. 2020.
- [106] “Strain Gage Sensor Reference Guide,” Micro Measurements, Raleigh, NC, USA, 8690-EN_May20, May 2020. Accessed: Feb. 01, 2023. [Online]. Available: <https://docs.micro-measurements.com/?id=8690>
- [107] “Arc measurement tool,” Digimizer. Accessed: Nov. 25, 2022. [Online]. Available: <https://www.digimizer.com/manual/u-arc.php>
- [108] L. Conklin, “Tutorial for Collecting and Processing Images of Composite Structures to Determine the Fiber Volume Fraction,” Hampton, Virginia, NASA/CR-2017-219365, Jan. 2017. Accessed: Nov. 02, 2022. [Online]. Available: <https://ntrs.nasa.gov/citations/20170001570>
- [109] C. N. Morales, G. Claire, J. Álvarez, and A. Nanni, “Evaluation of fiber content in GFRP bars using digital image processing,” *Compos. Part B Eng.*, vol. 200, p. 108307, Nov. 2020, doi: 10.1016/j.compositesb.2020.108307.
- [110] M. Doumeng *et al.*, “A comparative study of the crystallinity of polyetheretherketone by using density, DSC, XRD, and Raman spectroscopy techniques,” *Polym. Test.*, vol. 93, p. 106878, Jan. 2021, doi: 10.1016/j.polymertesting.2020.106878.
- [111] F. Shadmehri, S. V. Hoa, J. Fortin-Simpson, and H. Ghayoor, “Effect of in situ treatment on the quality of flat thermoplastic composite plates made by automated fiber placement (AFP),” *Adv. Manuf. Polym. Compos. Sci.*, vol. 4, no. 2, pp. 41–47, Apr. 2018, doi: 10.1080/20550340.2018.1444535.
- [112] “Universal Analysis Getting Started Guide,” TA Instruments, New Castle, May 2004. Accessed: Mar. 21, 2023. [Online]. Available: https://www.t-k-e.com/handbooks/Getting_Started_Universal_Analysis_2000.pdf
- [113] D. J. Blundell and B. N. Osborn, “The morphology of poly(aryl-ether-ether-ketone),” *Polymer*, vol. 24, no. 8, pp. 953–958, Aug. 1983, doi: 10.1016/0032-3861(83)90144-1.
- [114] M. H. Hassan, A. R. Othman, and S. Kamaruddin, “A review on the manufacturing defects of complex-shaped laminate in aircraft composite structures,” *Int. J. Adv. Manuf. Technol.*, vol. 91, no. 9, pp. 4081–4094, Aug. 2017, doi: 10.1007/s00170-017-0096-5.
- [115] G. K. Jeyakodi, “Finite Element Simulation of the In - Situ AFP process for Thermoplastic Composites using Abaqus,” Master Thesis, Delft University of Technology, Delft, Netherlands, 2016. Accessed: Nov. 22, 2023. [Online]. Available: <https://repository.tudelft.nl/islandora/object/uuid%3A6c13aaca-5f12-47b2-92ed-7744c64bcbb7>
- [116] “Plane-Shear Measurement with Strain Gages,” Intertechnology, Toronto, Ontario, Tech Note TN-512-1. Accessed: Dec. 15, 2023. [Online]. Available: https://intertechnology.com/Vishay/TechNotes_TechTips.html

- [117] D. G. Zill, *Advanced Engineering Mathematics*, 7th ed. Burlington, MA: Jones & Bartlett Learning, LLC, 2022. Accessed: Jan. 12, 2022. [Online]. Available: <https://ebookcentral-proquest-com.lib-ezproxy.concordia.ca/lib/concordia-ebooks/detail.action?docID=6450212>
- [118] “Solve Differential Equation - MATLAB & Simulink.” Accessed: Oct. 25, 2023. [Online]. Available: https://www.mathworks.com/help/symbolic/solve-a-single-differential-equation.html?s_cid=ans2doc_man_link
- [119] J. T. Tzeng and R. B. Pipes, “Thermal residual stress analysis for in situ and post-consolidated composite rings,” *Compos. Manuf.*, vol. 3, no. 4, pp. 273–279, 1992, doi: 10.1016/0956-7143(92)90114-A.
- [120] A. C. Ugural and S. K. Fenster, “Chapter 2. Strain and Material Properties,” in *Advanced Mechanics of Materials and Applied Elasticity*, 6th ed., Pearson, 2020.